

ELECTROCHEMICAL SYNTHESIS OF NANOSTRUCTURED MATERIALS AND RELATED ANODIC BEHAVIORS

Mingliang Wang

School of Mechanical and Chemical Engineering

The University of Western Australia



This thesis is presented for the Degree of Doctor of Philosophy of

The University of Western Australia

2011

Abstract

This work studies the formation mechanisms of anodized materials and their related electrochemical anodic behaviors. Electrochemical anodization is a versatile method to create various materials with intricate nanostructured morphologies. These materials have potentials for various functional applications in chemical and biomedical sensing, photocatalysis, energy conversion in batteries and supercapacitors.

The study is focused on three main aspects: experimental synthesis of anodized materials, theoretical analysis of formation mechanisms of anodized materials and fabrication metallic nanowires using anodized porous alumina. The following summarizes the highlights of the study.

Firstly, different anodized structures are synthesized experimentally, including nano-channeled anodized alumina, nanoporous anodized tin oxide and anodized SnC₂O₄ particles. The related electrochemical behaviors of the metals during anodization are quantified and explained.

Anodization current oscillations: The phenomenon of spontaneous periodical current oscillation during electrochemical anodization of tin in alkaline electrolytes is observed. Such phenomenon has been reported in the literature. Attempts have been made to explain this phenomenon on the basis of oxide film lift-off and electrolyte diffusion. This study demonstrates that the current oscillation is caused by oxygen generation and release on the tin anode, causing periodic redistribution of ion concentration in the electrolyte. The analysis also enables determination of the contributions of the two anodic reactions of tin oxidation and oxygen generation to

the total anodic current.

Secondly, a unified theory for the formation of surface structures of metals induced by anodization is proposed. The theory is based on thermodynamic and electrochemical principles. It is able to explain the main experimental observations of all three types of anodic structures, including solid compact oxide films, porous oxides and porous metal surface layers.

Unified theory for the formation of anodized structures: The unified theory explains that the formation of porous or compact metal oxide and porous metal structures is dictated by the reaction free energy balance between the electrochemical anodic formation of the metal oxide and the chemical dissolution of the metal oxide in the same electrolyte. Based on this theory, a range of key experimental observations reported in the literature are explained, including (1) the selection of the formation of compact oxide, porous oxide or porous metal during anodization, (2) voltage dependence of thickness of compact oxides, and (3) in-situ pore perforation by step-wise reduction of anodization voltage.

Thirdly, the study proposes an analysis as generic criteria for preferential orientation growth of metallic nanowires during electrochemical deposition using nanoporous anodized alumina templates.

Preferential growth orientation of metallic nanowires by cathodic deposition: The observation of metallic nanowires orientation dependence on cathodic deposition potentials is explained in terms of nucleation thermodynamics and crystal growth kinetics. The analysis demonstrates that at low deposition potentials, the wire axial orientation is determined by the criterion of minimum total surface energy, with the close-packed planes forming the exterior of the crystals. At high deposition potentials, the crystal axial orientation is predominantly determined by growth kinetics, i.e.,

close packed directions and the highest planar coordination numbers.

The thesis is written as a series of research publications, including four papers published in *Electrochimica Acta*, and one submitted to *Crystal Growth & Design*.

The list is summarized as following:

1. Preparation of nanoporous tin oxide by electrochemical anodization in alkaline electrolytes, *Electrochimica Acta*, 56 (2011) 8797-8801.
2. Current oscillations during potentiostatic anodization of tin in alkaline electrolytes, *Electrochimica Acta* 56 (2011) 7051-7057.
3. Anodization process of Sn in oxalic acid at low applied voltages, *Electrochimica Acta*, 59 (2012) 441-448.
4. A unified thermodynamic model for the formation of anodized aluminium oxide structures, *Electrochimica Acta*, 62 (2012) 424-432.
5. Growth orientation control of Co nanowires fabricated by electro-deposition method using porous alumina templates, *submitted to Crystal Growth & Design*, October 2011.

Statement of Candidate Contribution (%)

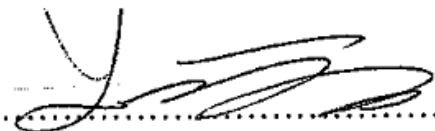
The relative contribution of the candidate and other co-authors to each work are presented below. Each author has given permission for the work to be included in this thesis.

1. **Mingliang Wang (70%)**, Yinong Liu, Dongfeng Xue, Dongke Zhang, Hong Yang, *Preparation of nanoporous tin oxide by electrochemical anodization in alkaline electrolytes*, *Electrochimica Acta*, 56 (2011) 8797-8801.
2. **Mingliang Wang (80%)**, Hong Yang, Yinong Liu, *Current oscillations during potentiostatic anodization of tin in alkaline electrolytes*, *Electrochimica Acta* 56 (2011) 7051-7057.
3. **Mingliang Wang (80%)**, Yinong Liu, Dongke Zhang, Hong Yang, *Anodization process of Sn in oxalic acid at low applied voltages*, *Electrochimica Acta*, 59 (2012) 441-448.
4. **Mingliang Wang (60%)**, Yinong Liu and Hong Yang, *A unified thermodynamic model for the formation of anodized metal oxide structures*, *Electrochimica Acta*, 62 (2012) 424-432.
5. **Mingliang Wang (80%)**, Yinong Liu and Hong Yang, *Growth orientation control of Co nanowires fabricated by electro-deposition method using porous alumina templates*, submitted to *Crystal Growth & Design*, October 2011.

Student Signature:

Mingliang Wang

Coordinating Supervisor Signature:



Acknowledgements

I would like to thank greatly my supervisors, Winthrop Professor Yinong Liu and Associate Professor Hong Yang, who has dedicatedly, diligently and patiently guided and helped me completing my thesis.

I would like also to thank the University of Western Australia and Chinese Scholarship Council to provide the scholarship to co-support me to study at Australia.

I would particularly the School of Mechanical and Chemical Engineering and Centre for Microscopy, Characterisation and Analysis (CMCA), for all the technical and administrative I have received. To the academic, technical and administrative staff, who are always friendly, generous and helpful.

Sincere appreciations are extended to my study mates and colleagues in Lab for Functional Materials and Centre for Energy, for your generous help in both scholar and daily life.

To all the friends I have made throughout my PhD candidature, especially those whom I have shared an office and play sports with. Thank you for your friendship.

Lastly, unparalleled thanks to my family, for generously giving their love, help and encouragement, especially my parents for their whole-hearted support since I was born; my beloved wife, Ou Zhu, for the past and future time with love, trust and mutual encouragement.

Mingliang Wang (October 2011)

Table of Contents

Abstract	i
Statement of Candidate Contribution	iv
Acknowledgements	v
Table of Contents	vi
Chapter 1: Introduction	1
Chapter 2: Preparation of nanoporous tin oxide by electrochemical anodization in alkaline electrolytes	37
Chapter 3: Current oscillations during potentiostatic anodization of tin in alkaline electrolytes	51
Chapter 4: Anodization process of Sn in oxalic acid at low applied voltages	69
Chapter 5: A unified thermodynamic model for the formation of anodized metal oxide structures	90
Chapter 6: Growth orientation control of Co nanowires fabricated by electro-deposition method using porous alumina templates	119
Chapter 7: Closing Remarks	141

CHAPTER 1. Introduction

Time has witnessed the dramatic progress in nanoscience and nanotechnology since the famous lecture by Richard Feynman [1] over 50 years ago announcing “There’s plenty of room at the bottom”. In his lecture, Feynman talked about “the problem of manipulating and controlling things on a small scale” and discussed “the ability to observe and control individual atoms and molecules”. Feynman’s lecture has seen the seed for what is now recognized as the nanotechnology [2, 3]. The idea of manipulating atoms has been realized thereafter by consistent effort from scientific and technological communities around the world. In the past few decades, it has been proven the investigation in the nanoscale of matters has the ability to make exciting technological advancements for the benefit of mankind [2].

1.1. Nanoscience and Nanotechnology

1.1.1. Nano Scale

The word “nano” is originated from a Greek word meaning “dwarf”. In the international system of units, the prefix “nano” means one-billionth, or 10^{-9} . Therefore, one nanometer is one-billionth of a meter [4]. Figure 1 shows the scale of things for both natural and manmade [5]. Since this small size of “nanometer” is far from the recognition in daily life, there are some examples for comparison [6]:

- A strand of human DNA is ~2.5 nanometers in diameter.
- A bacterium is ~2,500 nanometers (2.5 micrometers) long.
- A large raindrop is ~2,500,000 nanometers (2.5 millimeters) in diameter.
- A single gold atom is about a third of 1 nanometer in diameter.
- A single wall carbon nanotube is 1 nanometer in diameter.
- A human hair is approximately 100,000 nanometers (100 micrometers) wide.
- A house is about 10,000,000,000 nanometers (10 meters) wide.

The word “nanoscale” is mostly related to a scale of approximately 1 nm to 100 nm [7].

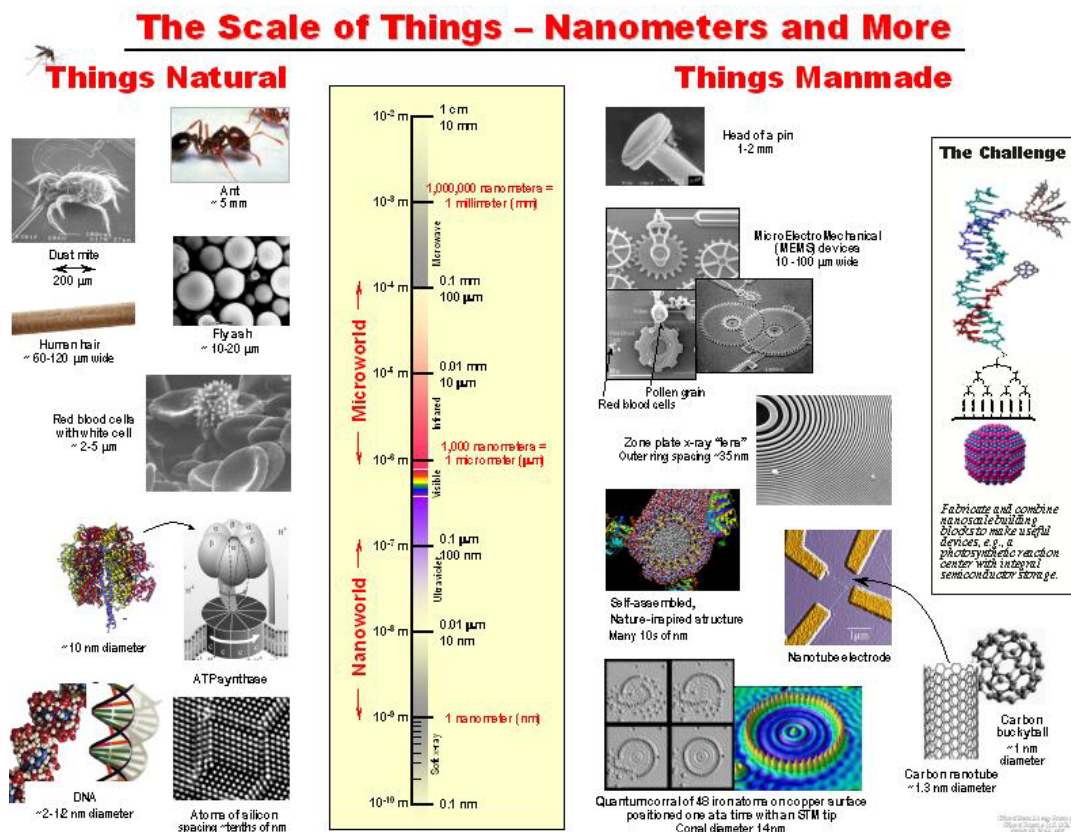


Figure 1. The scale of things: Natural and Manmade [5].

1.1.2. Nanomaterials

The nanomaterials are defined as materials with any external dimension in the nanoscale or having internal or surface structure in the nanoscale [7]. The most distinguished difference between nanomaterials and bulk materials is on the size, as

self-evidenced from the name “nanomaterials”. Nanomaterials can be created in a great variety of morphologies. Figure 2 shows a selected of examples, including: (a) CdSe quantum dots [8], (b) Fe nanocubes [9], (c) Au nanocages [10], (d) ZnO nanobelts [11], (e) Si nanowires array [12] and (f) anodized nanoporous aluminium oxide film. The abundant morphological styles of nanomaterials entitle them as an intensive attracted research field in both science and technology in recent decades.

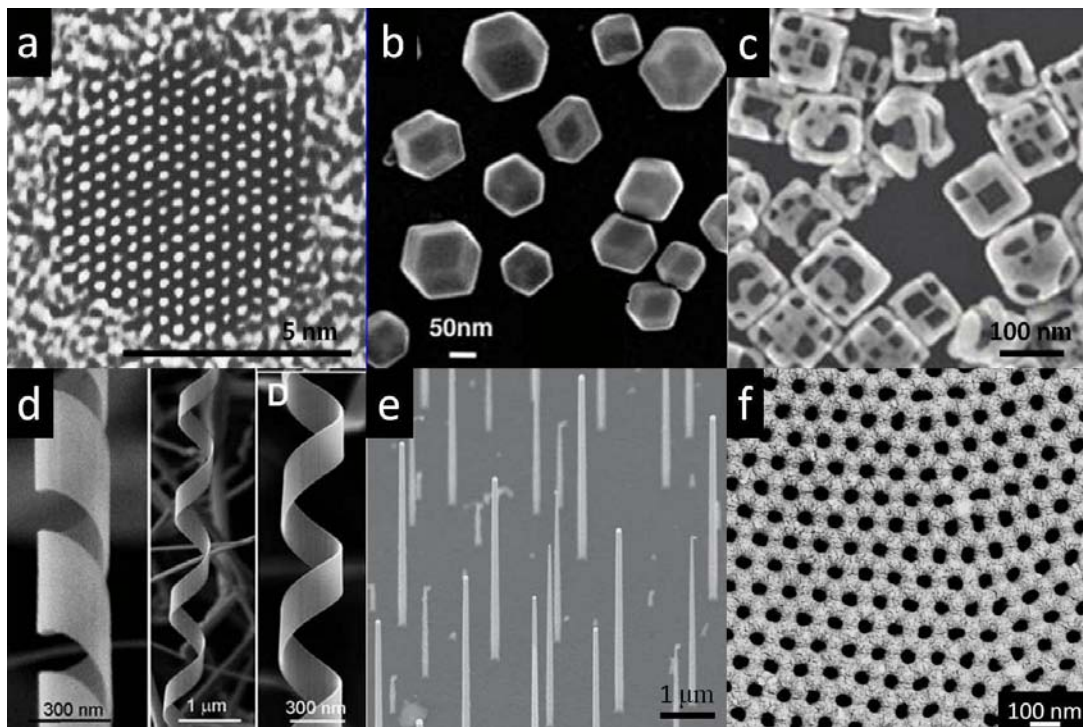


Figure 2. Examples of nanomaterials morphologies: (a) CdSe quantum dots [8], (b) Fe nanocubes [9], (c) Au nanocages [10], (d) ZnO nanobelts [11], (e) Si nanowires array [12], and (f) anodized nanoporous aluminium oxide film.

1.1.3. Nanoporous Materials and Applications

Nanoporous metal oxides are among the most intensively studied nanomaterials due to their high technological potentials in novel applications including as templates for fabricating nanostructures [13, 14], photocatalysts [15, 16], self-cleaning substrates [17, 18] and solar cell electrodes [19-21]. The nanoporous structures have a large specific surface area, thus benefit in synthesizing alien nanostructures, or performing as functional substrates.

The anodized aluminium oxide (AAO) template is one of the earliest [22] and most widely investigated nanoporous materials. Due to its chemical inertness, ordered pore arrangement and controllable pore size, the AAO membranes have been used widely as the templates to create other nanostructures. For example, by depositing a thin layer of Ag (≈ 20 nm) onto AAO membranes, Qiu et al. [23] discovered that this Ag-coated AAO composite can be used as surface enhanced Raman scattering (SERS) substrate for sensitive detection of chemical and biological species. Figure 3 shows a series of Ag-coated AAO nanostructures with different pore sizes (a-e), and a typical XRD spectrum of Ag-coated AAO templates (f). The pore size of Ag-coated AAO nanostructures can be tuned, which in turn controls the signal intensity of characteristic peaks of Raman spectrum for Rhodamine (Rhodamine 6G molecular, 1510 cm^{-1})(Figure 3(g)). This composite SERS substrate has potential application in identification of the trace amount of organics in the medical and environmental detection.

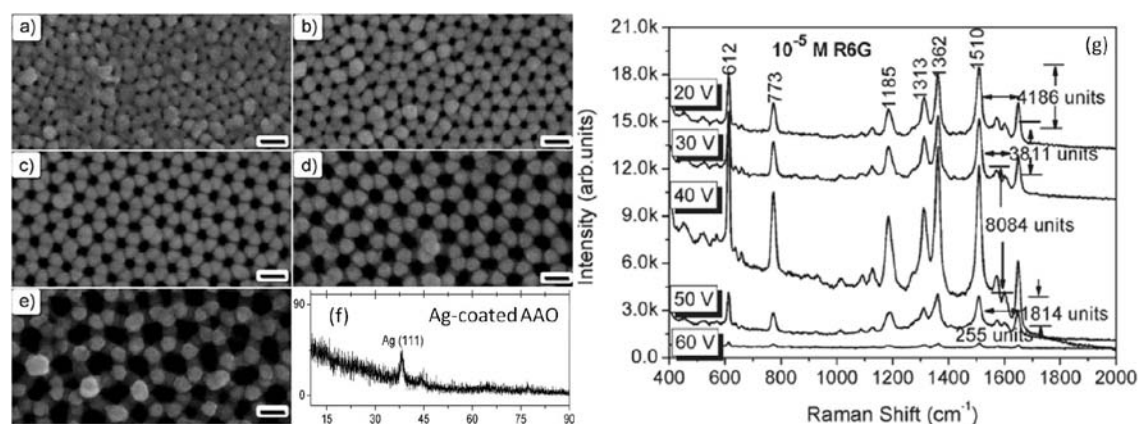


Figure 3. A series of SEM images acquired from the Ag-coated AAO membranes formed under different constant DC voltages: a) 20, b) 30, c) 40, d) 50, and e) 60 V. The scale bar is 100 nm. The sputtering times for Ag are all set to be 10 min; (f) XRD spectrum of a typical Ag/AAO membrane; (g) SERS spectral comparison of 10^{-5} M R6G adsorbed on the Ag-coated AAO membranes shown in (a-e), and a quantitative enhancement comparison is shown in the insets [23].

The anodized titanium oxide (ATO) nanotubes are widely investigated as a functional material itself because TiO_2 is an n-type semiconductor and a good UV absorbent. For

instance, the ATO nanotubes are a promising candidate as a transparent electrode in the dye-sensitized solar cell (DSSC). Figure 4(b) shows the schematic drawing of a DSSC integrated with ATO nanotube arrays (Figure 4(a)) as electrodes [24]. The overall light-to-electricity efficiency of 6.86% can be achieved using 17.6 μm long ATO nanotube electrodes [25] (Figure 4(c)). Owing to the large surface area and improved electron transport efficiency in the oriented nanostructures [26] (Figure 4(d)), it is expected the conversion efficiency in the ATO integrated DSSC could be further improved for the commercialized application [27].

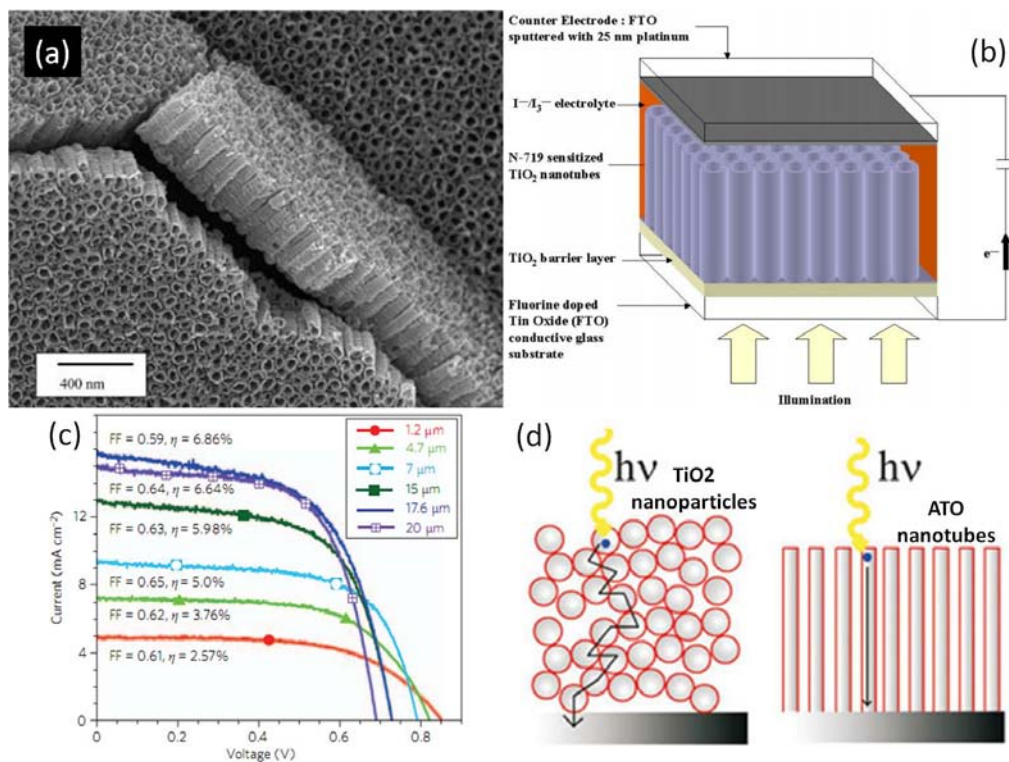


Figure 4. (a) a typical SEM micrograph of the ATO nanotube array [28]; (b) schematic drawing of a DSSC integrated by ATO nanotube arrays as electrodes [24]; (c) Current-voltage characteristics of DSSC fabricated using the ATO nanotube array of various lengths [25]; (d) electron path through a nanoparticles layer and an oriented nanostructure [26].

Tin dioxide (SnO_2) is another n-type semiconductor widely utilized in solid-state gas sensors [29, 30] and as oxidation catalysts [31] for a long history. The ever-growing need for high capacity and high power rechargeable batteries especially for emerging

large-scale applications (e.g., electric cars), has stimulated continuous research efforts aimed at developing advanced electrode materials for next generation high power and high energy density lithium-ion batteries. Tin-based materials can in principle deliver much higher specific lithium storage capacities ($790 \text{ mA}\cdot\text{h}\cdot\text{g}^{-1}$ for SnO_2 and $990 \text{ mA}\cdot\text{h}\cdot\text{g}^{-1}$ for Sn, corresponding to $\text{Li}_{4.4}\text{Sn}$) [32] than the currently used graphite-based anode materials (theoretical lithium storage capacity of graphite is $372 \text{ mA}\cdot\text{h}\cdot\text{g}^{-1}$, corresponding to LiC_6)

However, Sn-based anode suffers from a large volume change of $> 200\%$ accompanying Li insertion and extraction [33], a problem common to anode materials based on the Li-metal alloying/dealloying mechanism. This volume change destructs the mechanical stability of the electrode, and leads to rapid degeneration of conductive pathways within the electrode.

To alleviate this so called pulverization problem and to improve the structural stability of Sn-based electrode during Li insertion-extraction cycling, several materials design strategies have been proposed and investigated, including porous Sn oxide nanostructures [34, 35] and Sn oxide/C composite materials [32, 36, 37]. Among them, porous nanostructures of Sn-based electrode seem to be promising where nanopores are believed to provide physical space to partially accommodate the large volume change of Sn-anode during charge/discharge cycles [34, 35]. Electrochemical anodization is an effective method to create nanoporous tin oxide structures as demonstrated by this study and others [38-40].

1.2. Metal Anodization

Anodization of metals is a well-established technique for the synthesis of metal oxide structures on metal [41]. Metal anodization is an electrochemical process carried out by applying voltages/currents in a cell where metal is functioned as anode. It has been shown that electrochemical anodization is able to create varieties of porous metal

oxide structures of various metals e.g., Al [13, 42], Ti [43-46], Nb [47], Ta [48, 49], W [50], Zr [51], Fe [52, 53], Sn [40] and Ni [54]. These porous structures include ordered [55] (Figure 5(a)) or randomly [53] organized nano-channels (Figure 5(b)), nanotubes [46] (Figure 5(c)), and nano-porous sponge structures [14, 47] (Figure 5(d)).

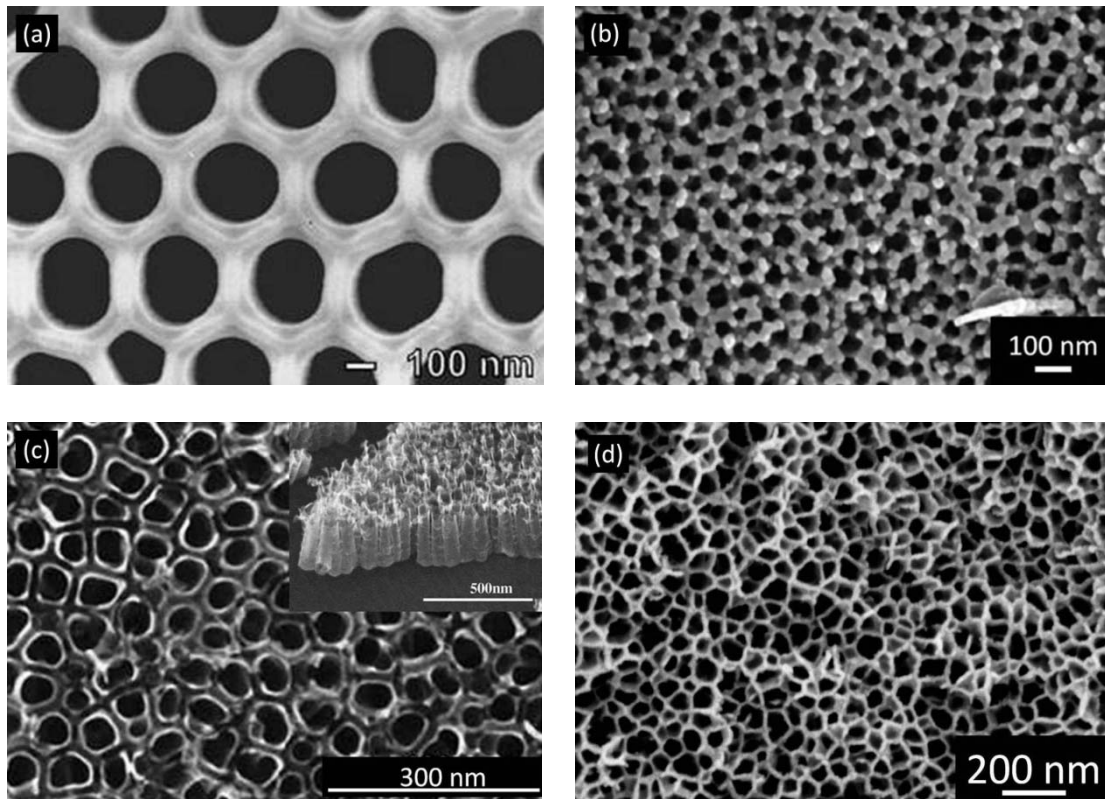


Figure 5. SEM micrographs showing typical morphologies of anodized metal oxides: (a) top view of porous Al_2O_3 of ordered nano-channels (10 wt% H_3PO_4 electrolyte at 160 V) [55]; (b) top view of porous Fe_2O_3 of random nano-channels (1% HF + 0.5% NH_4F + 0.2% HNO_3 electrolyte at 40 V) [53], (c) top view and side view (inset) of nano-tubular porous TiO_2 (formed in 0.5 wt% HF + 1 M H_3PO_4 electrolyte at 10 V) [56] and (d) porous sponge SnO_2 (formed in 0.5 M NaOH electrolyte at 12 V [57]).

1.3. Aluminium Anodization

Since 1900s, aluminium anodization has received significant attention due to their applications in protective and decorative coatings [22], and particularly in nanomaterials fabrications [41]. Electrochemical anodization enables in-situ

formation of a thick alumina layer on aluminium with desired morphologies.

Aluminium anodization is one of the most extensively investigated cases in electrochemical materials science. The current anodization theories are mostly originated from the study of aluminium anodization. This session will provide a review on the experimental discoveries and theoretical understandings in aluminium anodization. It includes the general classification of the anodized alumina, the electrochemical and chemical reactions responsible for the formation of anodized alumina, and the current understanding on formation mechanisms including pore initiation and growth of porous anodized alumina.

1.3.1. Compact and Porous Anodized Alumina

Anodized alumina is often classified based on its most obvious morphological feature; being compacted or porous. Figure 6 shows the typical cross section micrographs (a) compact [58] and (b) porous type [59] anodized alumina and their corresponding schematic drawings in (c) and (d). The morphological development of anodized alumina is largely dependent on the current density/applied voltages, and the type of electrolytes [42, 60, 61].

Generally, the compact type anodized alumina are found to form in weak acidic and near neutral solutions (e.g. boric acid, ammonium borate and ammonium tartrate), where anodized alumina cannot be dissolved chemically once formed [42]. The porous type anodized alumina, on the other hand, is created in relatively stronger acidic electrolytes (e.g. H_2SO_4 , $\text{H}_2\text{C}_2\text{O}_4$ and H_3PO_4), in which anodized alumina could be formed anodically and dissolved chemically in a dynamic balance [41, 42, 62].

The thickness of the compact anodized alumina depends only on the applied anodization voltage and reaches a final value of ~ 1.4 nm/V irrespective of anodization duration [37]. For the case of porous anodized alumina, there is a constant barrier

layer at the pore bottom (Figure 6(d)). The thickness of the barrier layer is also found to be mainly dependent on applied voltages with $t_{\text{barrier}} \approx 1.04 \text{ nm/V}$ in 0.4 M H_3PO_4 electrolytes [59]. The thickness of porous anodized alumina can reach to $\sim 100 \mu\text{m}$ [63].

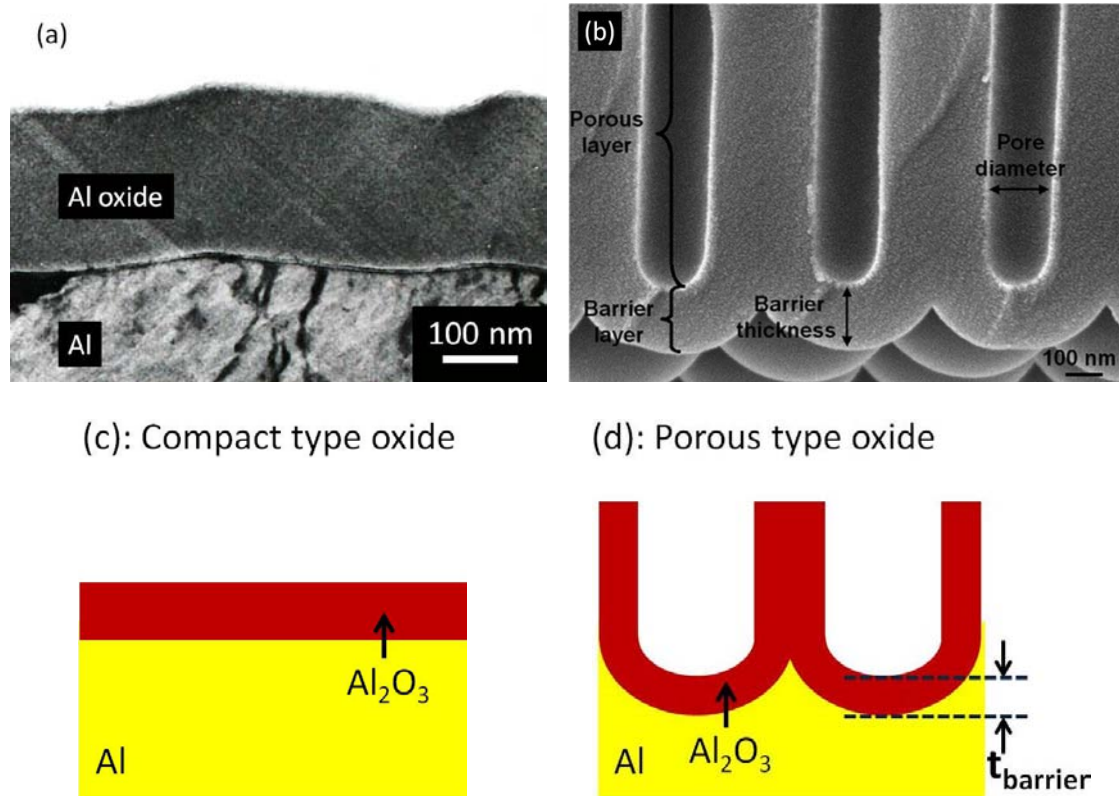


Figure 6. Typical cross section micrographs and schematic drawing of compact and porous type anodized alumina.

1.3.2. Reactions in Anodization

Figure 7 shows a schematic setup for aluminium anodization experiments. In an electrochemical cell, aluminium is used as anode and an electrochemical inert material (e.g., Pt, C and Ti) is as cathode. When the voltage/current source is switched on, the anodized alumina begins to form. The electrochemical reactions during the anodization process can be written as following [64]:

Anode:



Cathode:



where the reaction (1) is responsible for the growth of anodized alumina, whereas the hydrogen evolution via reaction (2) occurs at the cathode.

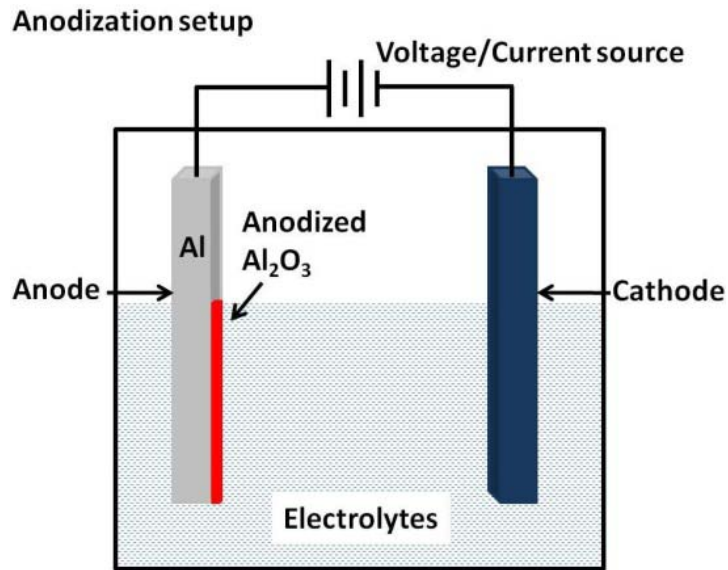


Figure 7. A schematic setup for Al anodization experiment.

Other chemical reactions are found to accompany the electrochemical reactions (1) and (2) mentioned above [59, 65] during the anodization process. Figure 8 presents a schematic description of anodic electrochemical and chemical reactions supporting the growth of anodized alumina. Initially, an anodized Al₂O₃ layer is formed immediately when the voltage/current source is switched on. The oxide/electrolyte (o/e) interface and metal/oxide (m/o) interface are created. The aluminium anodization proceeds via various ion conductions (e.g. O²⁻ and Al³⁺) under electric field [61, 66].

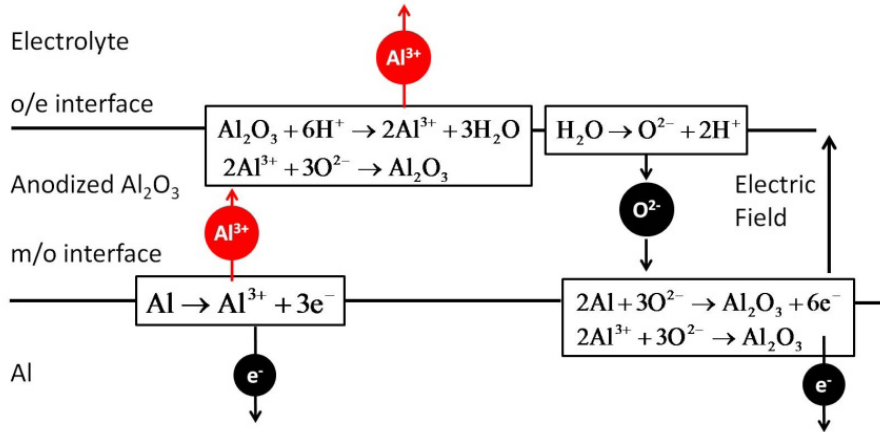


Figure 8. Schematic description of anodic electrochemical and chemical reactions in anodized oxides growth [59, 65, 67].

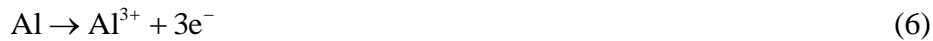
For oxygen-containing ionic species such as O^{2-} (or OH^-), it is considered an O^{2-} ion is generated by the water splitting at o/e interface [59] via reaction (3):



O^{2-} ions migrate across the anodized alumina to the m/o interface driven by the electric field. Finally, O^{2-} ions react with Al (or Al^{3+}) to form Al_2O_3 via reaction (4) (or reaction (5)) at the m/o interface:



For an Al^{3+} ion, it is formed at the m/o interface through anodic dissolution reaction (6):



Some of Al^{3+} ions are combining with O^{2-} ions in-situ to form Al_2O_3 via reaction (5). While the rest of Al^{3+} ions migrate across the oxide layer to the o/e interface to form Al_2O_3 , again via reaction (5).

In the case where porous anodized alumina forms, chemical dissolution of alumina via reaction (7) occurs concurrently at the o/e interface:



1.3.3. Mechanisms of Formation of Porous Anodized Alumina

Through extensive studies on the anodized alumina, it has established that the microstructural evolution of anodized alumina can be monitored through the current density-time (i.e. i - t) profile in potentiostatic anodization. Figure 9(a) shows a schematic diagram of typical i - t curves for compact and porous anodized alumina respectively [61, 68, 69]. Figure 9(b) display the morphology evolution based on current variations in i - t curves accordingly [62].

In the case of compact anodized alumina formation, the typical i - t curve is divided into two stages (Figure 9(a)). Stage I shows a significant initial reduction in current corresponding to the initial formation and growth of alumina. The new oxide forms at the m/o interface through ionic diffusion of O^{2-} . Stage II shows the current stabilize at a very low plateau value, corresponding to the leaking current [70].

In the case of porous anodized alumina formation, the typical i - t curve is characterized in three stages (Figure 9(a)). Stage I is an immediate current drop after switching on the anodic bias due to form of an oxide layer at m/o interface. However, it is considered there are accompanying pits (Pore precursors) randomly initiate at o/e interface in the oxide caused by chemical dissolution. Stage II is a slightly increase from the minimum current, which means formation of pores in compact oxide. Stage III shows a leveled current plateau which can last for a long time, where the porous structure grows steadily [62, 69].

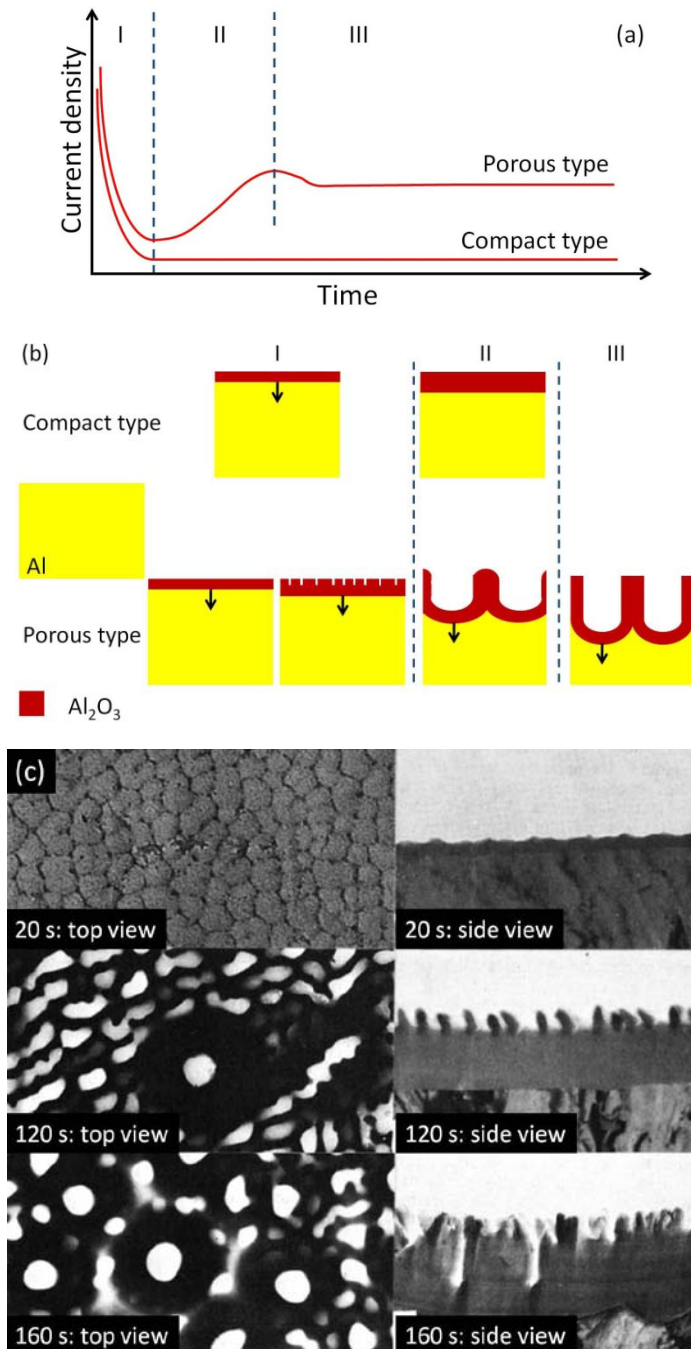


Figure 9. (a) A schematic diagram of typical *i-t* curves for compact and porous anodized alumina respectively; (b) Schematic drawings of morphology evolution based on current variations in *i-t* curves accordingly; (c) A set of TEM micrographs [62] of pore formation process according to the three stages in the porous type *i-t* curve of (a).

Figure 9(c) shows a set of TEM micrographs [62] demonstrating the pore formation process corresponding to the three stages in the porous type *i-t* curve of Figure 9(a). In

this classic reference [62], it was clearly shown a layer of compact oxide was initially formed at anodization of 20 s (Stage I). At 120 s anodization (Stage II), the pore precursors were formed at o/e interface. The pores were finally formed with the scalloped pore bottom shape at m/o interface at anodization of 160 s (Stage III). Based on the experimental studies, it is generally accepted the creation of porous anodized alumina are made up of two consecutive processes: pore initiation and pore growth. The following paragraphs will give a review of current knowledge in these two processes.

1.3.3.1. Pore Initiation Mechanisms

Understanding the formation mechanism of porous anodized alumina has been scientific focal point since the first structure was produced experimentally. For a compact anodized alumina to develop into a porous structure, it is generally was accepted that pores are initiated by roughing o/e interface during anodization [70]. Although the fundamental mechanism of pores initiation is still eluded, there are several proposed models in this field.

Keller et al. [22] proposed a local dissolution model. At the beginning of the anodizing process, formation of the homogeneous compact anodized alumina occurred. The local dissolution took place at surface defects/imperfects, where the concentrated current passes through, thus caused temperature of the electrolyte to increase locally. The localized oxide dissolution was consequently enhanced and pores initiate at those local sites on the oxide layer. However, this speculative model has no experimental support.

Physically, Raja et al. [71] proposed a stain-induced instability at o/e interface to explain pore initiation in anodization. However, they did not have any supportive evidence.

Recently, Oh et al. [72] reported that they confirmed the chemical dissolution of oxide effect caused the formation of pits. Nevertheless, it was shown that the porous oxide structure has a significantly different length scale, which should not result from the chemical dissolution. They proposed a mechanical instability with forced plastic deformation and flow of the oxide should account for the pore initiation. This new explanation is under discussion. However, the physical ground of plastic flow in anodized metal oxide is not clear yet.

The pore initiation is a core issue in the porous anodized alumina study. However, current understandings are on the explanation of experiments, and then generalize the phenomenological models. The fundamental physics for pore initiation is still beyond our knowledge, which needs more investigations.

1.3.3.2. Pore Growth Mechanism

- **Field-Assisted Dissolution Model**

The field-assisted dissolution model was firstly proposed by Hoar et al. [73], in which it was assumed that the Al_2O_3 dissolution rate was greatly promoted in presence of electric field. Due to the geometry effect, the strength of electric field is greatly increased at the pore bottom, thus enhances the dissolution rate of oxide. It is in this manner, the dynamic balance of oxidation and dissolution for pore growth is established.

O'Sullivan et al. [59] further developed a detailed chemical dissolution model. Figure 10 shows the schematic diagram illustrating the physical origin of the field-assisted dissolution model [59]. It was suggested the rate-determining step for oxide dissolution is the breaking of Al-O bonds from Al_2O_3 lattice at the o/e interface. They argued that at the o/e interface, Al-O bond should be stretched from its equilibrium position under influence of the electric field, thus lower the activation energy of

dissolution. The anodized alumina dissolution rate should be promoted, when an O^{2-} ion was chelated by two H^+ ions and an Al^{3+} ion was solvated by six H_2O molecules.

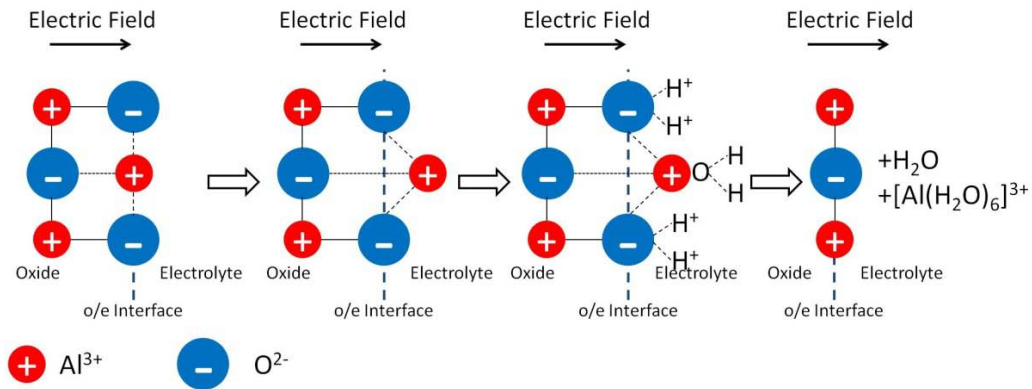


Figure 10. Schematic diagram showing physical origin of the field assisted dissolution model [59].

Although this model is the most cited in anodization studies till now, the field-assisted oxide dissolution effect is still in debate. The steady pore growth is characterized by a stable electrochemistry and chemistry process during aluminium anodization, as is shown a leveled current density in the typical i - t curve (Figure 9(a)). These features suggested there was a dynamic balance of electrochemical oxide formation at m/o interface and chemical dissolution of oxide. However, Hunter et al. [74] reported if this dynamic balance were maintained at pore growth front during anodization (in 53wt% H_2SO_4 at 0.2 mA/cm^2), it would require local electrolyte to reach $\sim 124^\circ\text{C}$ at pore bottom to maintain the rate of chemical dissolution. Nevertheless, local Joule heating was estimated to increase by $<10^\circ\text{C}$ in the electrolyte near pore bottom. Furthermore, the nature of the oxide dissolution is a chemical reaction [70]. The exact impact of the electric field on chemical reactions has not been demonstrated experimentally yet.

- Field-Assisted Plastic Flow Model

Recently, Thompson et al. [75] have proposed the field-assisted plastic flow model

base on the observation of ions transport during anodization using a layer of W tracer in aluminium anodization in H_3PO_4 electrolytes. Figure 11(a) shows the W trace layer distribution during anodization [75].

Initially, a ~ 20 nm thick W layer was deposited in ~ 600 nm thick Al film. The W layer was located near the middle of Al film. During the anodization, it was originally anticipated O^{2-} ions would migrate to m/o interface to form Al_2O_3 and WO_3 , and then W^{6+} ions would migrate outwardly to o/e interface via the field-assisted dissolution mechanism. Thus W species incorporated at the pore region should lie ahead of W at the pore walls along the metal-electrolyte direction.

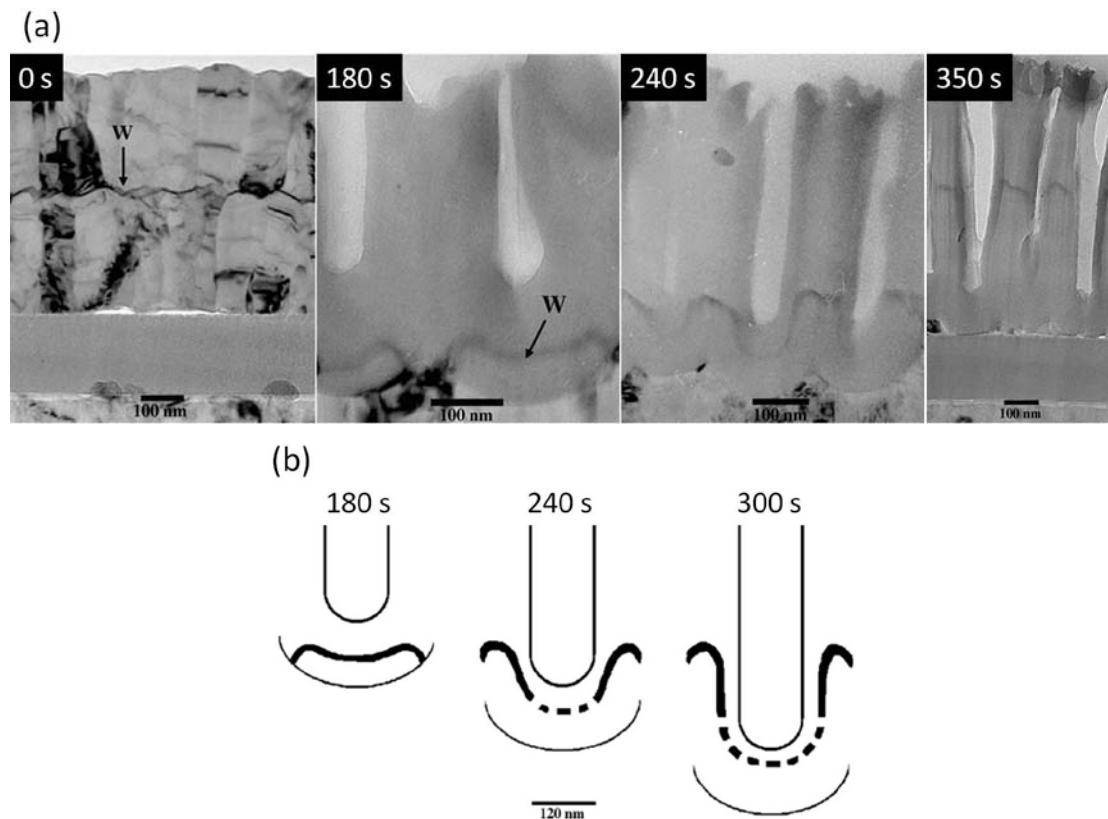


Figure 11. (a) A W trace layer distribution during anodization at 5 mA/cm^2 in $0.4 \text{ M H}_3\text{PO}_4$ solution at 293K . (b) Schematic drawing of the evolution on W trace distribution [75].

On the contrary, it was observed W species at pore walls moved ahead of that beneath the pore region, where the W layer showed a downward distortion experimentally

(Figure 11(a)). The author also confirmed a portion of W species have been found to migrate outward, whether incorporated into the oxide or into the electrolyte. Further, the outward movement of the tungsten species eventually located in pore wall regions was consistent with the observations at pore bottom. Furthermore, the reversal of W species from a cation to an anion species would lead to a separation of the distributions of cationic and anionic tungsten species, which is not observed by TEM.

Figure 11 (b) shows a schematic drawing of the evolution on W trace distribution [75]. In order to explain this phenomenon, it was proposed a field-assisted plastic flow model for steady pore growth, and argued the materials flow was facilitated by the plasticity of anodized oxides via the ionic transport.

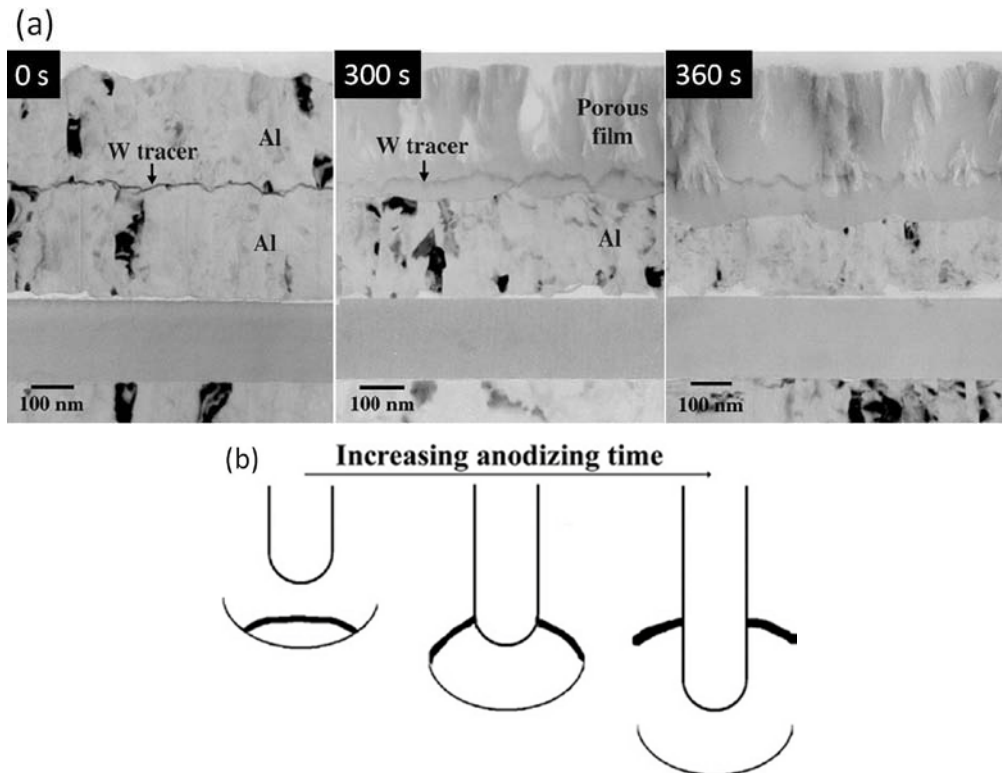


Figure 12. (a) A W trace layer distribution during anodization at 60 in 0.13 M borax electrolyte at 333K. (b) Schematic drawing of the evolution on W trace distribution [76].

However, it has been proven that this mechanism can not be uniformly applied to other anodization cases. Thompson et al. [76] performed a similar anodization

experiment in alkaline electrolytes. Figure 12(a) shows the W trace layer distribution during anodization [76]. It was observed W species incorporated at the pore region laid ahead of W at the pore walls along the metal-electrolyte direction as expected. Figure 12(b) shows a schematic drawing of the evolution on W trace distribution [76]. It was suggested the field-assisted dissolution mechanism was viable in this study.

It is worth mentioning that studies up-to-date generalize that the two models can account for parts of the experimental phenomena respectively. For example, the pore growth proceeded by the field-assisted dissolution mechanism in chromic acid [77] and alkaline electrolyte [76], and by the field-assisted plastic flow mechanism in sulfuric [78], oxalic [79], malonic [79] and phosphoric acid [75, 80]. It is not clear basic physics of these two models, and under what conditions one of the models is accountable.

- **Theoretical Analysis**

Although most pore growth mechanisms are proposed based on experimental studies, some theoretical analysis on pore growth phenomenon has also been published. The physical basis of these theoretical analyses is the field assisted dissolution mechanism.

Parkhutik et al. [69] firstly established a theoretical model for porous structure formation during aluminium anodization. By considering the pore development as a result of competition between oxide growth and oxide dissolution processes and calculating the electric field distribution in the oxide, analytic expressions for the pore size and interpore distance as a function of anodization parameters such as applied voltages are established. These expressions predicted the linear dependence of pore diameter and interpore on applied voltages, which are confirmed by the experimental results.

Thamida et al. [65] revised the Parkhutik's model by incorporating effects from the

pH of electrolytes. The expression of interpore distance was proposed dependent on both of applied voltages and pH of electrolytes. Based on this model, the interpore distance has a hyperbolic relation with pH of electrolytes under a constant applied voltage. However, the experimental studies showed a near constant relation between interpore distance and the pH of electrolytes [81].

So far, the more successful analysis is Parkhutik`s model, they have provided the maths expressions for both pore size and interpore distance as a function of applied voltages and verified it experimentally. Thamida`s is based on the Parkhutik`s model. Nevertheless, this derived model is disqualified by experimental observations. It is worth to mention the physical background of field-assisted dissolution mechanism is not clear. Thus, all these models based on such mechanism are soulless. Even, Parkhutik`s model are successfully in verification of experimental observations. The following model is invalid, which is inferred that without a suitable physical justification, the theoretical analysis is unavailing.

It is required a deeper understanding on the pore growth case physically. In this study, it is proposed a unified theory describing the rules governing the formation of various oxide and metal nanostructures via electrochemical anodization. This unified theory, based on thermodynamic and electrochemical principles, explains that the formation of porous or compact metal oxide and porous metal structures is dictated by the reaction free energy balance between the electrochemical anodic formation of the metal oxide and the chemical dissolution of the metal oxide in the electrolyte.

1.3.4. Ordered Porous Anodized Aluminium Oxide

In 1995, Masuda et al. [13] invented a two-step anodization method to fabricate ordered porous anodized aluminium oxide (AAO) templates with high density of parallel nanopores. The ability to create ordered anodized oxide structure has opened up a new research domain where a wide range of nanowires [73] and nanotubes [74]

of metal and alloys using this ordered structure as a template.

This session will provide a review on the critical conditions required to form ordered structure and comment on the pore ordering mechanism. There seem to be two key requirements in order to produce an ordered porous AAO structure. The ordered structure can only be produced by a two-step anodization method and within a specific electrochemical anodization window.

- Two-step anodization process

In order to form ordered pore structures in AAO, a two-step anodization process is required [13]. Figure 13 shows the schematic diagram of the two-step anodization method invented by Masuda et al.[13]. Firstly, a piece of untreated aluminium with a relatively rough surface is thoroughly washed with acetone, ethanol and distill water respectively. Secondly, the cleaned aluminium piece is electro-polished to obtain an smooth surface; the polishing is done in a mixed ethanol and perchloric acid (HClO_4) solution in volume ration of 4:1 at 0 °C at 20 V for 2~3 minutes. Thirdly, the first aluminium anodization is performed at a constant voltage in an electrolyte for hours, e.g. at 40 V in 0.3 M oxalic acid for 6 hours. This produces anodized alumina with irregular pores. Fourthly, the chemical etching of alumina produced in first anodization is performed in chromic acid (1.8 wt%) and phosphoric acid (6 wt%) at 80 °C for 1 hour. This step dissolves the anodized alumina produced in step 3, and leaves the hexagonal arranged dimple structure on aluminium surface. Lastly, the second aluminium anodization is performed in the same conditions as the first anodization. Completing the last step, an AAO template with perfect hexagonal arranged pores is thus created.

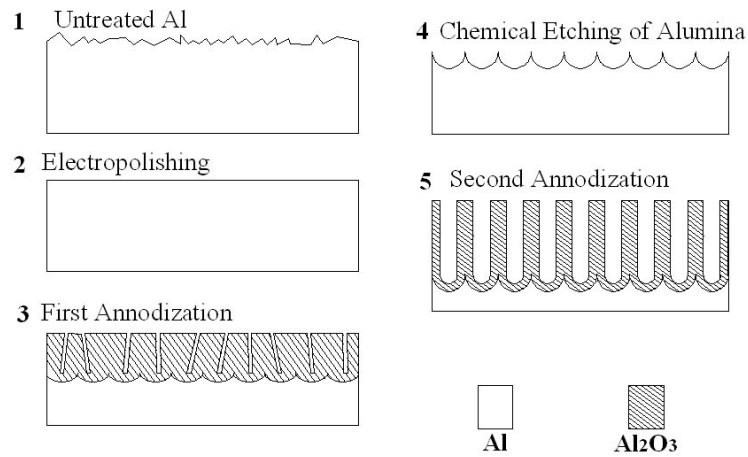


Figure 13. Schematic map of two-step anodization method [13].

Figure 14(a) and (b) show the typical top view and side view SEM micrographs respectively for ordered AAO templates fabricated using two-step anodization method. Figure 14(c) shows a schematic drawing of the AAO pore structure, where characteristic parameter including pore diameter (D_p), interpore distance (D_{int}), barrier layer thickness (t_{barrier}) and the template thickness (t_{AAO}) are defined.

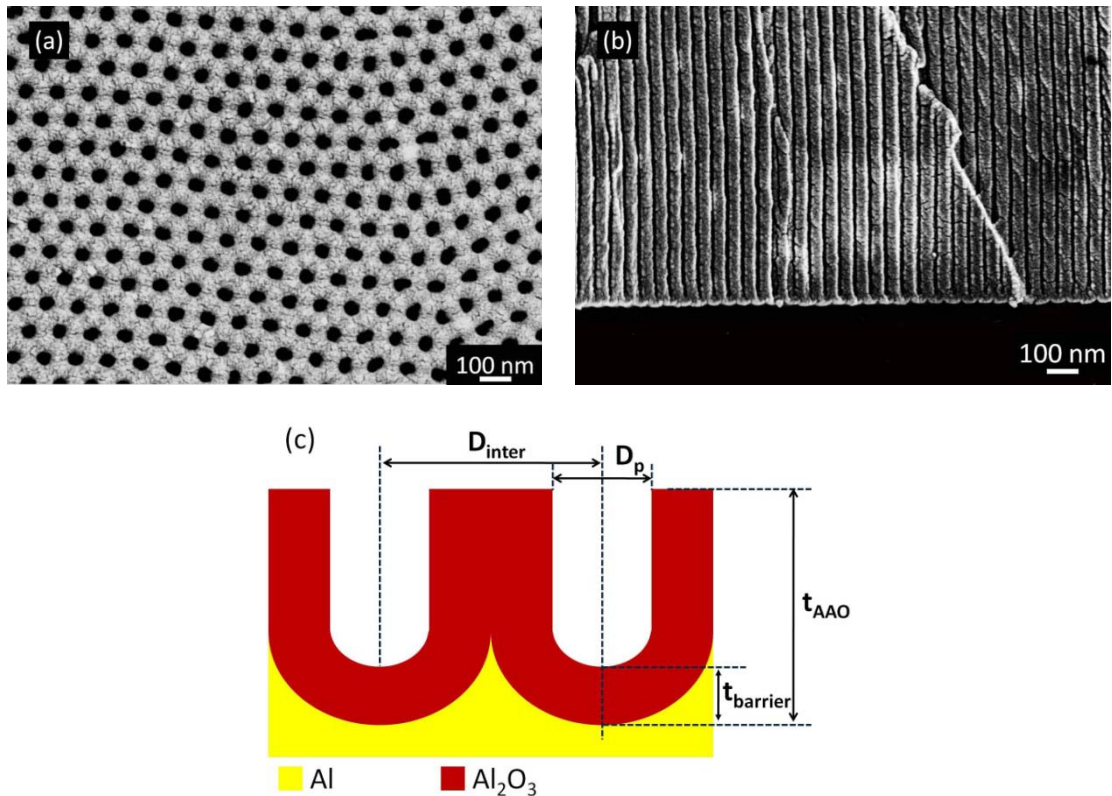


Figure 14. Typical SEM micrographs of (a) top view and (b) side view for ordered AAO templates; (c) schematic drawings for AAO template parameters.

It is observed that ~40 nm pores with ~110 nm interpore distance are hexagonally ordered arranged in porous AAO (Figure 14(a)), while the paralleling channels have a ~50 nm thickness barrier layer at pore bottom in the cross section (Figure 14(b)).

- Specific electrochemical anodization window

To produce ordered AAO templates, a relatively narrow electrochemistry window depending experimental conditions [68] (electrolyte species and concentrations, applied voltages and temperature) is identified. Table 1 summarizes typical conditions for ordered AAO templates fabrication.

Table 1. Typical conditions for ordered AAO templates fabrication.

Electrolyte type / Concentration	Temperature (°C)	Applied Voltages (V)	D _{int} (nm)	Ref.
H ₂ SO ₄ / 20 wt%	1	19	50	[82]
H ₂ SO ₄ / 0.3 M	10	25	60	[55, 83]
H ₂ C ₂ O ₄ / 0.3 M	1	40	95	[55, 63]
H ₃ PO ₄ / 10 wt%	3	160	420	[55]
H ₃ PO ₄ / 0.1 M	0	195	501	[84]

H₂SO₄, H₂C₂O₄ and H₃PO₄ are mostly used electrolytes in references [55, 84]. For H₂SO₄, a variation of anodization temperature within 0-10 °C does not severely affect the ordering of pores in AAO. However, higher temperatures may destroy the AAO templates due to the increased acidity of H₂SO₄ [85]. For H₃PO₄, anodization is performed at high applied voltages. The working temperature must be strictly controlled to < 4 °C since this higher voltage anodization produces a larger amount of heat locally, thus could destroy the AAO templates [55]. For H₂C₂O₄, a working temperature from 0-20 °C is acceptable to fabricate ordered AAO templates [41].

The quality of the pore ordering in AAO templates mostly depends on the anodization

voltage. For example, when Al anodizes in 0.3 M $\text{H}_2\text{C}_2\text{O}_4$, the optimum ordered AAO template is obtained at 40 V. When the voltage is increased to 60V or decrease to 30 V, the ordering in the sample is reduced where a significant amount of disordered domains are produced [82].

The ordered AAO template can be detached from the remaining Al substrate. This is normally done by chemically dissolve Al in a saturated metal salt solution, e.g. an HgCl_2 [99], a CuCl_2 [100] or a CuSO_4 [101] solution at ambient temperature. Further on, the barrier alumina layer at the pore bottom of the AAO template can be removed by chemical dissolution in a dilute H_3PO_4 solution [102, 103]. Xu et al. [103] made AAO templates in 0.3 M $\text{H}_2\text{C}_2\text{O}_4$ at 40 V of 12 °C. The dissolution rate of this barrier layer in 0.5 M H_3PO_4 solution at 30 °C was found to be approximately at 1.3 nm/min.

1.3.5. AAO Template Assisted Synthesis of 1D Nanomaterials

The ordered AAO template has been proven to be a versatile and inexpensive method for the synthesis of 1D nanomaterials. A great variety of nanoscale materials including nanopores, nanowires, nanotubes and carbon nanotubes have been successfully fabricated with the assistance of AAO templates.

Figure 15 shows a schematic setup for the electrochemical deposition method, which shares the same principle as the electroplating. In this method, the AAO template is used as the working electrode. It is deposited with a 200 nm layer of Au on its back side to ensure electrical conductivity.

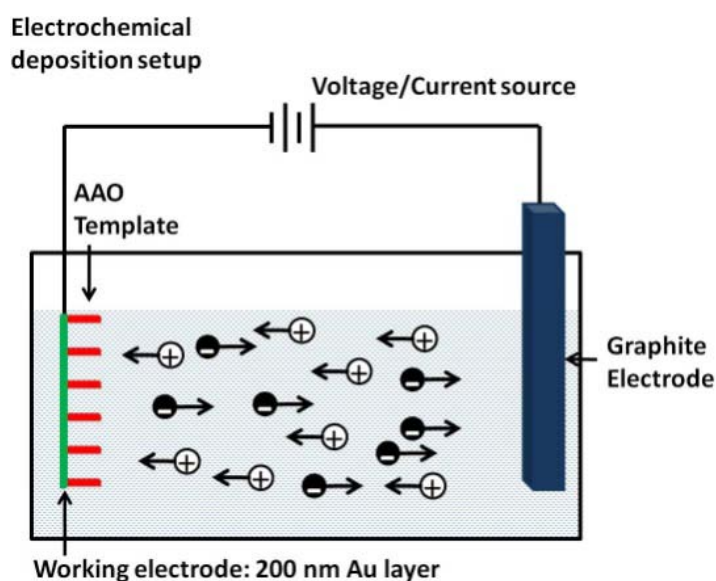


Figure 15. Schematic setup for the electrochemical deposition method

Driven by the applied electrical field during electrochemical deposition, the cations of metallic element(s) are migrating into the pores of AAO templates, and reduced on the Au layer. Within the confined space of pore channels, the nanostructured materials can grow. Nanowires are the mostly formed structures, including pure element of Au [86], Ag [87, 88], Cu [89, 90], Fe [91, 92], Ni [93], Co [94], Pb [95], Bi [96], Sb [97], Pd [98] and Zn [99], and alloys of CuNi [100], CoFe [101], CoNi [102], CoPb [103], CoPt [104], FeNi [105], FePb [106], NiZn [107] and NiPb [108].

It is widely observed that the deposited nanowires grow along different orientations, which can be efficiently adjusted by the experimental parameters (e.g., deposition potentials). The orientations include both the normal direction of the close-packed plane (i.e., $[0001]_{\text{hcp}}$ [94] and $[111]_{\text{fcc}}$ [93]) and some non close-packed planes (i.e., $[10\bar{1}0]_{\text{hcp}}$ [94] and $[110]_{\text{fcc}}$ [93]).

From a thermodynamic point of view, nanowires should grow in directions normal to the close-packed planes to preserve the lowest surface energy. Many examples of these have been reported (0001_{hcp} and 111_{fcc}) is favorable for crystal nucleation and growth along its normal direction during the electrodeposition process.

Some nanowires are found to grow along the normal of non close-packed planes. This is usually explained by a stabilization effect resulted from selective chemical adsorption on specific crystallographic planes. For example, Pan et al. [93, 109] proposed H^+ ions in electrolyte are preferred to stabilize the high surface energy faces (e.g., $(110)_{fcc}$) by surface adsorption, thus decreased the surface energy of these planes extrinsically. This effect could facilitate the growth of nanowires along the normal direction (e.g., $[110]_{fcc}$) of high surface energy planes during electrodeposition [109-111]. Nevertheless, this explanation is still speculative with little direct experimental evidence.

In this thesis, it is proposed a criterion which demonstrates that at low deposition potentials, the wire orientation is determined by the criterion of minimum total surface energy, with the close-packed surface forming the exterior of the crystals. At the high deposition potentials, the crystal axial orientation is predominantly determined by the growth kinetics, i.e., close packed directions and coordination number of the growth plane.

1.4. Thesis Overview

The thesis is arranged as a series of 5 papers, including 2 published, 2 submitted and 1 to be submitted papers. Below is an overview of the structure of the thesis.

1.4.1. Chapter 1 (Introduction)

Chapter 1 has provided a concise literature review on electrochemical anodization of metals, including general morphologies of anodized materials, current knowledge in the formation mechanisms of anodized materials and application of porous alumina templates in nanowires synthesis. The review has identified the problems in current literature leading to the objectives of this thesis. The objective of the thesis can be

summarized as following:

1. To synthesize new anodized materials for functional applications.
2. To study the underlying principles governing the morphologies of anodized materials.
3. To use porous anodized alumina as templates in further synthesis of metallic nanowires.

1.4.2. Chapter 2 (Paper 1)

Preparation of nanoporous tin oxide by electrochemical anodization in alkaline electrolytes: Mingliang Wang, Yinong Liu, Dongfeng Xue, Dongke Zhang, Hong Yang, *Electrochimica Acta*, 56 (2011) 8797-8801.

This paper reports the creation of a porous tin oxide structure by means of anodization of pure tin foil in alkaline NaOH solutions. The tin oxide film produced is polycrystalline and possesses an irregular nanoporous structure. The porosity of the oxide film is ~ 50% and the average pore size is ~37 nm irrespective of anodization conditions, including the applied voltage (5-15 V) and NaOH concentration (0.125-1 M). Linear relationships are observed for the dependence of tin oxide layer thickness on anodization time, applied voltage, and NaOH concentration. A thermodynamic model is established to explain the pore growth mechanism in the tin anodization process.

1.4.3. Chapter 3 (Paper 2)

Current oscillations during potentiostatic anodization of tin in alkaline electrolytes: Mingliang Wang, Hong Yang, Yinong Liu, *Electrochimica Acta* 56 (2011) 7051-7057.

This work discusses a phenomenon of spontaneous periodical current oscillation during electrochemical anodization of tin in alkaline electrolytes. Such phenomenon has been reported in the literature. Attempts have been made in the literature to explain this phenomenon on the basis of oxide film lift-off and electrolyte diffusion. This study demonstrates that the current oscillation is caused by oxygen generation and release on the tin anode, causing periodic redistribution of ion concentration in the electrolyte. The analysis also enables determination of the contributions of the two anodic reactions of Sn oxidation and oxygen generation to the total anodic current.

1.4.4. Chapter 4 (Paper 3)

Anodization process of Sn in oxalic acid at low applied voltages: Mingliang Wang, Yinong Liu, Dongke Zhang, Hong Yang, submitted to *Electrochimica Acta*, August 2011.

This work investigates the anodization of tin in oxalic acid electrolyte at low applied voltages of $U \leq 5$ V. Under such conditions, the anodization product consists of micron-sized SnC_2O_4 crystalline particles. The morphology of the product changes during the anodization process in three distinctive stages. In the initial stage I, Sn dissolves into the electrolyte at high current density. This process is associated with the precipitation of highly oriented SnC_2O_4 crystals on the Sn surface. Stage II is a passivation process associated with the formation of a SnC_2O_4 surface layer with unique pyramidal microstructure via in-situ conversion. Stage III is the localized creation of smaller SnC_2O_4 polyhedron crystals. The anodic reaction mechanisms for each stage are discussed in detail and a mathematical model is established to quantify the critical condition that induces the anodic passivation.

1.4.5. Chapter 5 (Paper 4)

A unified thermodynamic theory for the formation of anodized metal oxide structures: Mingliang Wang, Yinong Liu and Hong Yang, submitted to Acta Materialia, September 2011.

In this work, a unified theory describing the rules governing the formation of various oxide and metal nanostructures via electrochemical anodization has been proposed. This unified theory, based on thermodynamic and electrochemical principles, explains that the formation of porous or compact metal oxide and porous metal structures is dictated by the reaction free energy balance between the electrochemical anodic formation of the metal oxide and the chemical dissolution of the metal oxide in the electrolyte. Based on this theory, a range of key experimental observations reported in the literature are explained, including (1) the selection of the formation of compact oxide, porous oxide or porous metal during anodization, (2) voltage dependence of thickness of compact oxides, (3) thickness dependence of porous oxides, and (4) in-situ pore perforation by step-wise reduction of anodization voltage.

1.4.6. Chapter 6 (Paper 5)

Growth orientation control of Co nanowires fabricated by electro-deposition method using porous alumina templates: Mingliang Wang, Yinong Liu and Hong Yang, submitted to Crystal Growth & Design, October 2011.

In this paper we propose an analysis as generic criteria for preferential orientation growth of metallic nanowires during electrochemical deposition using nano-channel templates. In this work pure Co nanowire arrays were synthesized by electrochemical deposition using porous anodized aluminium oxide templates. The nanowire arrays are found to exhibit near complete preferential single orientation long the wire axis. The preferential orientation is found to change with increasing the deposition voltage,

from $[0002]_{\text{hcp}}$, $[10\bar{1}0]_{\text{hcp}}$, $[1\bar{2}10]_{\text{hcp}}$ to $[110]_{\text{fcc}}$. The observation is explained in terms of nucleation thermodynamics and crystal growth kinetics. The analysis demonstrates that at low deposition potentials, the wire orientation is determined by the criterion of minimum total surface energy, with the close-packed surface forming the exterior of the crystals. At the high deposition potentials, the crystal axial orientation is predominantly determined by the growth kinetics, i.e., close packed directions and coordination number of the growth plane. These criteria also appear to apply well to the preferential growth of fcc metal nanowires, e.g., Ag, Au, Cu and Ni.

1.4.7. Chapter 7 (Closing Remarks)

The final chapter presents the closing remarks on this thesis by the author.

References

- [1] R. P. Feynman, Eng. Sci. 23 (1960) 22-36.
- [2] S. V. N. T. Kuchibhatla, A. S. Karakoti, D. Bera, S. Seal, Prog. Mater Sci. 52 (2007) 699-913.
- [3] V. T. Yadugiri, R. Malhotra, Current Science 99 (2010) 900-907.
- [4] D. B. Warheit, Toxicol. Sci. 101 (2008) 183-185.
- [5] The Scale of Things - Nanometers and More, [http://www.umt.edu/ethics/Debating%20Science%20Program/ODC/NanoODC/Intro/Properties/Nanoscale the scale of things.aspx](http://www.umt.edu/ethics/Debating%20Science%20Program/ODC/NanoODC/Intro/Properties/Nanoscale%20the%20scale%20of%20things.aspx).
- [6] Nano Size, <http://www.nano.gov/nanotech-101/what/nano-size>.
- [7] G. Lövestam, H. Rauscher, G. Roebben, B. S. Klüttgen, N. Gibson, J.-P. Putaud, H. Stamm, Considerations on a Definition of Nanomaterial for Regulatory Purposes, in: Luxembourg: Publications Office of the European Union, 2010, pp. 1-40.
- [8] A. P. Alivisatos, Journal of Physical and Chemistry 100 (1996) 13226-13239.
- [9] Y.-X. Chen, S.-P. Chen, Z.-Y. Zhou, N. Tian, Y.-X. Jiang, S.-G. Sun, Y. Ding, Z. L.

- Wang, *J. Am. Chem. Soc.* 131 (2009) 10860-10862.
- [10] S. E. Skrabalak, J. Chen, Y. Sun, X. Lu, L. Au, C. M. Cobley, Y. Xia, *Acc. Chem. Res.* 41 (2008) 1587-1595.
- [11] P. X. Gao, Y. Ding, W. Mai, W. L. Hughes, C. Lao, Z. L. Wang, *Science* 309 (2005) 1700-1704.
- [12] J. B. Hannon, S. Kodambaka, F. M. Ross, R. M. Tromp, *Nature* 440 (2006) 69-71.
- [13] H. Masuda, K. Fukuda, *Science* 268 (1995) 1466-1468.
- [14] H. S. Shin, J. Yu, J. Y. Song, *Appl. Phys. Lett.* 91 (2007) 173106.
- [15] I. Paramasivam, J. M. Macak, P. Schmuki, *Electrochem. Commun.* 10 (2008) 71-75.
- [16] F. Schmidt-Stein, R. Hahn, J.-F. Gnichwitz, Y. Song, N. K. Shrestha, A. Hirsch, P. Schmuki, *Electrochem. Commun.* 11 (2009) 2077-2080.
- [17] E. Balaur, J. M. Macak, L. Taveira, P. Schmuki, *Electrochem. Commun.* 7 (2005) 1066-1070.
- [18] E. Balaur, J. M. Macak, H. Tsuchiya, P. Schmuki, *J. Mater. Chem.* 15 (2005) 4488-4491.
- [19] K. Shankar, James I. Basham, N. K. Allam, O. K. Varghese, G. K. Mor, X. Feng, M. Paulose, J. A. Seabold, K.-S. Choi, C. A. Grimes, *J. Phys. Chem. C* 113 (2009) 6327-6359.
- [20] G. K. Mor, K. Shankar, M. Paulose, O. K. Varghese, C. A. Grimes, *Appl. Phys. Lett.* 91 (2007) 152111.
- [21] J. R. Jennings, A. Ghicov, L. M. Peter, P. Schmuki, A. B. Walker, *J. Am. Chem. Soc.* 130 (2008) 13364-13372.
- [22] F. Keller, M. S. Hunter, D. L. Robinson, *J. Electrochem. Soc.* 100 (1953) 411-419
- [23] T. Qiu, Y. Zhou, J. Li, W. Zhang, X. Lang, T. Cui, P. K. Chu, *Journal of Physics. D: Applied Physics* 42 (2009) 175403-175407.
- [24] K. Shankar, G. K. Mor, H. E. Prakasam, S. Yoriya, M. Paulose, O. K. Varghese, C. A. Grimes, *Nanotechnology* 18 (2007) 065707.
- [25] K. Varghese, M. Paulose, C. A. Grimes, *Nat. Nanotechnol.* 4 (2009) 592-597.
- [26] A. Ghicov, P. Schmuki, *Chem. Commun.* (2009) 2791-2808.

- [27] S. Rani, S. C. Roy, M. Paulose, O. K. Varghese, G. K. Mor, S. Kim, S. Yoriya, T. J. LaTempa, C. A. Grimes, *Phys. Chem. Chem. Phys.* 12 (2010) 2780-2800.
- [28] G. K. Mor, K. Shankar, M. Paulose, O. K. Varghese, C. A. Grimes, *Nano Lett.* 6 (2006) 215-218.
- [29] P. G. Harrison, C. Bailey, W. Azelee, *J. Catal.* 186 (1999) 147-159.
- [30] Z. Miao, Y. Wu, X. Zhang, Z. Liu, B. Han, K. Ding, G. An, *J. Mater. Chem.* 17 (2007) 1791-1796.
- [31] G. Croft, M. J. Fuller, *Nature* 269 (1977) 585-586.
- [32] X. W. Lou, D. Deng, J. Y. Lee, L. A. Archer, *Chem. Mater.* 20 (2008) 6562-6566.
- [33] D. Larcher, S. Beattie, M. Morcrette, K. Edström, J.-C. Jumas, J.-M. Tarascon, *J. Mater. Chem.* 17 (2007) 3759-3772.
- [34] X. W. Lou, L. A. Archer, Z. Yang, *Adv. Mater.* 20 (2008) 3987-4019.
- [35] X. W. Lou, Y. Wang, C. Yuan, J. Y. Lee, L. A. Archer, *Adv. Mater.* 18 (2006) 2325-2329.
- [36] X. W. Lou, J. S. Chen, P. Chen, L. A. Archer, *Chem. Mater.* 21 (2009) 2868-2874.
- [37] X. W. Lou, C. M. Li, L. A. Archer, *Adv. Mater.* 21 (2009) 2536-2539.
- [38] J.-H. Jeun, S.-H. Hong, *Sens. Actuators, B* 151 (2010) 1-7.
- [39] J.-H. Jeun, H.-S. Ryu, S.-H. Hong, *J. Electrochem. Soc.* 156 (2009) J263-J266.
- [40] H.-C. Shin, J. Dong, M. Liu, *Adv. Mater.* 16 (2004) 237-240.
- [41] S. Shingubara, *J. Nanopart. Res.* 5 (2003) 17-30.
- [42] J. W. Diggle, T. C. Downie, C. W. Goulding, *Chemical Review* 69 (1969) 365-405.
- [43] D. Gong, C. A. Grimes, O. K. Varghese, W. Hu, R. S. Singh, Z. Chen, E. C. Dickey, *J. Mater. Res.* 16 (2001) 3331-3334.
- [44] R. Beranek, H. Hildebrand, P. Schmuki, *Electrochem. Solid-State Lett.* 6 (2003) B12-B14.
- [45] H. Hirakata, K. Ito, A. Yonezu, H. Tsuchiya, S. Fujimoto, K. Minoshima, *Acta Mater.* 58 (2010) 4956-4967.
- [46] F. Schmidt-Stein, S. Thiemann, S. Berger, R. Hahn, P. Schmuki, *Acta Mater.* 58

(2010) 6317-6323.

- [47] J. Choi, J. H. Li, S. C. Lee, J. H. Chang, K. J. Kim, M. A. Cho, *Electrochim. Acta* 51 (2006) 5502-5507.
- [48] I. Sieber, B. Kannan, P. Schmuki, *Electrochem. Solid-State Lett.* 8 (2005) J10-J12.
- [49] X. Feng, T. J. LaTempa, J. I. Basham, G. K. Mor, O. K. Varghese, C. A. Grimes, *Nano Lett.* 10 (2010) 948-952.
- [50] H. Zheng, A. Z. Sadek, K. Latham, K. Kalantar-Zadeh, *Electrochem. Commun.* 11 (2009) 768-771.
- [51] H. Tsuchiya, P. Schmuki, *Electrochem. Commun.* 6 (2004) 1131-1134.
- [52] T. J. LaTempa, X. Feng, M. Paulose, C. A. Grimes, *J. Phys. Chem. C* 113 (2009) 16293-16298.
- [53] H. E. Prakasam, O. K. Varghese, M. Paulose, G. K. Morand, C. A. Grimes, *Nanotechnology* 17 (2006) 4285-4291.
- [54] N. K. Shrestha, M. Yang, P. Schmuki, *Electrochem. Solid-State Lett.* 13 (2010) 21-24.
- [55] A. P. Li, F. Müller, A. Birner, K. Nielsch, U. Gösele, *J. Appl. Phys.* 84 (1998) 6023-6026.
- [56] A. Ghicov, H. Tsuchiya, J. M. Macak, P. Schmuki, *Electrochem. Commun.* 7 (2005) 505-509.
- [57] M. Wang, Y. Liu, D. Xue, D. Zhang, H. Yang, *Electrochim. Acta* 56 (2011) 8797-8801.
- [58] R. C. Furneaux, G. E. Thompson, G. C. Wood, *Corros. Sci.* 18 (1978) 853-881.
- [59] J. P. O'Sullivan, G. C. Wood, *The Proceedings of the Royal Society of London A* 317 (1970) 511-543.
- [60] G. E. Thompson, G. C. Wood, *Anodic Films on Aluminum*, in: J. C. Scully (Ed.) *Treatise on Materials Science and Technology*, vol 23, Academic Press, New York, 1983, pp. 205-329.
- [61] G. E. Thompson, *Thin Solid Films* 297 (1997) 192-201
- [62] G. E. Thompson, R. C. Furneaux, G. C. Wood, J. A. Richardson, J. S. Goode, *Nature* 272 (1978) 433-435.

- [63] W. Lee, R. Ji, U. Gösele, K. Nielsch, *Nat. Mater.* 5 (2006) 741-747.
- [64] F. Li, L. Zhang, R. M. Metzger, *Chem. Mater.* 10 (1998) 2470-2480.
- [65] S. K. Thamida, H.-C. Chang, *Chaos* 12 (2002) 240-251.
- [66] K. Shimizu, G. E. Thompson, G. C. Wood, Y. Xu, *Thin Solid Films* 88 (1982) 255-262.
- [67] J. Oh, Porous anodic aluminum oxide scaffolds; formation mechanisms and applications, in: Department of Materials Science and Engineering, vol Ph.D, Massachusetts Institute of Technology, Cambridge, Massachusetts 02139, United States, 2010, p. 161.
- [68] G. D. Sulka, Highly Ordered Anodic Porous Alumina Formation by Self-Organized Anodizing, in: A. Eftekhari (Ed.) *Nanostructured Materials in Electrochemistry*, Wiley-VCH Verlag GmbH & Co. KGaA, Weinheim, Germany, 2008.
- [69] V. P. Parkhutik, V. I. Shershulsky, *J. Phys. D: Appl. Phys.* 25 (1992) 1258-1263.
- [70] R. Krishnan, Templated self-assembly of nanoporous alumina: pore formation and ordering mechanisms, methodologies, and applications, in: Department of Materials Science and Engineering, vol Ph.D, Massachusetts Institute of Technology, Cambridge, Massachusetts 02139, United States, 2005, p. 324.
- [71] K. S. Raja, M. Misra, K. Paramguru, *Electrochim. Acta* 51 (2005) 154-165
- [72] J. Oh, C. V. Thompson, *Electrochim. Acta* 56 (2011) 4044-4051.
- [73] T. P. Hoar, N. F. Mott, *J. Phys. Chem. Solids* 9 (1959) 97-99
- [74] M. S. Hunter, P. Fowle, *J. Electrochem. Soc.* 101 (1954) 514-519.
- [75] S. J. Garcia-Vergara, P. Skeldon, G. E. Thompson, H. Habazaki, *Electrochim. Acta* 52 (2006) 681-687.
- [76] S. J. Garcia-Vergara, P. Skeldon, G. E. Thompson, H. Habazaki, *Thin Solid Films* 515 (2007) 5418-5423.
- [77] S. J. Garcia-Vergara, P. Skeldon, G. E. Thompson, H. Habazaki, *Surface Interface Analysis* 39 (2007).
- [78] S. J. Garcia-Vergara, P. Skeldon, G. E. Thompson, H. Habakaki, *Corros. Sci.* 49 (2007) 3696-3704.
- [79] S. J. Garcia-Vergara, P. Skeldon, G. E. Thompson, H. Habakaki, *Appl. Surf. Sci.*

254 (2007) 1534-1542.

- [80] S. J. Garcia-Vergara, P. Skeldon, G. E. Thompson, H. Habazaki, *Surf. Coat. Technol.* 201 (2007) 9506-9511.
- [81] A. L. Friedman, D. Brittain, L. Menon, *J. Chem. Phys.* 127 (2007) 154717
- [82] O. Jessensky, F. Müller, U. Gösele, *Appl. Phys. Lett.* 72 (1998) 1173-1175.
- [83] O. Jessensky, F. Müller, U. Gösele, *J. Electrochem. Soc.* 145 (1998) 3735-3740.
- [84] K. Nielsch, J. Choi, K. Schwirn, R. B. Wehrspohn, U. Gösele, *Nano Lett.* 2 (2002) 677-680.
- [85] S. Ono, M. Saito, M. Ishiguro, H. Asoh, *J. Electrochem. Soc.* 151 (2004) B473-B478.
- [86] M. Tian, J. Wang, J. Kurtz, T. E. Mallouk, M. H. W. Chan, *Nano Lett.* 3 (2003) 919-923.
- [87] X. Liu, J. Luo, J. Zhu, *Nano Lett.* 6 (2006) 408-412.
- [88] G. Riveros, S. Green, A. Cortes, H. Gomez, R. E. Marotti, E. A. Dalchiele, *Nanotechnology* 17 (2006) 561-570.
- [89] T. Gao, G. W. Meng, J. Zhang, Y. W. Wang, C. H. Liang, J. C. Fan, L. D. Zhang, *Applied Physics A Materials Science & Processing* 73 (2001) 251-254.
- [90] T. Gao, G. Meng, Y. Wang, S. Sun, L. Zhang, *Journal of Physics. D: Applied Physics* 14 (2002) 355-363.
- [91] S. Yang, H. Zhu, D. Yu, Z. Jin, S. Tang, Y. iDu, *J. Magn. Magn. Mater.* 222 (2000) 97-100.
- [92] J. M. Baik, M. Schierhorn, M. Moskovits, *J. Phys. Chem. C* 112 (2008) 2252-2255.
- [93] H. Pan, H. Sun, C. Poh, Y. Feng, J. Lin, *Nanotechnology* 16 (2005) 1559-1564.
- [94] M. Darques, A. Encinas, L. Vila, L. Piraux, *J. Phys. D: Appl. Phys* 37 (2004) 1411-1416.
- [95] G. Yi, W. Schwarzacher, *Appl. Phys. Lett.* 74 (1999).
- [96] L. Li, Y. Yang, X. Fang, M. Kong, G. Li, L. Zhang, *Solid State Commun.* 141 (2007) 492-496.
- [97] Y. Zhang, L. Li, G. H. Li, L. D. Zhang, *Physical Review B* 73 (2006) 113403.

- [98] C. Xu, H. Wang, P. K. Shen, S. P. Jiang, *Adv. Mater.* 19 (2007) 4256-4259.
- [99] J.-G. Wang, M.-L. Tian, N. Kumar, T. E. Mallouk, *Nano Lett.* 5 (2005) 1247-1253.
- [100] C. Z. Wang, G. W. Meng, Q. Q. Fang, X. S. Peng, Y. W. Wang, Q. Fang, L. D. Zhang, *J. Phys. D: Appl. Phys.* 35 (2002) 738-741.
- [101] H. L. Su, G. B. Ji, S. L. Tang, W. Chen, Z. Li, B. X. Gu, Y. W. Du, *J. Appl. Phys.* 97 (2005) 116104.
- [102] H. Zhua, S. Yang, G. Nia, D. Yu, Y. Du, *Scr. Mater.* 44 (2001) 2291-2295
- [103] G. B. Ji, S. L. Tang, B. X. Gu, Y. W. Du, *Journal of Physical Chemistry B* 108 (2004) 8862-8865.
- [104] T. R. Gao, L. F. Yin, C. S. Tian, M. Lu, H. Sang, S. M. Zhou, *J. Magn. Magn. Mater.* 300 (2006) 471-478.
- [105] Q. F. Liu, C. X. Gao, J. J. Xiao, D. S. Xue, *J. Magn. Magn. Mater.* 260 (2003) 151-155.
- [106] X. L. Fei, S. L. Tang, R. L. Wang, H. L. Su, Y. W. Du, *Solid State Commun.* 141 (2007) 25-28.
- [107] L. Liu, H. Li, S. Fan, J. Gu, Y. Li, H. Sun, *J. Magn. Magn. Mater.* 321 (2009) 3511-3514
- [108] G. Ji, J. Cao, F. Zhang, G. Xu, H. Su, S. Tang, B. Gu, Y. Du, *J. Phys. Chem. B* 109 (2005) 17100-17106.
- [109] H. Pan, B. Liu, J. Yi, C. Poh, S. Lim, J. Ding, Y. Feng, C. H. A. Huan, J. Lin, *J. Phys. Chem. B* 109 (2005) 3094-3098.
- [110] M. Paunovic, M. Schlesinger, *Fundamentals of Electrochemical Deposition*, Wiley, New York, 1998.
- [111] H. Sun, X. Li, Y. Chen, W. Li, F. Li, B. Liu, X. Zhang, *Nanotechnology* 19 (2008) 225601.

CHAPTER 2. Preparation of Nanoporous Tin Oxide by Electrochemical Anodization in Alkaline Electrolytes

Mingliang Wang, Yinong Liu, Dongfeng Xue, Dongke Zhang and Hong Yang

Electrochimica Acta, 56 (2011) 8797-8801

Abstract

This paper reports the creation of a porous tin oxide structure by means of anodization of pure tin foil in alkaline NaOH solutions. The tin oxide film is polycrystalline and possesses an irregular nanoporous structure. The porosity of the oxide film is ~ 50% and the average pore size is ~37 nm irrespective of anodization conditions, including the applied voltage (5-15 V) and NaOH concentration (0.125-1 M). The BET specific surface area of this porous structure is 79.6 m²/g. Linear relationships are observed for the dependence of tin oxide layer thickness on anodization time, applied voltage, and NaOH concentration. A thermodynamics model is established to explain the pore growth mechanism in the anodization process.

Keywords: tin oxide, anodization, nanoporous materials, electrochemical synthesis

2.1. Introduction

In the last decade, nanoporous structures created by anodization of different metals [1-8] and semiconductors [9-11] have received much attention due to the high technological potentials of these materials as photocatalysts [12, 13], self-cleaning substrates [14, 15], solar cell electrodes [16-18] and luminescence devices [11, 19]. The most widely studied porous structure is alumina created by the anodization of aluminum in acidic aqueous electrolytes [1]. Porous Al_2O_3 films created in this way have highly self-organized nanopores of 10~100 nm in diameter and greater than 100 μm in depth [20]. This highly ordered one-dimensional nanostructure makes anodic alumina ideal template materials for creation of nanowires [1, 21] and as substrates for surface enhanced Raman scattering effect [22].

In comparison to porous alumina, which is chemically inert, tin dioxide is more chemically and electrochemically more active and has the potential to offer more functional properties. Tin dioxide is an n-type semiconductor widely utilized as solid-state gas sensors [23, 24] and oxidation catalysts [25]. It also has the potential to function as high capacity anode materials for lithium-ion batteries [26, 27]. These applications desire a large specific surface area [28]. Despite the very high technological potential, the creation of highly porous tin oxide structures has seldom been reported in the literature [29-31]. Up to date, anodized tin oxide porous structure was only produced in acidic aqueous electrolytes, pioneered by Shin et al. They first reported the successful synthesis of tin oxide structure in oxalic acid by electrochemical anodization of Sn [29]. The anodic tin oxide film produced has a distinctive irregular pore arrangement with macrocracks formed perpendicular to the growth direction [29].

In this paper, we report on the creation of porous tin oxide by means of anodization of

Sn in alkaline NaOH solutions, and propose a thermodynamics model to explain the growth of this porous structure.

2.2. Experimental procedures

Sn foil of 99.99 at% purity and 400 μm thickness was used to create the porous tin oxide. The foil coupons were ultrasonically cleaned in ethanol and deionized water prior to anodization. The electrolyte used was NaOH solutions of concentrations in the range from 0.125 M to 1 M. The anodization experiments were performed at the room temperature in a two-electrode cell using a high purity titanium plate as the cathode. A constant voltage was applied for each experiment, ranging from 5 to 15 V. After the anodizing process, the Sn foil anode was removed from solution, washed several times in deionized water, and dried in air naturally.

The x-ray powder diffraction (XRD) pattern of the anodized foil was obtained using a Siemens D5000 Diffractometer with Cu K_{α} radiation ($\lambda = 0.1542$ nm) at 40 kV and 35 mA. The morphology and composition of the anodic films were further characterized using a field emission scanning electron microscope (Zeiss 1555 FESEM). The average pore diameter (D_{average}) of the porous structures was determined by analyzing the SEM micrographs using the Image J software [32]. The bright field image and selective area electron diffraction (SAED) pattern of the anodized foil were taken using a transmission electron microscope (JEOL 2100).

2.3. Results

Anodization of Sn foil in NaOH solution has resulted in the formation of a SnO_2 film

on the Sn anode, as confirmed by the XRD and TEM results shown in Figure 1. Figure 1(a) shows XRD spectra of two anodized samples. The as-anodized sample was in the original state after anodization and the annealed sample was anodized and then annealed at 110°C for 3 hours. It is seen that the as-anodized sample had poor crystallinity, with two low-intensity broad peaks centered at 33.9° and 55.8°. These peaks can be tentatively assigned to (101) and (211) of SnO₂ (JCPDS: 41-1445). Annealing of the anodized sample improved its crystallinity and resolution of the XRD peaks. The diffraction peaks are fully indexed to SnO₂. Figure 1(b) shows a TEM micrograph of the as-anodized film, displaying highly porous structure. The SAED pattern of this porous structure exhibited faint polycrystalline rings of (110), (101) and (211) of SnO₂, in good agreement with the XRD analysis.

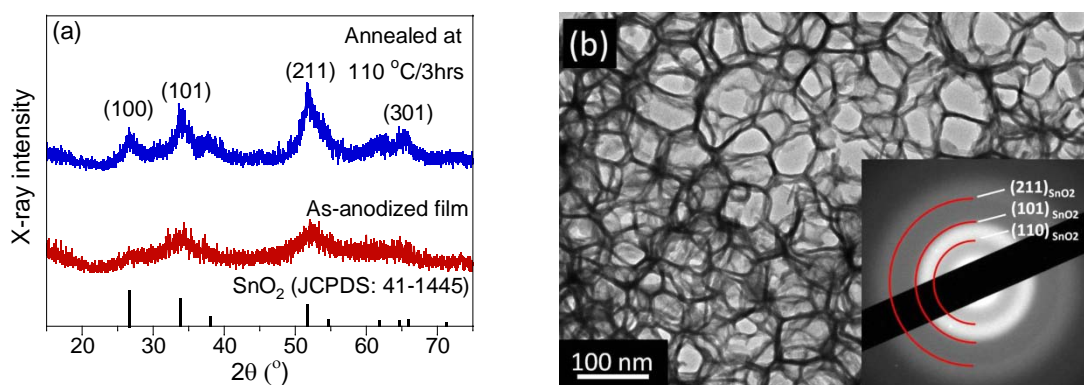


Figure 1. (a) XRD spectra of an as-anodized and annealed tin oxide films. (b) A TEM micrograph of the porous anodized oxide structure. The inset is a SAED pattern showing the diffraction rings of (110), (101) and (211) of SnO₂ (JCPDS: 41-1445).

Figure 2 shows typical SEM images of porous tin oxide formed on the surface of the Sn anode, as of the sample anodized in a 0.5 M NaOH solution at an applied voltage of 12 V for 3000 s. Micrographs (a) and (b) are the top view, micrographs (d) and (e) are the side view and micrograph (f) is a bottom view of the oxide film.

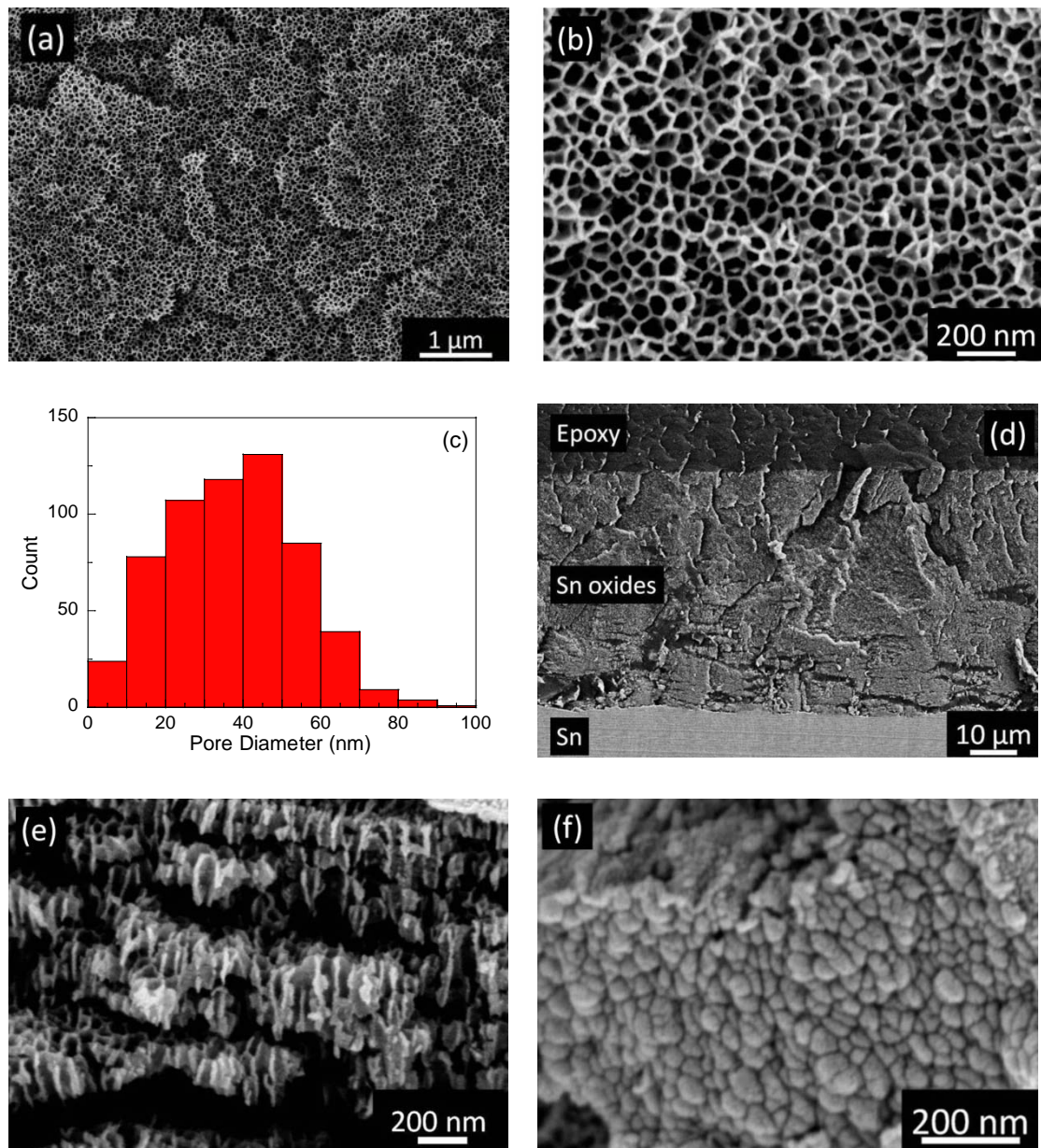


Figure 2. SEM images of an anodized porous SnO₂ film; (a) low and (b) high magnifications (A pore diameter histogram presented in (c)) for top view, (d) low and (e) high magnifications for side view, and (f) bottom view.

It is evident that the pore structure is irregular, unlike the highly ordered hexagonal cell structures observed in anodized alumina [1]. The porosity is estimated to be ~50% and the average pore diameter of this porous structure is ~ 37 nm (Fig. 2b). The pore diameter was derived from the image analysis using Image J distribution of the image

(b), of which the diameters histogram is presented in (c). Determined by BET (Brunauer-Emmett and Teller) technique using scratched anodized powders from the SnO₂ films, the surface area of anodized films was 79.6 m²/g. Micrograph (d) shows that the thickness of this SnO₂ porous film is ~ 50 μm from the side view. The large cracks observed in (d) are not intrinsic and are caused by microtome sectioning of the epoxy-mounted sample. Micrograph (e) is a detailed view of the cross-section of the porous SnO₂ at higher magnification. It is observed that the SnO₂ porous structure consists of nanochannels oriented along the thickness, i.e., growth direction. Some macro cracks perpendicular to the growth direction of the porous structure are clearly visible. This structure is similar to that of the porous tin oxide formed by anodization of Sn in oxalic acid [29]. Micrograph (f) shows the bottom view of a piece of porous film broken away from the metal substrate. It has a convex morphology at the Sn/Sn oxide interface, similar to the anodized porous alumina [33], although it has an irregular arrangement.

Figure 3 shows the effects of anodization parameters on the average pore diameter of porous SnO₂ synthesized, with (a) showing the effect of applied voltage and (b) showing the effect of NaOH concentration. It is evident that the average pore diameter remains constant at ~ 37 nm, irrespective of either of the two parameters. This behavior is very different from that of anodized alumina, where the pore diameter has been found to increase linearly with the applied voltage [20]. However, the dependence of pore diameter on the electrolyte concentration has not achieved a consensus experimentally. Thompson et al. [34] reported a slight increase of pore diameter with the increase of acidic concentration (e.g. sulfuric acid, oxalic acid and phosphorous acid) of the electrolyte for anodization of Al, whereas Krisnan et al. [35] found that the pore size of porous alumina presented an initially drop and then increase trend on the electrolyte concentration in 0~50 wt% H₃PO₄ electrolyte.

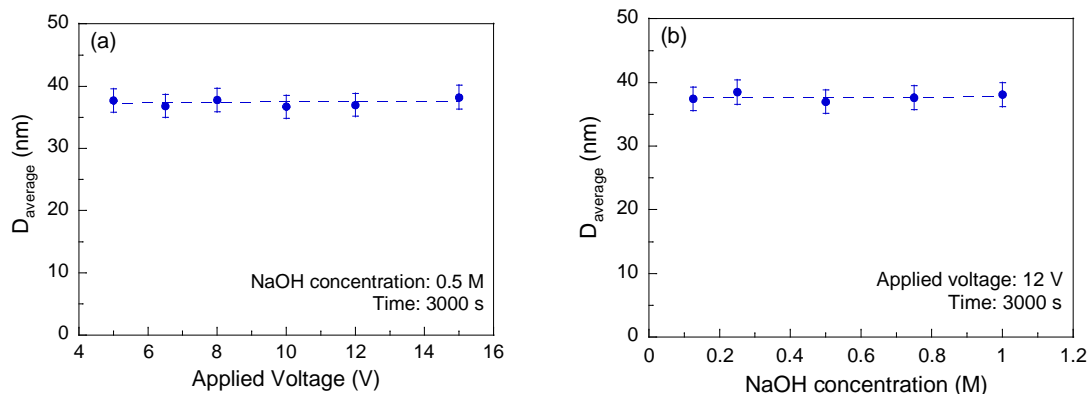


Figure 3. Effects of (a) applied voltage and (b) NaOH concentration on the average pore diameter (D_{average}) of porous SnO_2 film formed.

Figure 4 shows the effects of anodization parameters on the total thickness of the porous SnO_2 films. The thickness of the porous surface layer is determined by means of SEM observation on the cross-section. It is seen that film thickness has linear dependences on anodization time (graph (a)), applied voltage (graph (b)), and NaOH concentration (graph (c)). This behavior implies that the oxide formation kinetics is not affected by the oxide already formed. This is not surprising considering the highly porous nature of the oxide film. The growth rate of this porous SnO_2 film was estimated from Figure 4(a) to be ~ 17 nm/s, at 12 V in 0.5 M NaOH solution. This rate is much faster than the growth rate of anodized porous alumina, typically < 5 nm/s [36, 37], but much slower than the porous tin oxide film produced in 0.27 M oxalic acid solution at 8 V (~ 78 nm/s) [29]. The linear dependence of porous film thickness on the applied voltage is $5.3 \mu\text{m}/\text{V}$ in 0.5 M NaOH solution (for anodization duration of 3000 s). The linear dependence of the porous film thickness on NaOH concentration is $6.2 \mu\text{m}/\text{M}$ at an applied voltage of 12 V (for duration of 3000 s).

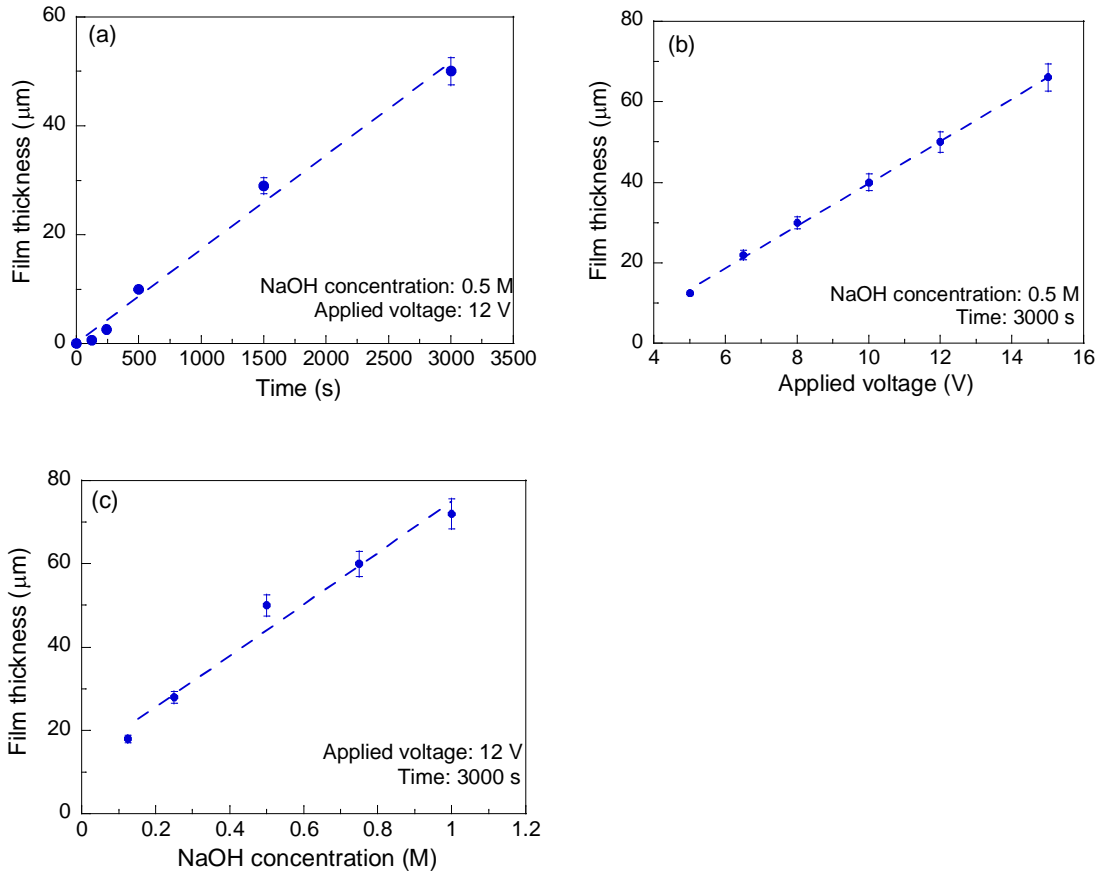


Figure 4. Effects of anodization time (a), applied voltage (b) and NaOH concentration (c) of the electrolyte on the total thickness of anodized tin oxide films.

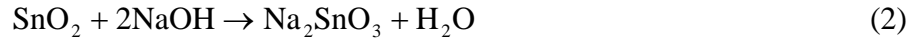
2.4. Discussion

The growth of a porous oxide requires concurrent occurrence of two reactions, one for the formation of metal oxide and the other for the dissolution of the same oxide, literally in the same electrochemical environment [38]. Despite the wide practice of electrochemical synthesis of porous metal oxide films, a consistent explanation of such a mechanism for pore growth is yet to be established.

In the present case of anodization of Sn in NaOH aqueous electrolytes, two reactions may happen: anodic oxidation of Sn into SnO_2 according to reaction (1)



and chemical dissolution of SnO_2 via reaction (2)



Reaction (1) is an electrochemical reaction. Its free energy change obeys Nernst equation and is a function of the electrode potential, or applied voltage. Reaction (2) is a chemical reaction, with a free energy change of -117.02 kJ/mol. The free energy changes of the two reactions may be schematically expressed as shown in Figure 5(a). In this presentation, two critical applied voltages may be identified. U_2 is the applied voltage at which the free energy change of reaction (1) is nil, i.e., $\Delta G_1=0$. Above U_2 reaction (1) occurs and SnO_2 is formed. U_1 is the applied voltage at which the free energy changes of reaction (1) and reaction (2) are equal, i.e., $\Delta G_1=\Delta G_2$. Above U_1 reaction (2) is suppressed and SnO_2 formed is stable. Between U_1 and U_2 both reactions operate.

Figure 5(b) shows a schematic illustration of the growth mechanism for anodized porous oxide. In the case of anodization of Sn in NaOH solution, a significant anodic voltage is applied across the Sn anode and Ti cathode. This applied voltage allows the formation of a stable SnO_2 barrier layer at the Sn/electrolyte interface (point a). During pore growth, the SnO_2 barrier layer and the electrolyte body effectively form an electrical circuit of two resistors in series connection and much of the potential difference between the two electrodes is carried by the SnO_2 layer due to the significantly higher resistance of SnO_2 relative to the electrolyte solution. Potential distribution in the system is schematically expressed by the red line in Figure 5(b). Potential U_a is the applied voltage, at the Sn/ SnO_2 interface (point a). It is well above U_2 , and SnO_2 is promoted to form via reaction (1).

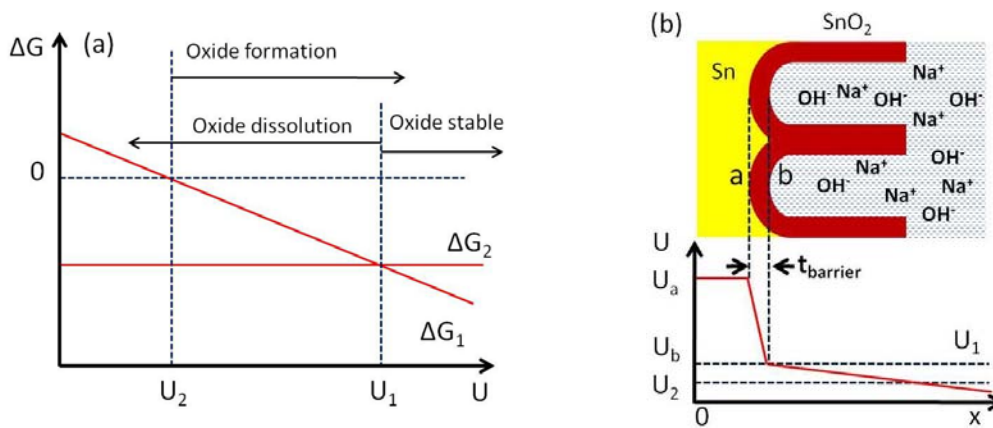


Figure 5. Schematic illustration of the mechanism of formation of anodized porous tin oxide; (a) thermodynamic analysis of the Gibbs free energy (ΔG) for the anodic formation of oxide and chemical dissolution of the oxide in relation to the applied voltage (U); (b) schematic illustration of growth mechanism of anodized porous oxide.

Potential U_b occurs at the SnO_2 /electrolyte interface (point b). It is dictated by the sharing of the circuit resistance between the electrolyte and the oxide, or dictated by the barrier layer thickness. Increase of the thickness of the barrier layer leads to decrease of U_b , until it reaches U_1 . Any further growth of the SnO_2 barrier layer lowers U_b to below U_1 . This leads to the SnO_2 formed being thermodynamically unstable and its chemical dissolution via reaction (2), resulting in the formation of the porous SnO_2 structure observed. The two reactions of electrochemical formation and the chemical dissolution of SnO_2 are self-equilibrated under the condition $U_b=U_1$, thus determining the constant thickness of the barrier layer while the porous film continues to grow in thickness. This growth mechanism also predicts that the thickness of the oxide barrier layer is linearly proportional to the applied voltage for a given electrochemical cell configuration. This agrees well with numerous observations reported in the literature, including Al [33], and Ti [16, 39]. For anodized porous Al_2O_3 , the barrier layer thickness has been reported to have a linear dependence on the applied voltage of $\sim 1.3 \text{ nm/V}$ [40].

2.5. Conclusions

A highly porous tin oxide film with irregular pore structures has been created by means of anodization of Sn in NaOH aqueous solution. This is the first time such structure has been created in alkaline electrolytes. The findings can be more specifically stated as following:

- (1) Anodization of Sn in NaOH solutions of 0.125~1 M concentration under 5-15 V applied voltage is able to produce porous SnO₂ films. The porous structure is random and irregular but uniform. The average pore size is ~37 nm and the porosity is ~50%. These features of the anodized porous SnO₂ films are found to be independent of the anodization conditions used.
- (2) The thickness of the anodized porous SnO₂ film increases linearly with anodization time, applied voltage, and NaOH concentration. The growth rate of the anodized porous SnO₂ film is estimate to be ~17 nm/s at the applied voltage of 12 V in a 0.5 M NaOH solution.
- (3) The formation and growth of the porous structure requires concurrent occurrence of two reactions, for the anodic formation of SnO₂ and the chemical dissolution of the same oxide. A mechanism based on thermodynamic and electrochemical considerations is proposed, and the criterion is identified to be $U_b=U_1$ as defined in Figure 5.

Acknowledgements

M. Wang wishes to acknowledge the scholarship support from the Chinese Scholarship Council and the University of Western Australia. We also acknowledge the experimental support of the Centre for Microscopy, Characterization and

Microanalysis of the University of Western Australia for electron microscopy and microstructure analysis.

References

- [1] H. Masuda, K. Fukuda, *Science* 268 (1995) 1466.
- [2] D. Gong, C. A. Grimes, O. K. Varghese, W. Hu, R. S. Singh, Z. Chen, E. C. Dickey, *J. Mater. Research* 16 (2001) 3331.
- [3] I. Sieber, H. Hildebrand, A. Friedrich, P. Schmuki, *Electrochem. Commun.* 7 (2005) 97.
- [4] H. E. Prakasam, O. K. Varghese, M. Paulose, G. K. Morand, C. A. Grimes, *Nanotechnology* 17 (2006) 4285.
- [5] H. Tsuchiya, T. Akaki, J. Nakataa, D. Terada, N. Tsuji, Y. Koizumi, Y. Minamino, P. Schmuki, S. Fujimoto, *Electrochim. Acta* 54 (2009) 5155.
- [6] H. Tsuchiya, P. Schmuki, *Electrochem. Commun.* 6 (2004) 1131.
- [7] S. E. Kim, J. H. Lim, S. C. Lee, S.-C. Nam, H.-G. Kang, J. Choi, *Electrochim. Acta* 53 (2008) 4846.
- [8] S. J. Kim, J. Lee, J. Choi, *Electrochim. Acta* 53 (2008) 7941.
- [9] S. Bauer, J. G. Brunner, H. Jha, Y. Yasukawa, H. Asoh, S. Ono, H. Böhmc, J. P. Spatz, P. Schmuki, *Electrochem. Commun.* 12 (2010) 565.
- [10] S. -H. Park, K.-W. Lee, Y. -Y. Kim, *Thin Solid Films* 518 (2010) 2860.
- [11] J. C. Vial, A. Bsiesy, F. Gaspard, R. Hérino, M. Ligeon, F. Muller, R. Romestain, R. M. Macfarlane, *Phys. Rev. B* 45 (1992) 14171.
- [12] I. Paramasivam, J. M. Macak, P. Schmuki, *Electrochem. Commun.* 10 (2008) 71.
- [13] F. Schmidt-Stein, R. Hahn, J.-F. Gnichwitz, Y. Song, N. K. Shrestha, A. Hirsch, P. Schmuki, *Electrochem. Commun.* 11 (2009) 2077.
- [14] E. Balaur, J. M. Macak, L. Taveira, P. Schmuki, *Electrochem. Commun.* 7 (2005)

1066.

- [15] E. Balaur, J. M. Macak, H. Tsuchiya, P. Schmuki, *J. Mater. Chem.* 15 (2005) 4488.
- [16] K. Shankar, James I. Basham, N. K. Allam, O. K. Varghese, G. K. Mor, X. Feng, M. Paulose, J. A. Seabold, K.-S. Choi, C. A. Grimes, *J. Phys. Chem. C* 113 (2009) 6327.
- [17] G. K. Mor, K. Shankar, M. Paulose, O. K. Varghese, C. A. Grimes, *Appl. Phys. Lett.* 91 (2007) 152111.
- [18] J. R. Jennings, A. Ghicov, L. M. Peter, P. Schmuki, A. B. Walker, *J. Am. Chem. Soc.* 130 (2008) 13364.
- [19] H. Föll, M. Leisner, A. Cojocaru, J. Carstensen, *Materials* 3 (2010) 3006.
- [20] S. Shingubara, *J. Nanoparticle Research* 5 (2003) 17.
- [21] H. S. Shin, J. Yu, J. Y. Song, *Appl. Phys. Lett.* 91 (2007) 173106.
- [22] T. Qiu, Y. Zhou, J. Li, W. Zhang, X. Lang, T. Cui, P. K. Chu, *J. Phys. D: Appl. Phys.* 42 (2009) 175403.
- [23] Z. Miao, Y. Wu, X. Zhang, Z. Liu, B. Han, K. Ding, G. An, *J. Mater. Chem.* 17 (2007) 1791.
- [24] P. G. Harrison, C. Bailey, W. Azelee, *J. Catalysis* 186 (1999) 147.
- [25] G. Croft, M. J. Fuller, *Nature* 269 (1977) 585.
- [26] Y. Wang, J. Y. Lee, H. C. Zeng, *Chem. Mater.* 17 (2005) 3899.
- [27] X. W. Lou, Y. Wang, C. Yuan, J. Y. Lee, L. A. Archer, *Adv. Mater.* 18 (2006) 2325.
- [28] M. Batzill, U. Diebold, *Prog. Surf. Sci.* 79 (2005) 47.
- [29] H. -C. Shin, J. Dong, M. Liu, *Adv. Mater.* 16 (2004) 237.
- [30] J. -H. Jeun, S. -H. Hong, *Sens. Actuators B* 151 (2010) 1.
- [31] J. -H. Jeun, H. -S. Ryu, S. -H. Hong, *J. Electrochem. Soc.* 156 (2009) 263.
- [32] C. Y. Han, G. A. Willing, Z. Xiao, H. H. Wang, *Langmuir* 23 (2007) 1564.

- [33] O. Jessensky, F. Muller, U. Gösele, *J. Electrochem. Soc.* 145 (1998) 3735.
- [34] G. E. Thompson, G. C. Wood, Anodic Films on Aluminum, in: J. C. Scully (Ed.) *Treatise on Materials Science and Technology*, vol 23, Academic Press, New York, 1983, pp. 205-329.
- [35] R. Krishnan, Templated self-assembly of nanoporous alumina: pore formation and ordering mechanisms, methodologies, and applications, in: Department of Materials Science and Engineering, Ph.D, Massachusetts Institute of Technology, Cambridge, Massachusetts 02139, United States, 2005, p. 324.
- [36] H. Masuda, F. Hasegawa, S. Ono, *J. Electrochem. Soc.* 144 (1997) 127.
- [37] O. Jessensky, F. Muller, U. Gösele, *Appl. Phys. Lett.* 72 (1998) 1173.
- [38] J. M. Macak, H. Tsuchiya, A. Ghicov, K. Yasuda, R. Hahn, S. Bauer, P. Schmuki, *Curr. Opin. Solid State Mater. Sci.* 11 (2007) 3.
- [39] A. Ghicov, P. Schmuki, *Chem. Commun.* (2009) 2791.
- [40] W. Lee, R. Ji, U. Gösele, K. Nielsch, *Nature Mater.* 5 (2006) 741.

CHAPTER 3. Current Oscillations during Potentiostatic Anodization of Tin in Alkaline Electrolytes

Mingliang Wang, Hong Yang and Yinong Liu,

Electrochimica Acta 56 (2011) 7051-7057

Abstract

This paper reports a phenomenon of spontaneous periodical current oscillation during electrochemical anodization of tin in alkaline electrolytes. Such phenomenon has been reported in the literature. Attempts have been made to explain this phenomenon on the basis of oxide film lift-off and electrolyte diffusion. This investigation demonstrates that the current oscillation is caused by oxygen generation and release on the tin anode, causing periodic redistribution of ion concentration in the electrolyte. The analysis also enables determination of the contributions of the two anodic reactions of Sn oxidation and oxygen generation to the total anodic current.

Keywords: tin oxide, anodization, nanoporous materials, electrochemical synthesis, current oscillation

3.1. Introduction

It is well known that electrochemical anodization of various metals (e.g., Al [1], Ti [2, 3], Nb [4], Ta [5, 6], W [7], Zr [8] and Fe [9]) and semiconductors (e.g., Si [10], GaN [11], GaP [12] and CdS [13]) is able to generate intricate nanostructures. These new breed of nanomaterials have attracted much attention due to their high technological potentials in various applications as photocatalysts [14, 15], self-cleaning substrates [16, 17], solar cell electrodes [18-20] and luminescence devices [10, 21]. It is common knowledge that parameters of the electrochemical process have strong influences on the morphology of the anodized structures formed. One such important parameter is the anodic current. Some researchers have reported the observation of spontaneous oscillations of current or voltage [22-27]. Several hypotheses have been proposed to explain this phenomenon.

Parkhutik et al. [25] observed regular voltage oscillations during anodization of Si in ($\text{H}_3\text{PO}_4+\text{HF}$) electrolyte. The periodic drops of the anodization voltage are considered to be caused by the lift-off of the anodized Si oxide film, which may contain random and isotropic micropores at the Si oxide/Si interface. Taveira et al. [26] agreed with this model in their work on anodization synthesis of disordered porous Ti oxide in $(\text{NH}_4)_2\text{SO}_4+\text{NH}_4\text{F}$ solution. They observed the detachment of the disordered TiO_2 porous layer when the voltage oscillation occurred. No direct evidence was given in these studies to demonstrate the time correspondence between the oxide detachment from the metal substrate and the voltage drop.

Lee et al. [27] reported the observation of spontaneous oscillations of current during anodization of aluminum under high voltages. It was reported the anodized alumina films that experienced current oscillatory during anodization exhibited modulated pore structures, and the modulation patterns of the porous structure match exactly the oscillating current profile. The oscillatory behavior was suggested to be controlled by

the diffusion of the electrolyte from the bulk reservoir to the bottom of the nanopores, where the electrochemical activities take place. The deep narrow pore channels create fluid convection barrier and hinder supply of reaction anions for the anodic reaction. Progressive depletion of the anions at the pore bottom results in continuous reduction of the anodic oxidation reaction rate and thus decreases in current density. However, no explanation was given how ionic diffusion may be periodically enhanced to induce the current oscillations.

At the meantime, several authors have reported that gas bubble development may have impacted on the current oscillatory phenomenon in Al [27, 28] and GaP [12] anodization. However, no detailed information was given to explain the co-relation. This study was conducted to elucidate the peculiar phenomenon of current oscillation during anodization of Sn in NaOH solution.

3.2. Experimental procedures

High purity (99.99 at%) tin foil of 400 μm was used as the material for anodization. The foil sample was cut in round shape of $\phi 25$ mm in diameter. The sample coupons were ultrasonically cleaned in ethanol and deionized water prior to anodization. For each experiment, a fresh sample coupon was used. The electrolyte used was NaOH aqueous solution of 0.5 M concentration.

The experimental set up is shown in Figure 1. The anodization was performed at room temperature in a two-electrode cell using titanium metal as the cathode. A constant voltage was instantaneously applied across the two electrodes for each experiment. The applied voltage was varied between 5 and 15 V for different experiments. The corresponding current density-time ($i - t$) curves of the anodization processes were recorded via a computer with a USB-interfaced digital multimeter (DMM 86C). The

Sn anode was located at the end of a cylindrical barrel of $\phi 12 \times 35$ mm. Although magnetic stirring was employed in the bulk electrolyte solution during anodization, no stirring was near the Sn anode.

After the anodization process, the Sn foil anode was removed from solution, washed in deionized water, and dried in air naturally. The morphology of the anodized films was characterized using a field emission scanning electron microscope (Zeiss 1555 FESEM). The average pore diameter and porosity of the porous structures were determined by analyzing the SEM micrographs using Image J software [29].

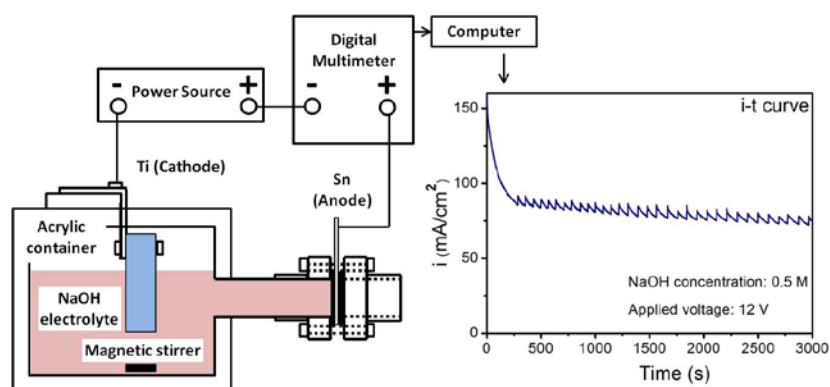


Figure 1. Experimental setup configuration of the Sn anodization experiment

3.3. Results

Figure 2 shows two SEM micrographs of the porous SnO_2 film formed on the surface of the Sn anode after anodization from (a) low and (b) high magnifications. It is seen that the tin oxide produced is highly uniform and porous, with an average pore diameter of ~ 37 nm and porosity of $\sim 50\%$ (Fig. 2b), based on image analysis using Image J.

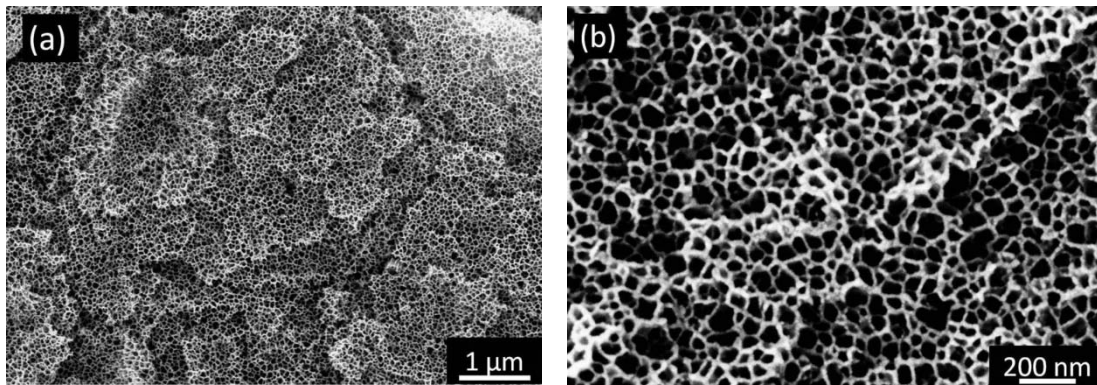


Figure 2. SEM micrographs of a porous SnO₂ film formed by anodization of Sn in 0.5 M NaOH solution at 12 V for 3000 s.

Figure 3 shows the effect of applied voltage on the thickness of the SnO₂ porous layer. Micrograph (a) shows a cross-section view of a sample anodized under 12 V for 500 s. The sample was cut using microtome and unpolished, thus the cracked surface resulting from the sectioning. The anodized layer is ~ 10 μm thick. Figure 3(b) shows the dependence of the film thickness on the time, revealing a linear relationship. The growth rate of this porous SnO₂ film was estimated to be 17 nm/s, at 12 V in 0.5 M NaOH solution.

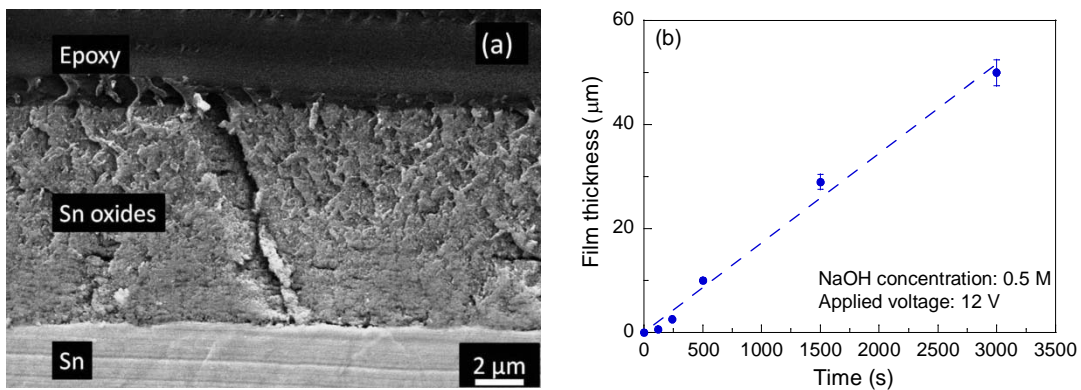


Figure 3. Effect of applied voltage on the thickness of anodized SnO₂ films; (a) SEM micrograph showing cross-section view of a porous SnO₂ film; (b) linear dependence of film thickness on time.

Figure 4 (a) shows current-time (*i* - *t*) curves of anodization at different applied

voltages from 5 to 15 V. For each experiment a constant voltage was applied between the two electrodes. It is seen that there is a progressive decrease of the current with time during the initial stage of anodization, and then a rather regular repetitive oscillation of the current occurred. The current oscillation is spontaneous and self-activated. It is characteristic of a sudden jump followed by a gradual decrease in the same fashion as the initial curve. i_{stable} is defined as the average current density in the stable stage at the end of the measurement (determined in the range from 2500 to 3000 s). Figure 4 (b) shows the linear dependence of i_{stable} on the applied voltage. This implies that the anodic reactions are controlled by mass transfer in the electrolyte.

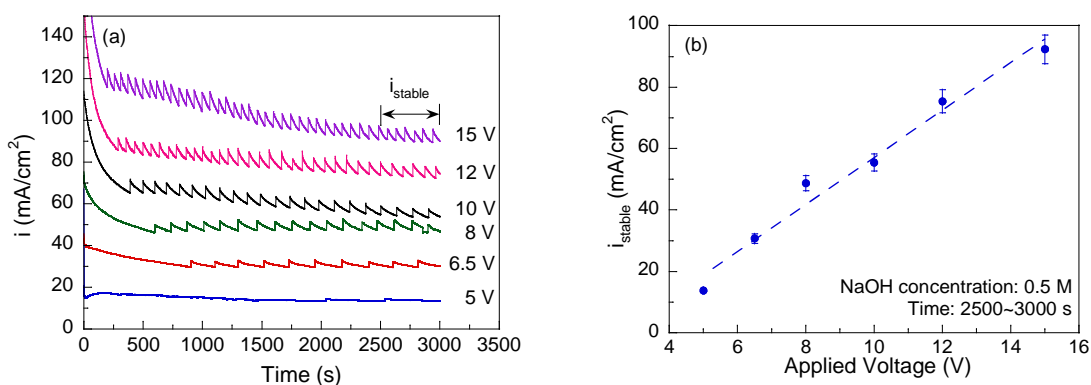


Figure 4. (a) Time evolution of anodic current during anodization of Sn; (b) dependence of i_{stable} on the applied voltage.

Figure 5(a) shows an enlarged view of the pattern of the current oscillation, as of the sample anodized at 15 V. In the figure some characteristic parameters are defined. Q_{initial} is the electric charge derived through the time integral of the current density before the onset of current oscillation, as defined in equation (1); t_0 and i_{initial} are the time and current density respectively at the moment when the oscillation first

occurred; Q_{rest} is the electric charge derived through the time integral of the current density during one oscillation period, as defined in equation (2); Δt is the duration of one current oscillation; Δi is the current jump at the beginning of one current oscillation.

$$Q_{\text{initial}} = \int_0^{t_0} i dt \quad (1)$$

$$Q_{\text{rest}} = \int_{t_1}^{t_2} i dt \quad (2)$$

Figure 5(b-d) shows the charge (Q_{rest}), current jump (Δi) and oscillation duration (Δt) of each of the oscillation peaks of the sample anodized at 15 V. It is seen that Q_{rest} remained practically constant during the process of anodization, ranging between 6×10^3 and 8×10^3 mC/cm². The value of Δi showed a slight decrease with time, and Δt showed a moderate increase with time. These are apparently related to the mild gradual decrease of the average current of the $i - t$ curve. The average current jump within the last section of the curve (between 2500 and 3000 s) is determined to be the characteristic stable stage average current jump of each sample. These observations are the same for all other samples anodized at other applied voltages. In the presentation below, the average values of Q_{rest} , Δi and Δt are used for each anodization voltage.

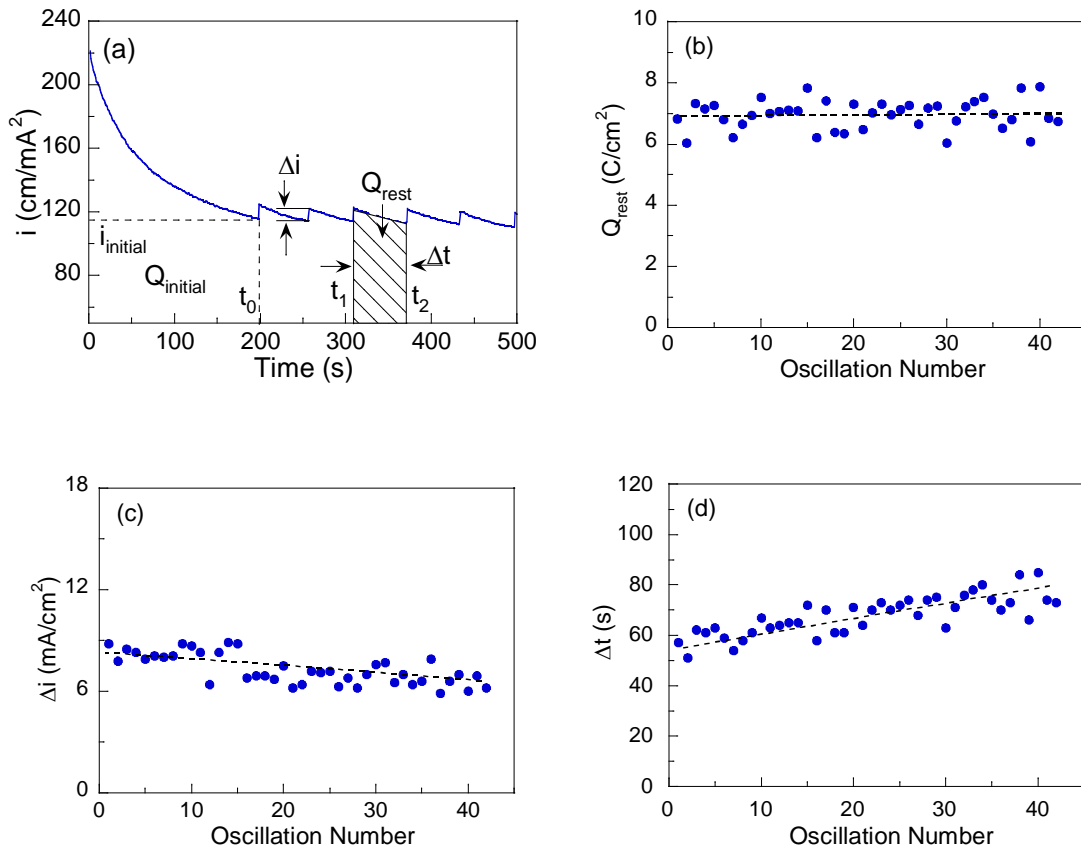


Figure 5. (a) Current oscillation of the sample anodized in 0.5 M NaOH electrolyte at 15 V and definitions of parameters; (b) charge of each oscillation period, (c) current jump of the oscillations and (d) duration of the oscillations.

Figure 6 shows the effect of applied voltages on Δi (graph (a)), $\Delta i/i_{\text{stable}}$ (graph (b)), $(\Delta t)^{-1}$ (graph (c)) and Q_{rest} (graph (d)). It is seen that Δi increased linearly with applied voltage, whereas $\Delta i/i_{\text{stable}}$ remained a constant at 8.7%, implying that Δi is only a function of i_{stable} . $(\Delta t)^{-1}$ also increased linearly with applied voltage. It is evident that Q_{rest} remained constant at $7 \times 10^3 \text{ mC/cm}^2$, irrespective of the applied voltage.

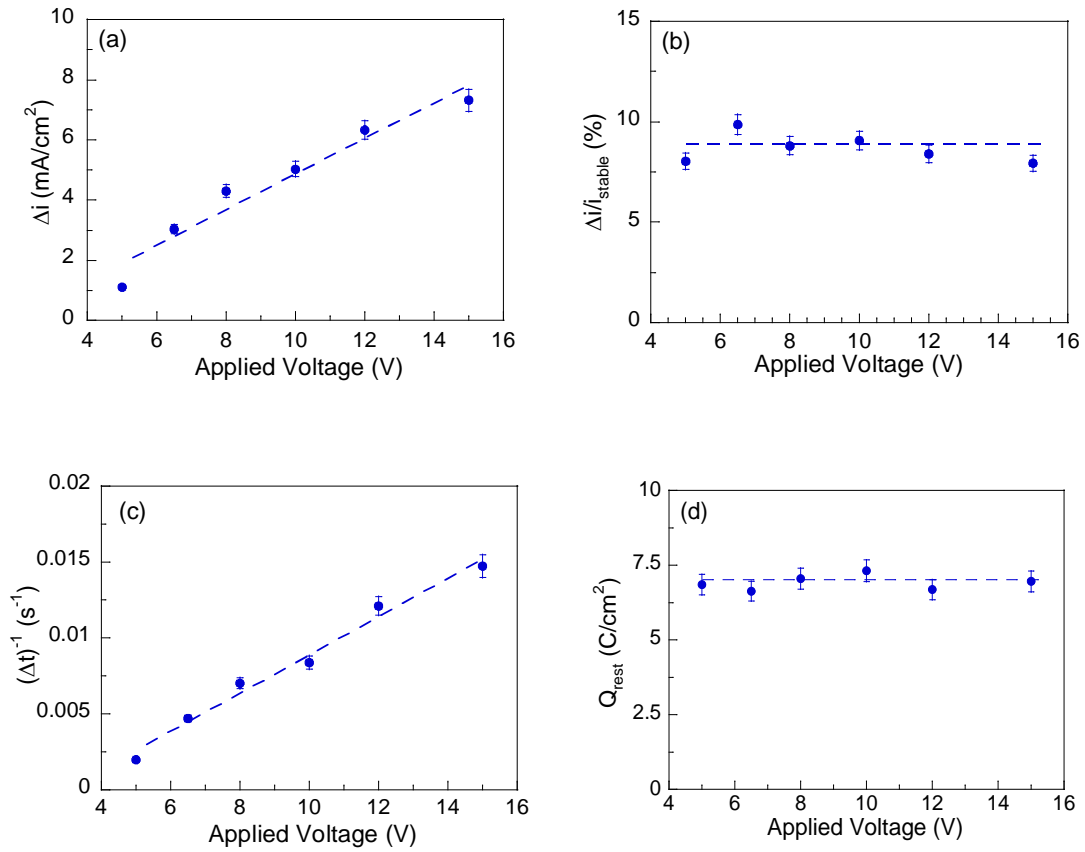


Figure 6. Effects of applied voltages on (a) Δi , (b) $\Delta i/i_{\text{stable}}$, (c) $(\Delta t)^{-1}$ and (d) Q_{rest} .

Figure 7 shows the effect of applied voltages on i_{initial} (graph (a)) and Q_{initial} (graph (b)). It is evident that whereas i_{initial} shows a linear dependence on the applied voltage, Q_{initial} is a constant at 3×10^4 mC/cm² at all voltages applied.

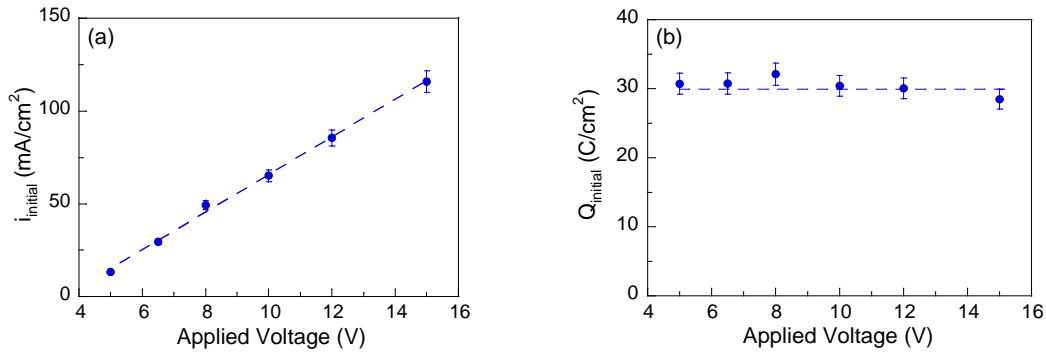


Figure 7. Effects of applied voltage on (a) i_{initial} , and (b) Q_{initial} .

3.4. Discussion

3.4.1. Anodic reactions and their kinetics

In this system there are two possible electrochemical anodic reactions, as expressed below:



Reaction (3) is the formation of SnO_2 and reaction (4) produces oxygen gas. The anodic potential of reaction (4) is higher than that of reaction (3). This implies that oxygen formation always occurs on the anode surface during the anodization process.

Figure 3(b) shows that the SnO_2 film thickness increases linearly with anodization time. This behavior implies that the oxide formation kinetics is not affected by the oxide already formed. This is not surprising considering the highly porous nature of the oxide film. It is also obvious that the products of reaction (4) will not affect the rate of the reaction. Therefore, it is clear that the total rate of anodic reactions is a time

constant for a given applied voltage in the stable stage, as evident in Figure 4(a), and that the linear increase of i_{stable} with applied voltage (shown in Figure 4(b)) is governed by mass transfer in the electrolyte. With this, the initial continuous decrease of the anodic current is attributed to the depletion of OH^- within the vicinity in front of the anode, due to lack of convection in the long channel.

3.4.2. Oxygen release and current oscillation

The oxygen generated was clearly visible at the anode. The oxygen generated is accumulated in the top part of the long channel in front of the anode, and small bubbles were periodically released when the pocket became too large. Figure 8 shows schematic illustrations of the oxygen bubble generation and escaping process. During the process of anodization, small oxygen bubbles form on the Sn surface (Figure 8a). The small bubbles accumulate at the upper ceiling of the channel wall, creating a gas pocket (Figure 8b). The O_2 pocket is held in position due to the space constraint. When the volume of the O_2 pocket reaches a critical level (V_1) (Figure 8b), the gas overcomes surface tension resistance and a gas bubble is released from the channel (Figure 8c). One important point is that only a small portion of the trapped gas in the pocket is allowed to escape (V_2), and the rest is re-arrested inside the channel by surface tension of the O_2 -electrolyte interface.

As the anodization proceeds, more oxygen is formed and added to the gas pocket, till the release of the next bubble. The correspondence between the release of each O_2 bubble and the sudden hike of the anodic current was confirmed by visual observation for all the samples. The release of one oxygen bubble introduces into the channel a volume of fresh solution equivalent to V_2 . This leads to the sudden jump of the anodic current because of the sudden increase of OH^- concentration in the electrolyte

in front of the anode.

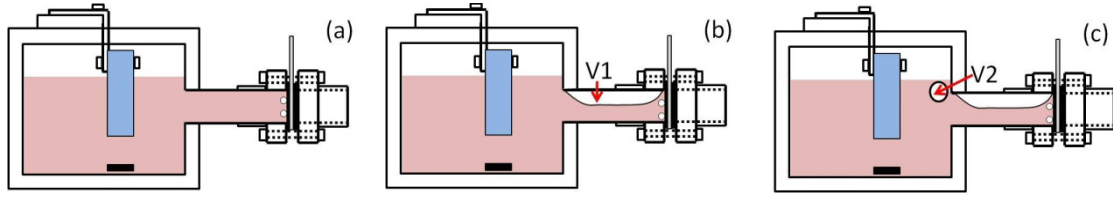


Figure 8. Schematic illustrations of oxygen generation and release from the channel: (a) initial formation of oxygen, (b) accumulation of oxygen to form the pocket (V1), and (c) release of one bubble of volume of V2.

3.4.3. Rates of oxygen generation and tin oxidation

To estimate the rates of oxygen production and tin oxidation, the total current is assumed to be only due to the charge exchange of the two anodic reactions, and charging currents are ignored. Moreover it is assumed that all oxygen molecules are transported to the bubble and the amount of dissolved oxygen in the electrolyte is comparatively negligible and constant. Under these conditions, the total anodic current is considered to be contributed to by both reactions (3) and (4), i.e.:

$$i = i_{\text{SnO}_2} + i_{\text{O}_2} \quad (5)$$

As established above, the two reactions do not interfere with each other and both rates are time constants. Therefore, it is reasonable to assume that:

$$i_{\text{SnO}_2} / i_{\text{O}_2} = k \quad (6)$$

As defined in equations (1) and (2):

$$Q_{\text{initial}} = \int_0^{t_0} i dt = \int_0^{t_0} (i_{\text{SnO}_2} + i_{\text{O}_2}) dt = (1 + k) \int_0^{t_0} i_{\text{O}_2} dt = (1 + k) Q_{\text{initial}, \text{O}_2} \quad (7)$$

$$Q_{\text{rest}} = (1+k) \int_{t_1}^{t_2} i_{\text{O}_2} dt = (1+k)Q_{\text{rest},\text{O}_2} \quad (8)$$

where $Q_{\text{initial},\text{O}_2} = \int_0^{t_0} i_{\text{O}_2} dt$ is the charge consumed for oxygen generation prior to the release of the first oxygen bubble and $Q_{\text{rest},\text{O}_2} = \int_{t_1}^{t_2} i_{\text{O}_2} dt$ is the charge consumed for oxygen generation during each period of current oscillation. It is easy to recognize that $Q_{\text{initial},\text{O}_2}$ corresponds to the volume of the gas pocket V1 and $Q_{\text{rest},\text{O}_2}$ corresponds to the volume of the gas bubble V1. Therefore:

$$\frac{Q_{\text{rest}}}{Q_{\text{initial}}} = \frac{(1+k)Q_{\text{rest},\text{O}_2}}{(1+k)Q_{\text{initial},\text{O}_2}} = \frac{Q_{\text{rest},\text{O}_2}}{Q_{\text{initial},\text{O}_2}} = \frac{V2}{V1} = 0.233 \quad (9)$$

As discussed in section 4.2, the current jump is attributed to the replenishment of the solution in the stagnant channel caused by the displacement of the oxygen bubble with fresh electrolyte solution. In this regard, the relative current jump $\Delta i/i_{\text{stable}}$, is expected to correspond to the relative replenishment of the electrolyte body in the channel, i.e.:

$$\frac{V2}{V_0 - V1} = \frac{\Delta i}{i_{\text{stable}}} = 0.087 \quad (10)$$

where V_0 is the channel volume (3.958 ml) and $(V_0 - V1)$ is the volume of the electrolyte held in the channel during the stable stage of anodization.

Solving equations (9) and (10) simultaneously gives that $V1=1.076$ ml and $V2 =0.251$ ml. Furthermore, it is derived the bubble size emitted from the channel is 3.91 mm of radius based on the $V2$ volume.

Volume $V2$ corresponds to 1.043×10^{-5} moles of oxygen gas, which in turn may translate into 3.558×10^3 mC/cm² electrical charge density on the anode for the

circular Sn anode of $\phi 12$ mm. This charge density is essentially $Q_{\text{rest},\text{O}_2}$. Therefore, the current density responsible for the oxygen generation may be estimated, using the average value of from Figure 6(b), as:

$$\frac{i_{\text{O}_2}}{i_{\text{stable}}} = \frac{Q_{\text{rest},\text{O}_2}}{Q_{\text{rest}}} \times 100\% = \frac{3.558}{7.018} \times 100\% = 50.7\% \quad (11)$$

The O_2 formation contributes 50.7% in the total anodic current. This value is schematically expressed in Figure 9 relative to the curve (I) for a sample anodized at 6.5 V in 0.5 M NaOH solution for 3000 s. Since both $\Delta i/i_{\text{stable}}$ (Figure 5(b)), Q_{rest} (Figure 6(d)) and Q_{initial} (Figure 7(b)) are constants irrespective of the applied voltage, V_2 is also independent of applied voltage. Given this, it is not difficult to see that this current division is true for anodization at all applied voltages for the current system.

3.4.4. Anodization without oxygen gas accumulation

To further prove the origin of the current oscillation observed, we conducted a comparative anodization experiment with the anode located in the main chamber of the electrochemical cell. Figure 9 shows schematic illustrations of two setups. Setup 1 has the “normal” configuration as all the experiments presented above, where current oscillation is observed (curve I in Figure 9(c)). Setup 2 is for the comparative experiment, where the Sn anode is placed in the open space in the cell. All other conditions (e.g., the anode size, the distance between the anode and cathode, the applied voltage, the electrolyte volume and concentration, the magnetic stirrer position and stirring speed) are identical for the two tests. It is evident in Figure 9(c) that the i - t curve of setup II is smooth and exhibits no current oscillation. This

behavior is similar to some observations reported in previous studies, e.g., for Fe [9] and Hf [30]. The Sn oxide formed in setup 2 has a random porous structure similar to that shown in figure 2. The higher anodic current for setup 2 relative to that of setup 1 is attributed to the open environment and the better convection of the electrolyte by magnetic stirring.

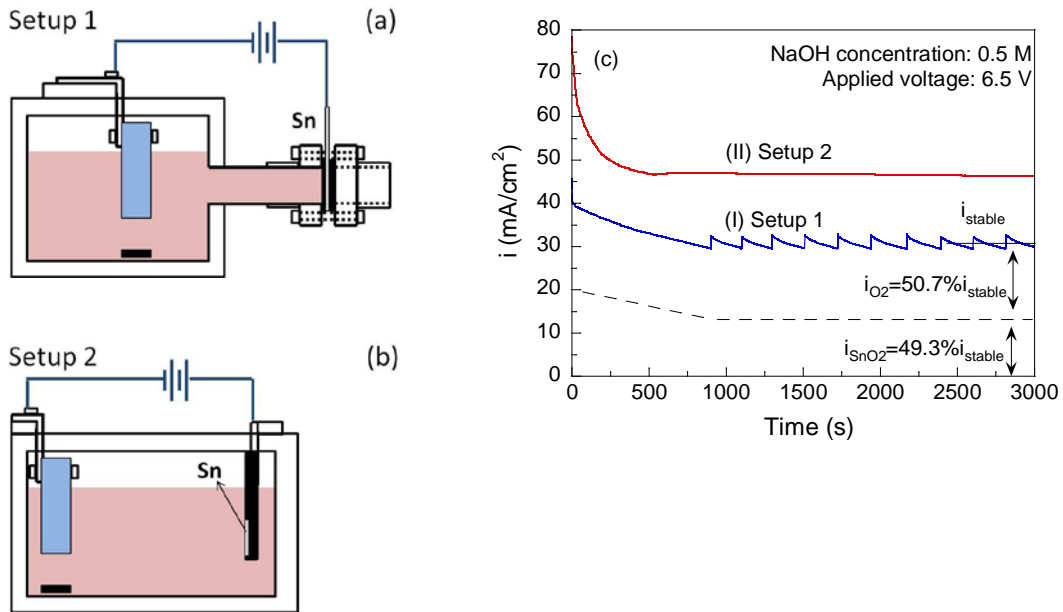


Figure 9. Schematic illustrations of comparative study using two different electrochemical cell configurations: (a) Setups 1, which allows oxygen accumulation; (b) Setup 2, which allows no oxygen buildup; (c) corresponding i - t curves of the two experiments.

3.5. Conclusions

This work for the first time revealed the direct correlation between periodic anodic current oscillation and O₂ gas generation and release. Based on the experimental evidences and the discussions presented, the following conclusions can be reached:

- 1) Anodization of tin in NaOH produces highly porous SnO₂. The total thickness of the nanoporous SnO₂ layer is found to increase linearly with time, indicating that

the anodic products have no influence on the electrochemical activities at the anode.

- 2) Highly repeatable periodic current oscillation is observed during anodization of tin in NaOH solution at all different applied voltage levels between 5 and 15 V. The total electrical charge consumed prior to the onset of the oscillation Q_{initial} , the relative current amplitude of the oscillations $\Delta i / i_{\text{stable}}$, and the electrical charge of each oscillation period Q_{rest} are all constants irrespective of the anodization voltage applied.
- 3) The current oscillation cycles are found to coincide precisely with the periodic release of oxygen bubbles from a gas pocket trapped in the electrochemical cell. The periodic release of O_2 causes convection in the electrochemical cell, rejuvenating the anodic process, causing the sudden jump of the anodic current.
- 4) There exist two anodic reactions in this process: anodic oxidation of Sn in NaOH electrolyte and O_2 formation. The first reaction is determined to contribute 49.3% and the second reaction 50.7% of the total anodic current.

Acknowledgements

M. Wang wishes to acknowledge the scholarship support from the Chinese Scholarship Council and the University of Western Australia. We also acknowledge the experimental support of the Centre for Microscopy, Characterization and Microanalysis of the University of Western Australia for electron microscopy and microstructure analysis.

References

- [1] H. Masuda, K. Fukuda, *Science* 268 (1995) 1466-1468.
- [2] D. Gong, C. A. Grimes, O. K. Varghese, W. Hu, R. S. Singh, Z. Chen, E. C. Dickey, *Journal of Materials Research* 16 (2001) 3331-3334.
- [3] R. Beranek, H. Hildebrand, P. Schmuki, *Electrochemical and Solid-State Letters* 6 (2003) 12-14.
- [4] J. Choi, J. H. Li, S. C. Lee, J. H. Chang, K. J. Kim, M. A. Cho, *Electrochimica Acta* 51 (2006) 5502-5507.
- [5] I. Sieber, B. Kannan, P. Schmuki, *Electrochemical and Solid-State Letters* 8 (2005) 10-12.
- [6] X. Feng, T. J. LaTempa, J. I. Basham, G. K. Mor, O. K. Varghese, C. A. Grimes, *Nano Letter* 10 (2010) 948-952.
- [7] H. Zheng, A. Z. Sadek, K. Latham, K. Kalantar-Zadeh, *Electrochemistry Communications* 11 (2009) 768-771.
- [8] H. Tsuchiya, P. Schmuki, *Electrochemistry Communications* 6 (2004) 1131-1134.
- [9] T. J. LaTempa, X. Feng, M. Paulose, C. A. Grimes, *Journal of Physical Chemistry C* 113 (2009) 16293-16298.
- [10] J. C. Vial, A. Bsiesy, F. Gaspard, R. Hérino, M. Ligeon, F. Muller, R. Romestain, R. M. Macfarlane, *Physical Review B* 45 (1992) 14171-14176.
- [11] K. Kim, J. Choi, T. S. Bae, *Applied Physics Letters* 90 (2007) 181912.
- [12] Y. C. Shen, I. C. Leu, W. H. Lai, M. T. Wu, M. H. Hon, *Journal of Alloys and Compounds* 454 (2008) L3-L9.
- [13] M. Yang, N. K. Shrestha, P. Schmuki, *Electrochimica Acta* 55 (2010) 7766-7771.
- [14] I. Paramasivam, J. M. Macak, P. Schmuki, *Electrochemistry Communications* 10 (2008) 71-75.
- [15] F. Schmidt-Stein, R. Hahn, J.-F. Gnichwitz, Y. Song, N. K. Shrestha, A. Hirsch, P. Schmuki, *Electrochemistry Communications* 11 (2009) 2077-2080.
- [16] E. Balaur, J. M. Macak, L. Taveira, P. Schmuki, *Electrochemistry Communications* 7 (2005) 1066-1070.

- [17] E. Balaur, J. M. Macak, H. Tsuchiya, P. Schmuki, *Journal of Materials Chemistry* 15 (2005) 4488-4491.
- [18] K. Shankar, James I. Basham, N. K. Allam, O. K. Varghese, G. K. Mor, X. Feng, M. Paulose, J. A. Seabold, K.-S. Choi, C. A. Grimes, *Journal of Physical Chemistry C* 113 (2009) 6327-6359.
- [19] G. K. Mor, K. Shankar, M. Paulose, O. K. Varghese, C. A. Grimes, *Applied Physics Letters* 91 (2007) 152111.
- [20] J. R. Jennings, A. Ghicov, L. M. Peter, P. Schmuki, A. B. Walker, *Journal of the American Chemical Society* 130 (2008) 13364-13372.
- [21] H. Föll, M. Leisner, A. Cojocar, J. Carstensen, *Materials* 3 (2010) 3006-3076.
- [22] J. Carstensen, R. Prange, H. Föll, *Journal of The Electrochemical Society* 146 (1999) 1134-1140.
- [23] J. Grzanna, H. Jungblut, H. J. Lewerenz, *Journal of Electroanalytical Chemistry* 486 (2000) 181-189.
- [24] J. Grzanna, H. Jungblut, H. J. Lewerenz, *Journal of Electroanalytical Chemistry* 486 (2000) 190-203.
- [25] V. Parkhutik, E. Matveeva, R. Perez, J. Alamo, D. Beltran, *Materials Science and Engineering B* 69-70 (2000) 553-558.
- [26] L. V. Taveira, J. M. Macak, K. Sirotna, L. F. P. Dick, P. Schmuki, *Journal of The Electrochemical Society* 153 (2006) 137-143
- [27] W. Lee, J.-C. Kim, U. Gosele, *Advanced Functional Materials* 20 (2010) 21-27.
- [28] K. Schwirn, W. Lee, R. Hillebrand, M. Steinhart, K. Nielsch, U. Gösele, *ACS Nano* 2 (2008) 302-310.
- [29] C. Y. Han, G. A. Willing, Z. Xiao, H. H. Wang, *Langmuir* 23 (2007) 1564-1568.
- [30] H. Tsuchiya, P. Schmuki, *Electrochemistry Communications* 7 (2005) 49-52.

CHAPTER 4. Anodization Process of Sn in Oxalic Acid at Low Applied Voltages

Mingliang Wang, Yinong Liu, Dongke Zhang and Hong Yang,

Electrochimica Acta, 59 (2012) 441-448.

Abstract

This study investigated the anodization of tin in oxalic acid electrolyte at low applied voltages of $U \leq 5$ V. Under such conditions, the anodization product consists of micron-sized SnC_2O_4 crystalline particles and the morphology of the product changes during the anodization process in three distinctive stages. In the initial stage I, Sn dissolves into the electrolyte at high current density. This process is associated with the precipitation of highly oriented SnC_2O_4 crystals on the Sn surface. Stage II is a passivation process associated with the formation of a SnC_2O_4 surface layer with unique pyramidal microstructure via in-situ conversion. Stage III is the localized creation of smaller SnC_2O_4 polyhedron crystals. The anodic reaction mechanisms for each stage are discussed in detail and a mathematical model is established to quantify the critical condition that induces the anodic passivation.

Keywords: tin; anodization; electrochemical dissolution; SnC_2O_4

4.1. Introduction

The electrochemical anodization of various metals (e.g., Al [1, 2], Ti [3, 4], Nb [5], Ta [6-9], W [10], Zr [11] and Fe [12]) and semiconductors (e.g., Si [13], GaN [14], GaP [15] and CdS [16]) under appropriate conditions is able to generate varieties of nanostructures. In the last decade, these new breeds of nanomaterials have received intensive interests due to their high technological potentials in many applications, e.g., photocatalysts for organic degradation [17, 18], self-cleaning substrates [19, 20], solar cell electrodes [21-23] and luminescence devices [13, 24].

Tin dioxide (SnO_2) is an n-type semiconductor widely utilized in solid-state gas sensors [25, 26] and oxidation catalysts [27]. It also has the potential to function as high capacity anode materials for lithium-ion batteries [28, 29]. These applications desire a large specific surface area [30]. Anodization of Sn is a promising method to synthesize porous tin oxide structure with large specific surface areas. Both acidic [31-33] and alkaline [34] electrolytes can be used to create such structures. Jeun et al. [32] synthesized anodized irregular nanoporous tin oxide film in 0.3 M oxalic acid solution at 6 V, and used it as gas sensor materials. They found that the nanoporous tin oxide films have the shortest response time and highest gas response in CO detection, comparing to sensors based on compact SnO_2 film and a commercial SnO_2 powder ($\sim 45 \mu\text{m}$). The better sensing effect was attributed to the higher specific surface area of the porous tin oxide film.

It is known that anodization of Sn in oxalic acid solutions at above 5 V of applied voltages produces highly porous tin oxide structures [33]. In this study we investigated the anodization behavior of Sn in oxalic acid solution under relatively low applied voltages of ≤ 5 V, and produced totally different products. The anodic chemical processes, the development of the anodized surface morphology and the possible formation mechanisms are discussed in this paper. Furthermore, a mathematical model is developed to quantify the critical condition which causes the

anodic passivation.

4.2. Experimental procedures

Sn foil of 99.99 at% purity and 400 μm thickness was used in the anodization experiment. The foil coupons were ultrasonically cleaned in ethanol and deionized water prior to anodization. The electrolyte used was an oxalic acid aqueous solution of 0.27 M concentration. The anodization experiments were performed at ambient temperatures in a two-electrode cell using a high purity titanium plate as the cathode. A constant voltage was applied for each experiment, ranging from 0.5 to 5.0 V. The i - t curves of the anodization process were recorded via a computer with a USB-interfaced digital multimeter (DMM 86C).

After the anodizing treatment, the Sn foil anode was removed from the electrolyte, rinsed several times in deionized water, and dried in air at ambient. The X-ray powder diffraction (XRD) pattern of the anodized foil was obtained using a Siemens D5000 Diffractometer with Cu K_{α} radiation ($\lambda = 0.1542$ nm) at 40 kV and 35 mA. The morphology of the anodized products was characterized using a Zeiss 1555 field emission scanning electron microscope (FESEM). The compositions of anodized products were determined by energy dispersive X-ray spectrometry (EDS) equipped with the FESEM. In the EDS analysis, carbon was subtracted as the background, and normalized Sn (at%) and O (at%) contents were derived.

4.3. Results

The anodization of Sn metal in oxalic acid solution at 3 V for 6000 s results in the formation of an off-white powder loosely spread on the Sn electrode surface, as clearly seen in the macroscopic insert in Figure 1. The SEM micrograph of the

anodized Sn surface reveals that the product consists of micron sized particles of ~ 1 μm , as shown in Figure 1.

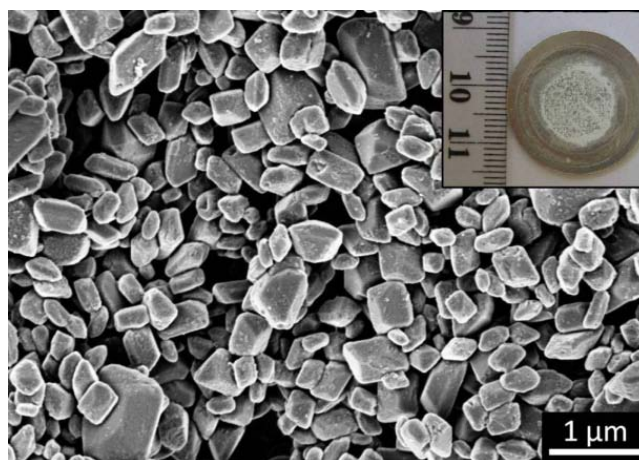


Figure 1. SEM micrograph of the product on the surface of Sn anode after anodization in oxalic acid solution at 3 V for 6000 s. The insert macroscopic image is the anodized Sn surface.

Figure 2 shows XRD spectra of the Sn surface anodized at 3 V for different time periods. The spectra can all be indexed to SnC_2O_4 (JCPDS: 51-0614) during the whole anodization process. The Sn peaks observed in XRD spectra are from the background of the Sn foil (JCPDS: 89-4898). It is evident that anodization of Sn in oxalic acid electrolytes at low applied voltages of 3 V produce SnC_2O_4 particles.

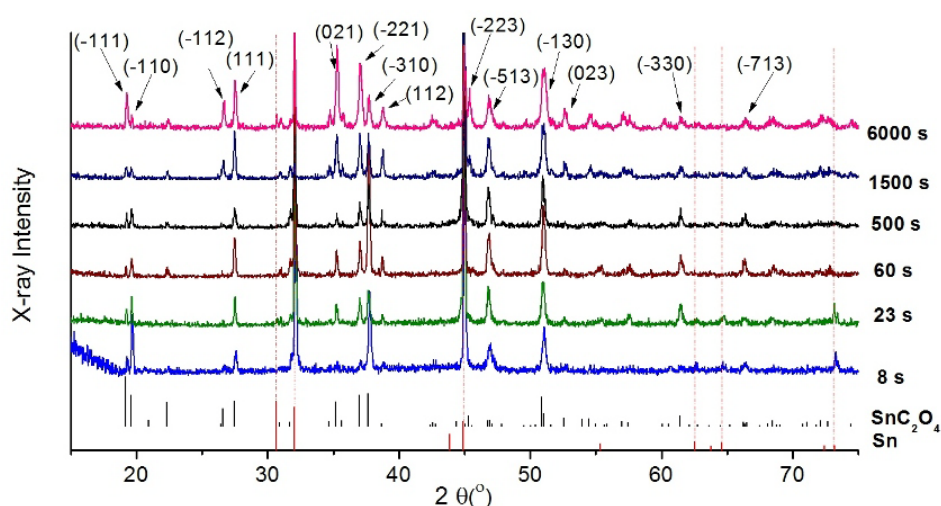


Figure 2. XRD spectra of the Sn surface anodized at 3 V for different time periods.

Considering the electrochemical/chemical reactions in this anodization system, two processes for the formation of SnC₂O₄ are possible:

(1) Dissolution and Precipitation process

On the Sn anode surface, Sn atoms are ionized via reaction (1a). Each Sn²⁺ ion is chelated with two C₂O₄²⁻ ions to form a [Sn(C₂O₄)₂]²⁻ complex ion following reaction (1b). The formation of [Sn(C₂O₄)₂]²⁻ ions and the precipitation of SnC₂O₄ following reaction (1c) ensure the establishment of an equilibrium concentration of [Sn(C₂O₄)₂]²⁻ ions at near the Sn anode.



(2) Direct formation process

An alternative chemical process may also be possible. In this case, on the Sn anode surface, each ionized Sn²⁺ ion is combined with a C₂O₄²⁻ ion to directly form an insoluble SnC₂O₄ following the reaction (2b).



Note that the reaction (1b) is a thermodynamically favored process than reaction (2b), since the chemical equilibrium constant for the formation of [Sn(C₂O₄)₂]²⁻ ion is about 3 orders higher than that of SnC₂O₄. The equilibrium constant, k_{1(c)} shown with reaction 1(c) is calculated since $k_{1(c)} \cdot k_{\text{SnC}_2\text{O}_4} = k_{[\text{Sn}(\text{C}_2\text{O}_4)_2]^{2-}}$.

Figure 3(a) shows a typical *i-t* curve of Sn anodized at 3 V in the oxalic acid solution for 6000 s. Figure 3(b) is the initial 100 s of the *i-t* profile from figure 3(a). The *i-t* curve clearly displays three distinctive stages during the anodization of Sn. In stage I

the current density is maintained at a high value for the initial 21 s. In stage II the current density decreases rapidly by 95%, from ~ 22 to ~ 1 mA/cm². In stage III the current density remains at a low and steady level for the rest of the anodization process.

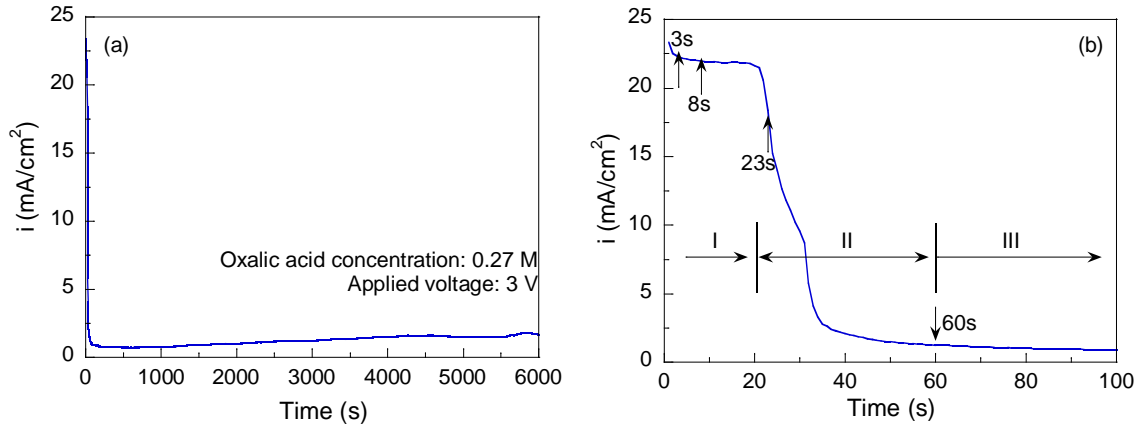


Figure 3. A typical i - t curve of the sample anodized at 3 V in 0.27 M oxalic acid solution for (a) 6000 s and (b) the beginning 100 s with stage divisions.

To investigate the anodic chemical processes and the evolution of the anodized structure (In this case, the formation of particulate SnC₂O₄) in relation to the distinctive i - t stages, detailed XRD analysis and microscopy study of anodized anode surface were conducted at four anodization time points of 3 s, 8 s, 23 s and 60 s, as labeled on the i - t curve shown in Figure 3(b). Furthermore, analysis was also carried out at longer anodization time periods up to 6000 s. The experimental evidences reveal the following correlations between anodic structure and the i - t characteristics.

(1) *Stage I: Anodic dissolution of Sn at higher current density and heterogeneous nucleation and growth of SnC₂O₄ crystals*

Figure 4 shows SEM micrographs of Sn anode surface after anodization for (a) 3 s, (b) 8 s, (c) 23 s and (d) 60 s. As seen in Figure 3(b), the initial current density is high and maintained at ~ 22 mA/cm² for 21 s. This current density is sustained by the

dissolution of Sn anode (1a) and subsequent formation of $[\text{Sn}(\text{C}_2\text{O}_4)_2]^{2-}$ ions (1b). The formation of SnC_2O_4 crystals also occurs via (1c) at this stage, as evident in the SEM micrograph of the Sn anode after anodization for 3 s (Figure 4(a)). The SnC_2O_4 particles form and scatters on the surface of Sn anode. The particles are roughly in rectangular shape with average particle size of 10 μm . These SnC_2O_4 crystals appear to be aligned along certain directions, apparently governed by the orientation of the Sn grains underneath. These observations suggest that at this stage, the formation of anodized SnC_2O_4 particles is via a heterogeneous nucleation and growth process; these SnC_2O_4 particles are referred to as stage-I particles. The nucleation and growth of stage-I particles continues on the Sn anode surface as clearly evidenced in Figure 4(b) (anodization for 8 s) and 4(c) (anodization for 23 s), the particles reach the size of 20-30 μm at the completion of the stage I. No significant change is observed for stage-I particles at anodization of 60 s, well into stage II.

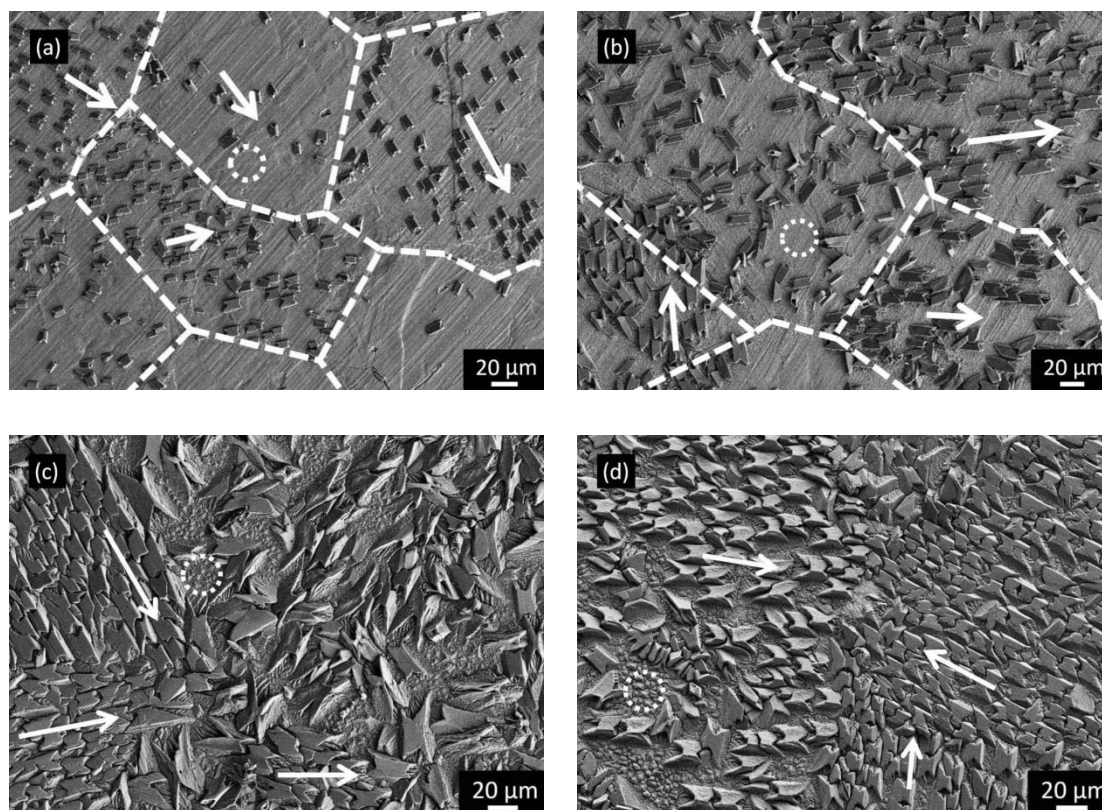


Figure 4. SEM micrographs of for the surface of the Sn anode after anodization in 0.27 M oxalic acid electrolyte for: (a) 3 s, (b) 8 s, (c) 23 s and (d) 60 s.

In addition, the original surface of the Sn anode beneath the stage-I particles are also examined closely. Figure 5((a)-(d)) shows high magnification SEM micrographs of the circled areas marked in Figure 4((a)-(d)), respectively. The Sn and O contents are determined by the EDS analysis. It is seen in Figure 5(a) that the original polishing scratches on the Sn anode surface are still visible after 3 s of anodization. At 8 s, however, these scratches are no longer visible and the surface has appeared wavy with a large population of pits (Figure 5(b)). The disappearance of the original scratches and the appearance of pits are evidences of anodic dissolution of Sn via reaction (1a). In the left-lower hand corner of each micrograph shows the Sn and O contents of the surface as determined by the EDS analysis. It is seen that very low amount of oxygen is detected on the Sn surface, thus excluding the possibility of continuous deposition of SnC₂O₄ layer on the Sn anode surface.

(2) Stage II: Passivation of Sn surface caused by direct formation and in-situ growth of SnC₂O₄ particle layer

Stage II is marked by a rapid decrease of anodic current, thus apparently a passivation process of Sn anode. The focus is thus to closely examine the surface of Sn anode underneath of the stage-I particles.

Figure 5(c) shows the sample after anodization for 23 s, corresponding to the beginning of Stage II. The surface of the Sn anode is found to be covered by a closely arranged SnC₂O₄ particle layer with a distinctive capped pyramid-like morphology. The oxygen content of the surface is obviously increased, to 19 at%. Figure 5(d) shows the sample after anodization for 60 s. It is seen that the particle layer progressively grow thicker further into stage II, but the capped pyramid-like morphology remains with each pyramid being about 5 μm in dimension and bounded by well-defined crevices. EDS analysis shows a high oxygen content of 78 at%, giving a O(at%)/Sn(at%) ratio of approximately 4:1, the stoichiometry of SnC₂O₄.

This is consistent with the XRD analysis shown in Figure 2. The development of this stage-II SnC_2O_4 particle layer occurs via an in-situ formation of SnC_2O_4 through reaction (2b) on the Sn surface. This particle layer is responsible for the passivation behavior manifested in the i - t curve (Figure 3(b)).

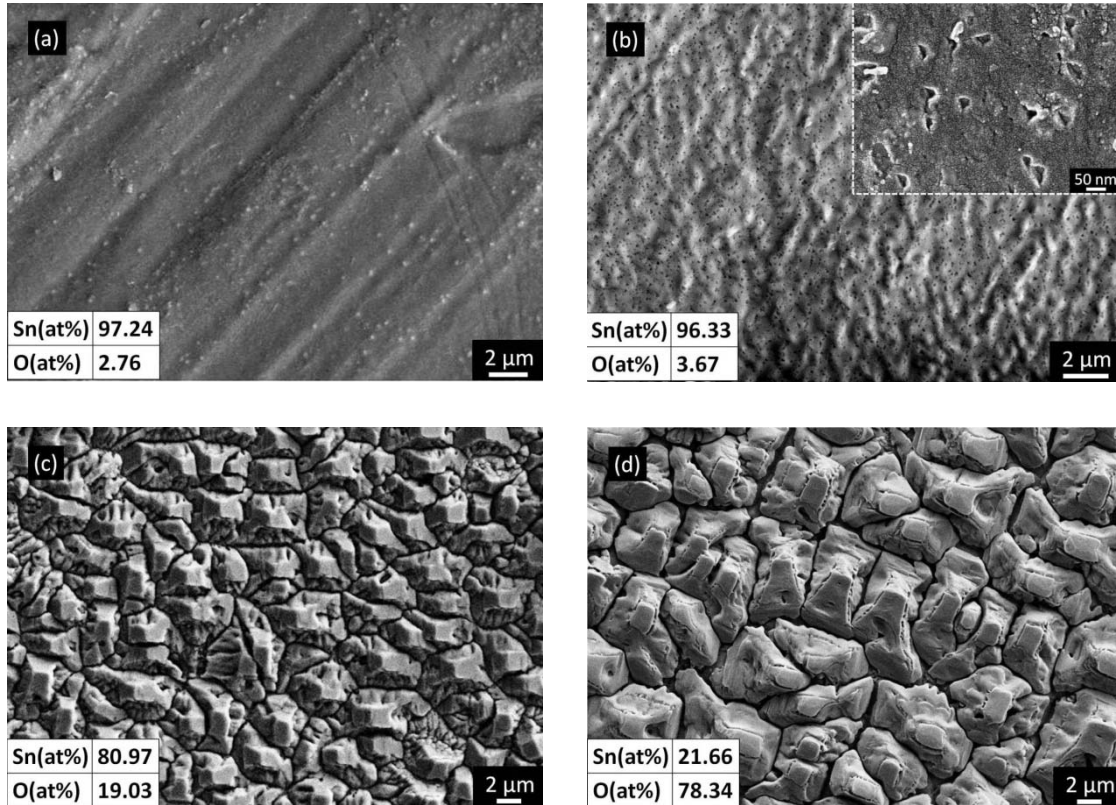


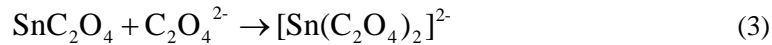
Figure 5. SEM micrographs (Combining with Sn (at%) and O (at%) content by EDS analysis) of enlarged circle area labeled in figure 4 for the Sn anodized in 0.27 M oxalic acid for: (a) 3 s, (b) 8 s, (c) 23 s and (d) 60 s respectively.

(3) Stage III: Anodic dissolution at lower current density and localized nucleation and growth of SnC_2O_4

Figure 6 shows SEM micrographs of the Sn anode anodized in 0.27 M oxalic acid for (a) 300 s, (b) 500 s, (c) 1000 s, (d) 1500 s, (e) 3000 s and (f) 6000 s. Two phenomena are observed during the progression of this stage.

Figure 6(a) shows a sample anodized for 300 s. The stage-I particles appear to remain intact on the Sn anode surface as at the end of stage II. The inset shows a close-up

view of one particle at a higher magnification. It is evident that chemical attack has occurred to the stage-I particles, which have lost their smooth facets and became ragged, even partially shattered. Considering the possible chemical processes in this anodic system, it is clear that the stage-I particles are subjected to chemical dissolution reaction (3), resulting in localized dissolution of SnC_2O_4 along specific crystallographic orientations. The reaction (3) is the reverse process of reaction (1c).



This chemical dissolution of stage-I particles progresses through stage III. The size of the stage-I particles decreases continuously from $\sim 20 \mu\text{m}$ for the sample anodized for 300 s to $\sim 10 \mu\text{m}$ after 3000 s of anodization. More pronouncedly is the change in the shape and surface features of the stage-I particles. Progressive chemical dissolution selectively leaches away certain facets, creating polyhedron particles of perfectly smooth facets about half of their initial sizes.

The dominant event occurred during stage III is the formation of a new population of polyhedron particles of smaller sizes. This becomes evident after anodization for 500 s, as shown in Figure 6(b). Masses of small SnC_2O_4 particles ($\sim 1 \mu\text{m}$) emerges from beneath the stage-I particles, as indicated by the dashed circles. These particles are termed stage-III particles. Large numbers of such small SnC_2O_4 particles are continuously formed during anodization in stage III (6(c) and (d)), and eventually submerge the shrinking stage-I larger particles (6(e)). The stage-III particles are formed via a localized direct formation process by reaction (2b).

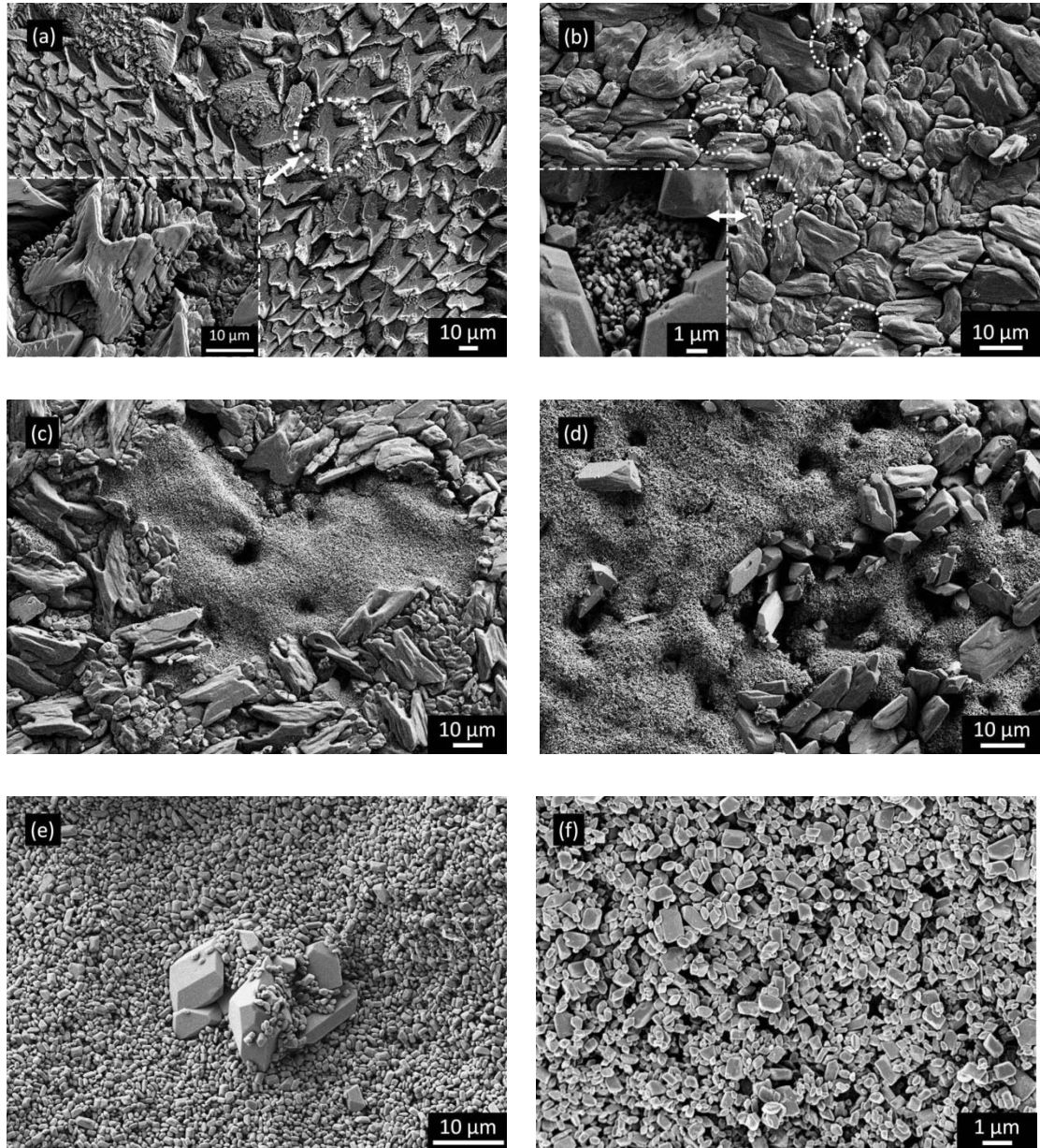


Figure 6. The typical top view SEM micrographs of Sn anodized in 0.27 M oxalic acid for: (a) 300 s, (b) 500 s, and (c) 1000 s, (d) 1500 s, (e) 3000 s and (f) 6000 s. The insert images in (a) and (b) show the enlarged view of the circle areas.

Figure 7 shows schematic drawings of the reaction mechanisms during Sn anodization based on the above information. The transition from stage I to stage II corresponds to the change of chemical process from reactions (1b)-(1c) to reaction (2b). At the beginning of stage I, as depicted in Figure 7(a), the anodic dissolution of Sn to form $[\text{Sn}(\text{C}_2\text{O}_4)_2]^{2-}$ ions following the reaction (1a) and (1b) dominates the anodization

process. The $[\text{Sn}(\text{C}_2\text{O}_4)_2]^{2-}$ ions formed are accumulated in the double layer in front of the anode surface under the influence of the applied electrical field (E-field). During this stage, stage-I particles form via reaction (1c) as an accompanying process, as depicted in Figure 7(b). As the anodization process continues (Figure 7(b)), the concentration of $[\text{Sn}(\text{C}_2\text{O}_4)_2]^{2-}$ at near the anode surface continues to increase until it reaches the equilibrium value dictated by reaction (1c). The progression of anodization from this point onwards transits to direct formation of SnC_2O_4 following reaction (2b). This marks the transition into stage II. The direct formation of SnC_2O_4 results in the creation of a passivation layer on the surface of the Sn anode, as depicted in Figure 7(c). The continued growth of the stage-II SnC_2O_4 particle layer eventually isolates the electrolyte from the Sn anode at the end of stage II (Figure 7(d)).

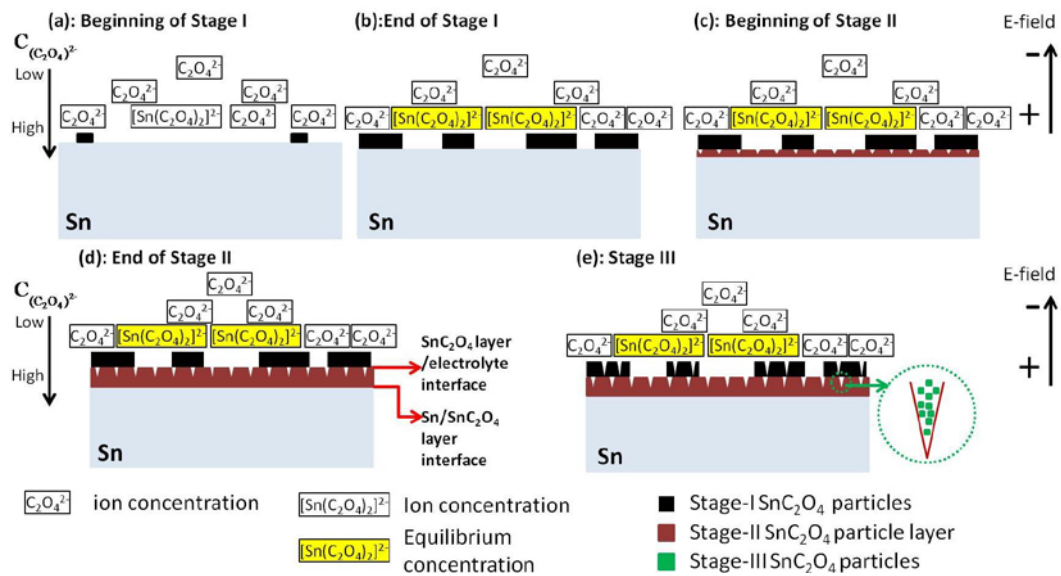


Figure 7. Schematic drawing of the reaction mechanisms during the Sn anodization process.

Entering into stage III, the continued anodic dissolution of Sn and formation of SnC_2O_4 requires Sn^{2+} to diffuse outwards through the passive layer to react with $\text{C}_2\text{O}_4^{2-}$ at the SnC_2O_4 layer/electrolyte interface. Naturally, Sn^{2+} ions would diffuse through the crevices bound the pyramidal islands on the passivation layer (figure 5(d) & 7(d)), as they provide the shortest diffusion path for Sn^{2+} ions across the passivation

layer. This leads to the localized formation of the new breed of SnC₂O₄ particles, i.e. the stage-III particles, in the crevices as shown in figures 6(b) and 7(e).

The above analysis is supported by the anodization charge measurement. Figure 8(a) shows *i-t* curves of a few samples anodized at various applied voltages up to 5 V. Figure 8(b) shows the dependence of the stable stage current density (*i*_{stable}) on the applied voltages (U). The *i*_{stable} is defined as the average current density in the stage III determined in the range from 2500 s to 3000 s. The *i*_{stable}-U relationship is exponential, as illustrated in figure 8(b). This exponential relationship indicates that stage III is an ionic diffusion controlled process [37-39], i.e., controlled by the diffusion of Sn²⁺ through the SnC₂O₄ particle layer.

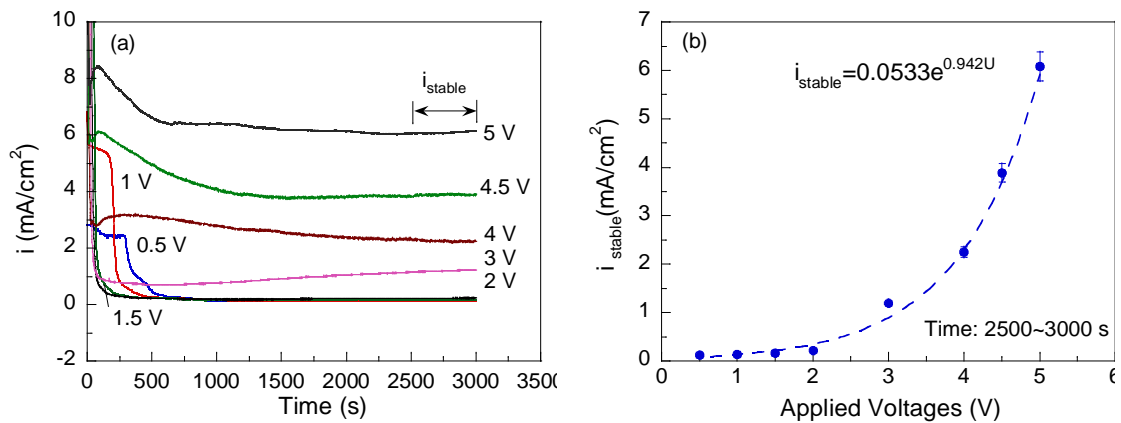


Figure 8. (a) Current density (*i*) transients on anodizing time (0 ~ 3000 s) recorded for Sn anodization at 0.27 M oxalic acid for various applied voltages ($U \leq 5$ V); (b) Dependence of *i*_{stable} on the applied voltage.

4.4. Discussion

The anodic *i-t* curve of Sn obtained in oxalic acid electrolytes under relative low applied voltages clearly shows three stages involving a passivation process as illustrated in Figure 3(b). Under such low voltage conditions, anodization of Sn results in the formation of SnC₂O₄ particles, rather than SnO₂ nanoporous structures. Our detailed study seems to suggest that the stage I proceeds via a dissolution and

precipitation mechanism following reactions (1a) to (1c), whilst the stage II and III occur by direct formation mechanism via reaction (2a) and (2b). The following discussion highlights the quantification of the critical conditions for this stage I to stage II transition.

4.4.1. Electrochemical Anodic reactions

In this system there are two possible electrochemical anodic reactions as expressed below:



Reaction (4a) is the dissolution of Sn atoms and reaction (4b) produces oxygen gas. The anodic potential of reaction (4a) is significantly lower than that of (4b). Consequently, Sn anodic dissolution will occur on the anode prior to the emission of oxygen during the anodization process. This is also confirmed on the observation of anodization process at low applied voltages, where the oxygen formation occurred only to a very minor extent.

4.4.2. The critical conditions for the stage I to stage II transition

It is considered that the transition from the stage I to stage II corresponds to two different chemical processes as expressed by reactions (1b) & (1c) and (2b), respectively. Once the concentration of $[\text{Sn}(\text{C}_2\text{O}_4)_2]^{2-}$ ions in the electric double layer reaches the equilibrium value, the transition from the stage I to stage II occurs.

The following analysis further supports the proposed transitional mechanism. During stage I, the concentration of the accumulated $[\text{Sn}(\text{C}_2\text{O}_4)_2]^{2-}$ ions can be related to the observed current density i_{II} by equation (5):

$$\int_0^{t_1} \left(\frac{A}{z \cdot 10^3 \cdot F} i_{II} - R_{(1c)} \right) \cdot dt = V_{dl} C_e \quad (5)$$

where

i_{II} (mA/cm²): the average current density at stage I.

t_1 (s): the anodized duration of stage I.

A (cm²): the surface area of Sn anode, 1.13 cm².

z : the electron transfer number ($z=2$).

F (C/mol): the Faraday constant, 96500 C/mol.

$R_{(1c)}$ (mol/s): the average precipitation rate of SnC₂O₄ via reaction (1c) during stage I.

C_e (mol/L): the equilibrium concentration of [Sn(C₂O₄)₂]²⁻ dictated by reaction (1c).

V_{dl} (L): the volume of the electric double layer established on the Sn anode surface.

Since i_{II} is the plateau current density of stage I, it is treated as a constant. The equation (5) can thus be integrated to give the following:

$$\left(\frac{A}{2 \cdot 10^3 \cdot F} i_{II} - R_{(1c)} \right) \cdot t_1 = V_{dl} C_e \quad (6)$$

Figure 9(a) shows the dependence of average current density (i_{II}) of the stage I anodization on applied voltages. It is seen that i_{II} increases linearly with the applied voltages following the relation:

$$i_{II} = 8.66U - 2.32 \quad (7)$$

This relation indicates that the anodic dissolution in stage I is governed by migration of (C₂O₄)²⁻ ions in the electrolyte.

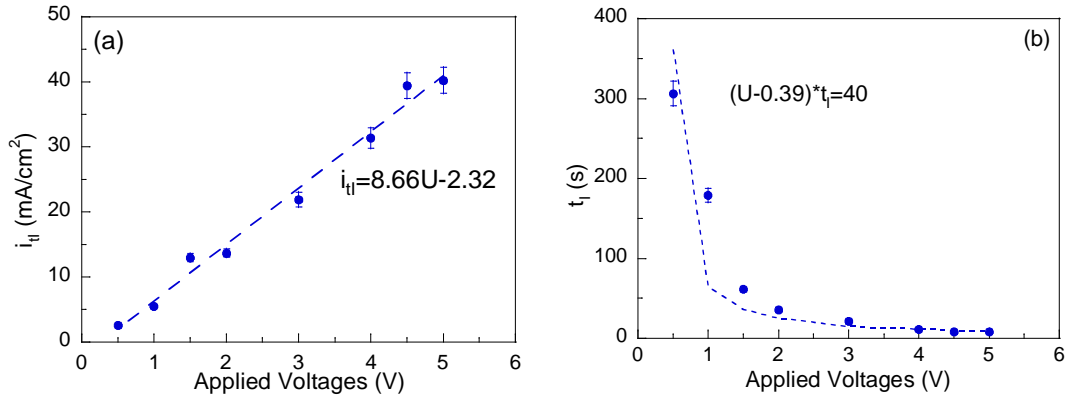


Figure 9. Dependence of (a) average current density (i_{tI}) and (b) anodized duration (t_I) of the stage I anodization on applied voltages.

Substituting equation (7) and all other known constants into (6) gives rise to

$$(U - 0.27 - \frac{R_{(1c)}}{5.07 \times 10^{-8}}) \cdot t_I = \frac{V_{dl} C_e}{5.07 \times 10^{-8}} \quad (8)$$

Figure 9(b) shows anodized duration (t_I) of the stage I anodization on applied voltages. From figure 9(b), an optimum fitting curve is derived using the Matlab software which gives

$$(U - 0.39) \cdot t_I = 40 \quad (9)$$

Comparing the left side of equations (8) and (9), it is derived:

$$0.27 + \frac{R_{(1c)}}{5.07 \times 10^{-8}} = 0.39 \quad (10)$$

Therefore, the average precipitation rate of stage-I SnC₂O₄ is obtained as $R(1c) = 0.61 \times 10^{-8}$ mol/s.

At the applied voltage of $U = 3$ V, as an example, the anodization at stage I lasted for $t_I = 21$ s. The electric charge consumed during the stage I can be integrated (Figure 3(b)) as:

$$Q_{tI} = A \int_0^{21} i_{tI} dt = 0.497C \quad (11)$$

If all the electric charge is consumed by anodic dissolution of $\text{Sn} \rightarrow \text{Sn}^{2+}$ ions via reaction (1a) and, subsequently all the Sn^{2+} ions are then converted to $[\text{Sn}(\text{C}_2\text{O}_4)_2]^{2-}$ ions via reaction (1b), the amount of $[\text{Sn}(\text{C}_2\text{O}_4)_2]^{2-}$ ions formed can be calculated as:

$$n_{[\text{Sn}(\text{C}_2\text{O}_4)_2]^{2-}}(\text{formation}) = \frac{Q_{\text{t}}}{2F} = 2.58 \cdot 10^{-6} \text{ mol} \quad (12)$$

Whereas the amount of $[\text{Sn}(\text{C}_2\text{O}_4)_2]^{2-}$ ions consumed due to the precipitate of SnC_2O_4 particles via reaction (1c) can be calculated as:

$$n_{[\text{Sn}(\text{C}_2\text{O}_4)_2]^{2-}}(\text{consumption}) = R_{(1c)} \cdot t_1 = 1.28 \cdot 10^{-7} \text{ mol} \quad (13)$$

The percentage of consumption of $[\text{Sn}(\text{C}_2\text{O}_4)_2]^{2-}$ ions during the stage I anodization can thus be calculated as following:

$$\eta\% = \frac{n_{[\text{Sn}(\text{C}_2\text{O}_4)_2]^{2-}}(\text{consumption})}{n_{[\text{Sn}(\text{C}_2\text{O}_4)_2]^{2-}}(\text{formation})} \times 100\% = 4.96\% \quad (14)$$

The calculation thus confirms that during the anodization of Sn under the conditions studied, the majority of $[\text{Sn}(\text{C}_2\text{O}_4)_2]^{2-}$ ions accumulates in the electric double layer at the vicinity of Sn anode surface. The formation of stage-I SnC_2O_4 particles via reaction (1c) consumes only a small fraction of $[\text{Sn}(\text{C}_2\text{O}_4)_2]^{2-}$ ions formed (4.97% consumption at $U = 3 \text{ V}$). When the accumulated $[\text{Sn}(\text{C}_2\text{O}_4)_2]^{2-}$ ionic concentration reaches its equilibrium value in the electric double layer, the transition from the stage I to stage II occurs.

4.5. Conclusion

This study investigated the anodization behavior of Sn foil in 0.27 M oxalic acid at applied potentials of $U \leq 5 \text{ V}$. The anodization under these conditions produces crystalline SnC_2O_4 compound. The characteristics of the anodization i - t curve highlight three distinctive stages during anodization of Sn at these low applied potentials.

- (1) The stage I is characterized by a high plateau current density (i_{H}) associated with chemical process I described by reactions 1(a) to 1(c). The chemical equilibrium favors the formation of $\text{Sn}[\text{C}_2\text{O}_4]_2^{2-}$. Once $\text{Sn}[\text{C}_2\text{O}_4]_2^{2-}$ reaches its equilibrium concentration in the double layer near Sn anode, stage I transits into stage II and the system enters into passivation state. This study has also found that the stage I plateau current i_{H} increases linearly with the applied voltages, indicating the anodic dissolution rate in stage I is governed by the migration of $(\text{C}_2\text{O}_4)^{2-}$ ions in the electrolyte.
- (2) The stage II is marked by a rapid decrease in anodic current density due to passivation. The passivation is a result of in-situ conversion of Sn to form an intricate SnC_2O_4 passivation layer with unique pyramidal microstructures.
- (3) The stage III anodic dissolution occurs at a lower plateau current density. Sn^{2+} ions diffuse through the crevices bound the pyramidal islands on the passivation layer to react locally with $(\text{C}_2\text{O}_4)^{2-}$ ions to form stage III SnC_2O_4 polyhedron crystals. The exponential $i_{\text{stable}}-U$ relationship observed confirms that the ionic migration of Sn^{2+} ions is the rate-determining step for the anodization of stage III.

Acknowledgements

M. Wang wishes to acknowledge the scholarship support from the Chinese Scholarship Council and the University of Western Australia. We also acknowledge the experimental support of the Centre for Microscopy, Characterization and Microanalysis of the University of Western Australia for electron microscopy and microstructure analysis.

References

- [1] H. Masuda, K. Fukuda, Science 268 (1995) 1466-1468.

- [2] O. Jessensky, F. Müller, U. Gösele, *J. Electrochem. Soc.* 145 (1998) 3735-3740.
- [3] D. Gong, C. A. Grimes, O. K. Varghese, W. Hu, R. S. Singh, Z. Chen, E. C. Dickey, *J. Mater. Res.* 16 (2001) 3331-3334.
- [4] R. Beranek, H. Hildebrand, P. Schmuki, *Electrochem. Solid-State Lett.* 6 (2003) B12-B14.
- [5] J. Choi, J. H. Li, S. C. Lee, J. H. Chang, K. J. Kim, M. A. Cho, *Electrochim. Acta* 51 (2006) 5502-5507.
- [6] I. Sieber, B. Kannan, P. Schmuki, *Electrochem. Solid-State Lett.* 8 (2005) J10-J12.
- [7] X. Feng, T. J. LaTempa, J. I. Basham, G. K. Mor, O. K. Varghese, C. A. Grimes, *Nano Lett.* 10 (2010) 948-952.
- [8] I. V. Sieber, P. Schmuki, *J. Electrochem. Soc.* 152 (2005) C639-C644
- [9] W. Wei, J. M. Macak, N. K. Shrestha, P. Schmuki, *J. Electrochem. Soc.* 156 (2009) K104-K109.
- [10] H. Zheng, A. Z. Sadek, K. Latham, K. Kalantar-Zadeh, *Electrochem. Commun.* 11 (2009) 768-771.
- [11] H. Tsuchiya, P. Schmuki, *Electrochem. Commun.* 6 (2004) 1131-1134.
- [12] T. J. LaTempa, X. Feng, M. Paulose, C. A. Grimes, *J. Phys. Chem. C* 113 (2009) 16293-16298.
- [13] J. C. Vial, A. Bsiesy, F. Gaspard, R. Hérino, M. Ligeon, F. Muller, R. Romestain, R. M. Macfarlane, *Physical Review B* 45 (1992) 14171-14176.
- [14] K. Kim, J. Choi, T. S. Bae, *Appl. Phys. Lett.* 90 (2007) 181912.
- [15] Y. C. Shen, I. C. Leu, W. H. Lai, M. T. Wu, M. H. Hon, *J. Alloys Compd.* 454 (2008) L3-L9.
- [16] M. Yang, N. K. Shrestha, P. Schmuki, *Electrochim. Acta* 55 (2010) 7766-7771.
- [17] I. Paramasivam, J. M. Macak, P. Schmuki, *Electrochem. Commun.* 10 (2008) 71-75.
- [18] F. Schmidt-Stein, R. Hahn, J.-F. Gnichwitz, Y. Song, N. K. Shrestha, A. Hirsch, P. Schmuki, *Electrochem. Commun.* 11 (2009) 2077-2080.
- [19] E. Balaur, J. M. Macak, L. Taveira, P. Schmuki, *Electrochem. Commun.* 7 (2005)

1066-1070.

- [20] E. Balaur, J. M. Macak, H. Tsuchiya, P. Schmuki, *J. Mater. Chem.* 15 (2005) 4488-4491.
- [21] K. Shankar, James I. Basham, N. K. Allam, O. K. Varghese, G. K. Mor, X. Feng, M. Paulose, J. A. Seabold, K.-S. Choi, C. A. Grimes, *J. Phys. Chem. C* 113 (2009) 6327-6359.
- [22] G. K. Mor, K. Shankar, M. Paulose, O. K. Varghese, C. A. Grimes, *Appl. Phys. Lett.* 91 (2007) 152111.
- [23] J. R. Jennings, A. Ghicov, L. M. Peter, P. Schmuki, A. B. Walker, *J. Am. Chem. Soc.* 130 (2008) 13364-13372.
- [24] H. Föll, M. Leisner, A. Cojocaru, J. Carstensen, *Materials* 3 (2010) 3006-3076.
- [25] P. G. Harrison, C. Bailey, W. Azelee, *J. Catal.* 186 (1999) 147-159.
- [26] Z. Miao, Y. Wu, X. Zhang, Z. Liu, B. Han, K. Ding, G. An, *J. Mater. Chem.* 17 (2007) 1791-1796.
- [27] G. Croft, M. J. Fuller, *Nature* 269 (1977) 585-586.
- [28] X. W. Lou, Y. Wang, C. Yuan, J. Y. Lee, L. A. Archer, *Adv. Mater.* 18 (2006) 2325-2329.
- [29] Y. Wang, J. Y. Lee, H. C. Zeng, *Chem. Mater.* 17 (2005) 3899-3903.
- [30] M. Batzill, U. Diebold, *Prog. Surf. Sci.* 79 (2005) 47-154.
- [31] J.-H. Jeun, S.-H. Hong, *Sens. Actuators, B* 151 (2010) 1-7.
- [32] J.-H. Jeun, H.-S. Ryu, S.-H. Hong, *J. Electrochem. Soc.* 156 (2009) J263-J266.
- [33] H.-C. Shin, J. Dong, M. Liu, *Adv. Mater.* 16 (2004) 237-240.
- [34] M. Wang, Y. Liu, D. Xue, D. Zhang, H. Yang, *Electrochim. Acta* 10.1016 / j.electacta.2011.07.085 (2011).
- [35] V. K. Gouda, E. N. Rizkalla, S. Abd-El-Wahab, E. M. Ibrahim, *Corros. Sci.* 21 (1981) 1-15
- [36] R. C. Weast, M. J. Astle, W. H. Beyer, *CRC Handbook of Chemistry and Physics* (68th Edition), CRC Press, Inc., Boca Raton, Florida, 1987-1988.
- [37] V. P. Parkhutik, V. I. Shershulsky, *J. Phys. D: Appl. Phys.* 25 (1992) 1258-1263.

- [38] M. M. Lohrengel, *Materials Science and Engineering R11* (1993) 243-294.
- [39] S. C. Hendy, N. J. Laycock, M. P. Ryan, *J. Electrochem. Soc.* 152 (2005) B271-B275.

CHAPTER 5. A Unified Thermodynamic Theory for the Formation of Anodized Metal Oxide Structures

Mingliang Wang, Yinong Liu and Hong Yang,

Electrochimica Acta, 62 (2012) 424-432.

Abstract

In this paper we propose a unified theory describing the rules governing the formation of various oxide and metal nanostructures via electrochemical anodization. Nanoporous metal oxides of various morphologies have been of keen interest owing to their potential for various functional applications in chemical and biomedical sensing, chemical and photocatalysis, energy conversion in batteries and supercapacitors. This unified theory, based on thermodynamic and electrochemical principles, explains that the formation of porous or compact metal oxide and porous metal structures is dictated by the reaction free energy balance between the electrochemical anodic formation of the metal oxide and the chemical dissolution of the metal oxide in the electrolyte. Based on this theory, a range of key experimental observations reported in the literature are explained, including (1) the selection of the formation of compact oxide, porous oxide or porous metal during anodization, (2) voltage dependence of thickness of compact oxides, and (3) in-situ pore perforation by step-wise reduction of anodization voltage.

Keywords: anodization, nanoporous materials, metal oxide, electrochemical synthesis, thermodynamics, pore perforation.

5.1. Introduction

It is known that electrochemical anodization is able to create intricate oxide structures of various metals, e.g., Al [1, 2], Ti [3-6], Nb [7], Ta [8, 9], W [10], Zr [11], Fe [12, 13], Sn [14] and Ni [15]. The various oxide structures formed may be classified into two basic types according to their physical morphology: compact oxides and porous oxides. Compact oxide thin surface layers (e.g., Al_2O_3) have been widely used for wear and corrosion resistance purposes for over a century [2], owing to their inherent hardness and chemical inertness. The application of porous oxides occurred much more recently, such as porous Al_2O_3 used for pigment retention for coloring [16]. More recently, porous metal oxides have attracted much heightened interests due to their technological potentials in some novel applications, e.g., fabrication templates for nanostructures [1, 17], photocatalysts for organics degradation [18, 19], self-cleaning substrates [20, 21] and solar cell electrodes [22-24].

The formation of compact oxide surface layers appears to be a natural and simple case, in the light of the established electrochemical theories. In contrast, the formation of porous oxides has attracted much discussion in the literature to explain the mechanisms. The main hypotheses may be summarized as following.

(1) Valve metal theory

Earlier explanations have been made based on the concept of “valve metals” [25, 26]. Despite the wide reference to “valve metals” in the literature and claims of them as being a prerequisite for the formation of porous metal oxides [26], there has not been any credible direct explanation of the link between their necessary properties and the formation mechanisms of their porous oxide structures. In fact, none of the following have been established or explained: (i) the definition of “valve metals”, (ii) the list or

the identification of “valve metals”, and (iii) the identification of which of the properties of the “valve metals” that contribute to the pore formation of the oxides.

The term “valve metal” was initially given to metals used in the making of vacuum valves, also known as vacuum tubes or electronic tubes [27]. These metals were found to have a special property that when covered with a thin layer of their own or alien oxide the rate of electron emission may increase significantly [28]. Largely stemming from this phenomenon, in some less scholarly literature, there have been claims that “valve metals” allow one-way electrical conductivity during electrochemical anodization, or a “valve effect”, i.e., the oxide allows the passage of an anodic current but not a cathodic current [29]. This is in fact nothing of the extraordinary but a common and natural phenomenon applicable to all metal oxides, by the basic electrochemical principle, i.e., an oxide is formed when an anodic current is applied and dissolved when the direction of the current is reversed to being cathodic.

The list of valve metals is also of an uncertainty. Güntherschulze et al. [29] classified many metals into those with complete valve effect (Al, Bi, Sb and Ta) and those with incomplete valve effect (Ag, Cd, Fe, Mg, Si, Sn, W, Zn and Zr). A particular metal may exhibit complete valve effect or incomplete valve effect depending on the electrolyte it is in. Young et al. [30] classified the various metals into the “most typical members”, including Al, Bi, Hf, Nb, Sb, Ta, W and Zr, and the “other elements”, including Be, Ge, Mg, Si, Sn, Ti and V. More recently, Ghicov et al. [26] considered Al, Ti, Ta, Nb, W, Hf and Zr as valve metals based on their ability to anodically form nanoporous structures. These classifications are mostly phenomenological and are lack of logical rationale and scientific justification.

Contrary to the popular claims, there are key experimental evidences that challenge the valve metal theory. For example, although Si is normally considered a valve metal, porous Si [31, 32], rather than SiO₂, forms during anodization in HF aqueous solution.

Ni is not considered a valve metal, yet porous NiO layer can be formed by anodizing Ni in HF/H₃PO₄ electrolyte [15].

In addition, neither has there been any firm explanation established of the prerequisite of “valve metals” for the formation of porous oxide, nor have there been credible explanations of the formation mechanisms of porous oxides. Two relatively more popular explanations are the electrical field assisted oxide dissolution theory and the plastic deformation flow of oxide theory, as discussed below.

(2) Electrical field-assisted oxide dissolution model

The formation process of porous (aluminium) oxide is described to occur in three stages during anodization [33, 34], including (i) initial formation of a continuous compact oxide layer, (ii) pitting of the compact oxide layer (as nucleation of the pores), and (iii) electrical field-assisted oxide dissolution (for the growth of the porous structure). This theory argues that the dissolution rate of Al₂O₃ increases in the presence of an applied electric field at the tip of a pit [35]. The dissolution of the oxide at the tip (the oxide-electrolyte interface) of a pore forms an equilibrium with the continued anodic formation of the oxide at the oxide-metal interface, creating a steady-state pore growth process [2, 35]. This theory is practically a phenomenological description of the oxide formation and growth process without much explanation. The unexplained claim that the oxide at the pore tip preferentially dissolves under the influence of the same electrical field that causes the formation of the oxide demands serious discussion.

(3) Plastic ionic flow model

In this model, pore formation in the anodized oxide is explained in terms of mass

migration of metal ions within the oxide from underneath the pores to pore wall [36-39]. This process is suggested to be driven by distribution of the anodization electrical field and compressive stresses within the oxide arising from electrostrictive effect and possibly oxide volume expansion. Garcia et al. [36] presented evidence of the curving of a tungsten tracer layer pre-impregnated within the Al metal underneath the pore of anodized Al_2O_3 to support this hypothesis. Oh et al. [40] also proposed that anodized Al_2O_3 pores are initiated as a result of mechanical instability with forced plastic deformation and flow of the oxide.

There exist some serious questions to this hypothesis. The volume expansion of the formation of compact anodized $\gamma\text{-Al}_2\text{O}_3$ is 1.28 [41]. Given an average pore volume fraction of 10% (a very conservative low estimate) in anodized porous Al_2O_3 [42] (Al anodizing in 0.3 M oxalic acid at 40 V), to form the pores by ionic migration, 10% of the material needs to move by an average lateral distance of typically ~55 nm (half of the inter-pore distance) into the pore walls in solid state. Secondly, it is insufficient, in fact inappropriate, to consider it as a case of an ionic species migrating in a solid matrix. Both the metal ions and the oxygen ions need to move in order to shift the volume of the oxide away from the pores to the wall. This is no other material to form a matrix within which such migration by diffusion is to occur, or possible. An alternative to this is that the ionized metal species move inside the existing oxide (the barrier layer) towards the walls and to complete their oxidation reaction at the oxide-electrolyte interface on the wall surfaces. This implies that the barrier layer is a moving body of the same oxide formed at the beginning on the surface. This also appears impossible.

It is our view that the current understanding of the underlying principles of the formation of porous metal oxides during anodization is inadequate, in fact much erroneous. For this we propose a new theory based on electrochemical and

thermodynamic principles, which is able to explain on the same principle the formation of compact metal oxides, porous metal oxide and porous metal structures as a result of anodization. To enable the discussion, we present a review summary of the key experimental observations first.

5.2. Experimental observations

A variety of anodized metal oxide morphologies have been reported in the literature, mostly with nano scale features. These include compact oxides [43, 44], ordered or randomly organized nano-channels [1, 45], nanotubes [46], and nano-porous sponge structures [14, 47]. Figure 1 shows SEM micrographs of several typical forms of anodized metal oxides. Figure 1(a) shows a solid, compact and continuous Al_2O_3 surface film [44]. Figure 1(b) shows a porous Al_2O_3 created by anodizing pure Al in $\text{H}_2\text{C}_2\text{O}_4$ electrolyte. The porous structure is characterized by the highly regular hexagonal arrangement of nano channels, typically ~ 35 nm in diameter. The channels are also highly regular and un-branched, as seen in the inset, which is a cross section view, and the depth can vary from 1 to 100 μm depending on anodization time [48, 49]. Figure 1(c) shows a porous TiO_2 [3]. This oxide has a tubular form. The tubes are monodirectional and perpendicular to the surface of the anode metal. It can grow up to 250 nm in height in 0.5 wt% HF electrolyte at 20 V. Figure 1(d) shows a porous SnO_2 formed by anodizing Sn in 0.5 M NaOH electrolyte at 12 V. The oxide has a sponge-like morphology with very high volume fraction of random pores [47].

In addition to the various forms of oxide, anodization may also produce porous surface structure of the parent metal without the oxide. Typical examples are porous Ge formed by anodization of Ge wafer in HCl solution [50, 51] and porous Si formed by anodization of Si wafer in HF solution [31, 32, 52]. Figure 1(e) shows an example of porous Ge formed by anodization in 5 wt% HCl electrolyte at 5 mA/cm^2 [51].

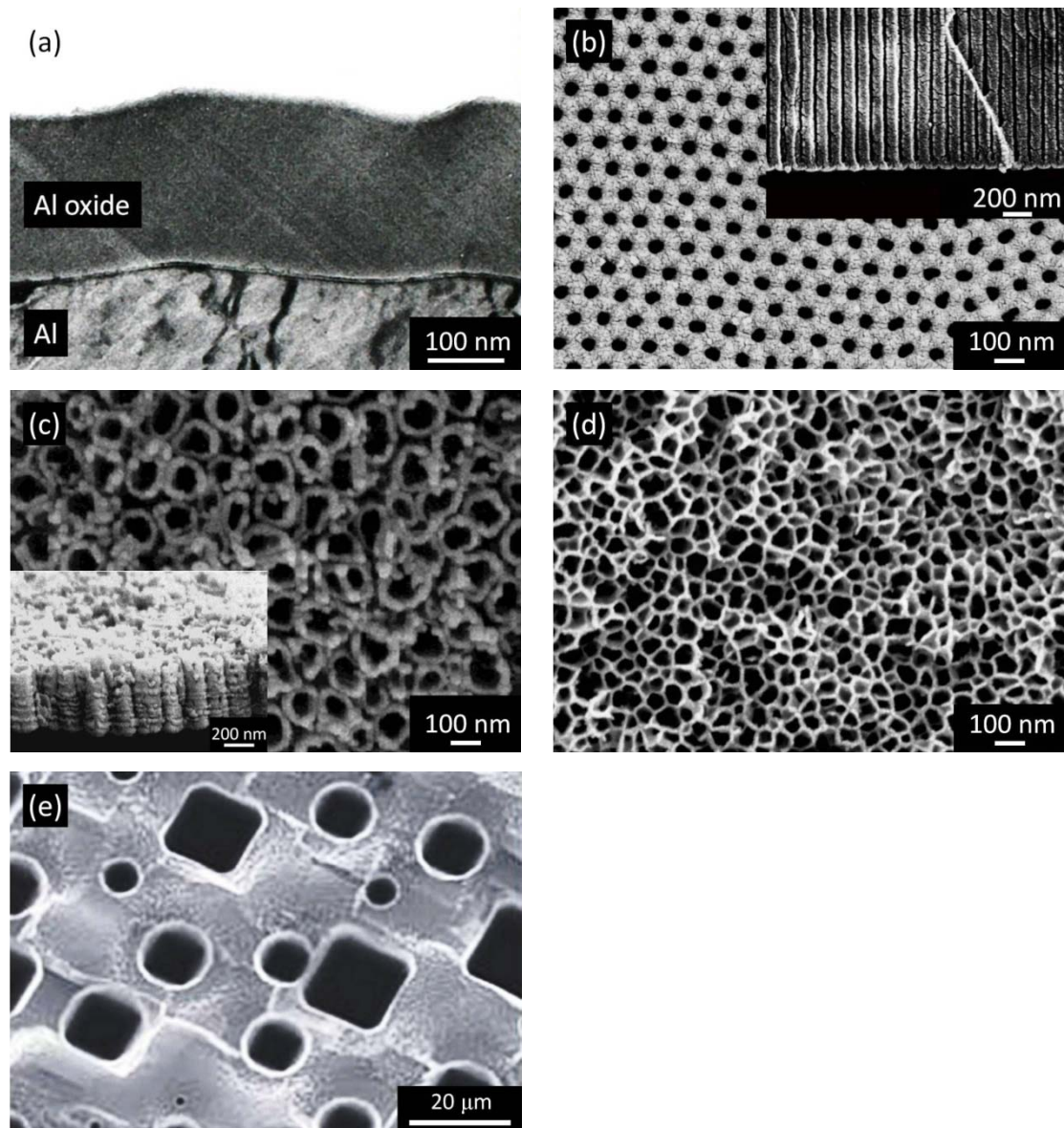


Figure 1. SEM micrographs showing typical morphologies of anodized metal oxides:

(a) side view of compact Al₂O₃ surface film (formed in 0.16 M (NH₄)₂C₄H₄O₆ electrolyte at 200 V) [44]; (b) top view and side view (inset) of ordered porous Al₂O₃ nano-channels (formed in 0.27 M H₂C₂O₄ electrolyte at 40 V) [1]; (c) top view and side view (inset) of nano-tubular porous TiO₂ (formed in 0.5 wt% HF electrolyte at 20 V) [3]; (d) porous sponge SnO₂ (formed in 0.5 M NaOH electrolyte at 12 V) [47], and (e) porous Ge formed by anodization in 5 wt% HCl electrolyte at 5 mA/cm² [51].

The various forms of anodized metal oxides may be classified into two major groups: compact oxides and porous oxides. These oxides share some key common features, as listed below:

- (1) Compact oxides usually have limited thickness determined by the applied anodization voltage, for a given anodization system. The thickness is independent of the anodization time after the initial growth. It has been reported that thickness of compact Al_2O_3 films formed in boric acid, citric acid or ammonium tartrate electrolytes have a voltage dependence of 1.4 nm/V [2], apparently independent of the nature of the three electrolytes mentioned above.
- (2) An oxide may grow into either compact or porous forms, depending on the electrolyte. Vast range of experimental observations suggest that compact oxides are formed in mild electrolytes, porous oxides are formed in moderately aggressive electrolytes (to the oxide) and porous metals are formed in highly aggressive electrolytes (to the oxide). For example, compact Al_2O_3 films may formed in weak acidic and near neutral solutions, e.g., boric acid, ammonium borate [2] and ammonium tartrate [44] electrolytes, whereas porous Al_2O_3 films form in stronger acidic electrolytes, e.g., H_2SO_4 , $\text{H}_2\text{C}_2\text{O}_4$ and H_3PO_4 [42, 48].
- (3) Porous oxides can grow indefinitely in thickness in mild electrolytes. In more aggressive electrolytes, e.g., fluoride containing electrolytes, some oxides have been found to grow to a certain thickness and remain in that thickness with continued anodization. The limited thickness mainly depends on the acidity of the electrolyte. For example, the layer thickness of anodized nanotubular porous TiO_2 can reach ~250 nm in 0.5 wt% HF electrolytes [3], but in $(\text{NH}_4)\text{H}_2\text{PO}_4$ (1 M) + 0.5 wt% NH_4F (0.5 wt%) electrolytes it can grow up to ~4 μm thick [53].
- (4) Porous oxides are always found to have a continuous barrier layer at the pore bottom. This layer is found to maintain a constant thickness for a given

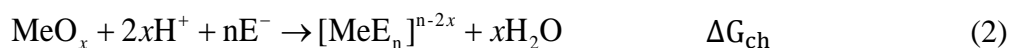
anodization system (electrolyte type and concentration, anodization voltage etc.). The thickness has been reported to linearly depend on the applied voltage e.g., ~1.3 nm/V for Al₂O₃ in H₂C₂O₄ solution [49] and ~2.5 nm/V for TiO₂ in (1 M H₂SO₄ + 0.15 wt% HF) electrolytes [26, 54].

- (5) The barrier layer may be perforated during anodization process, by progressively reducing the anodization voltage [55-57]. This observation is in fact of the same principle described in (4) above.
- (6) In highly aggressive electrolytes, porous metals may be formed without the formation of oxide, such as in the case of anodization of Si [31, 32] or Ge [58] in HF solution, and Ge in HCl [50, 51] solution.

The observation described in (2) indicates that whether an oxide layer is formed in compact form or porous form is not determined by the nature of the metal itself. The fact that porous oxide structures may form continuously with a steady barrier layer, as described in (3) and (4) above, implies that there must exist concurrent oxide formation and dissolution reactions in the same environment.

5.3. Thermodynamic analysis

It is clear from the descriptions above that a criterion for the formation of porous oxide structure is to have two concurrent reactions in the same anodization system [25], one for the electrochemical anodic formation of the metal oxide (MeO_x) and the other for the chemical dissolution of the same oxide in the same electrolyte, i.e.:



Reaction (1) is an electrochemical anodic reaction. Its Gibbs free energy change obeys Nernst equation and is a function of the electrode potential, i.e.,

$$\Delta G_{el} = -zFE \quad (3)$$

where z is the electron transfer number, F is the Faraday constant, and E is the electrode potential, which is influenced by the applied voltage U . It is to be noted that in an electrochemical cell, most of the applied voltage is consumed in the IR (current-resistance) drop of the conducting medium and a relatively small fraction of it manifests as the polarization potential on the electrodes. The absolute value of the over-potential on an electrode is expected to increase with increasing applied voltage. For the convenience of discussion below, when non-quantitative analysis is made, the applied voltage, which is an experimentally applied and variable parameter, is used in place of the electrode potential, which is the intrinsic parameter determining the Gibbs free energy change of the electrochemical reaction. Reaction (2) is a chemical reaction, with a free energy change (ΔG_{ch}) of a constant value irrespective of the applied voltage.

These two reactions may form three possible combinations according to their Gibbs free energy changes, as illustrated in Figure 2. In case (I), as illustrated in Figure 2(a), $\Delta G_{ch} > 0$ and is always greater than $\Delta G_{el}(U)$. In this case reaction (2) is not operative and only reaction (1) occurs. This leads to the formation of compact oxide. The compact oxide film is stable in the electrolyte at $U > U_o$ (more precisely, $E > E_o$), where U_o is the critical applied voltage at which $\Delta G_{el}(E) = 0$, or above which the metal oxide forms via reaction (1). A typical example of this condition is the compact Al_2O_3 oxide formed by anodization in ammonium tartrate electrolyte [44].

Case (II), as illustrated in Figure 2(b), represents the situation where ΔG_{ch} is always below ΔG_{el} (within the range of the applied voltage concerned). In this case, the metal oxide formed via reaction (1) is unstable and is instantaneously dissolved into the electrolyte via reaction (2). This is typically referred to as anodic etching. One example is the porous Si formed by electrochemical anodization in HF aqueous solution [31, 32, 59, 60].

Case (III) is represented in Figure 2(c), where the ΔG_{ch} and ΔG_{el} lines cross at a certain point. In this case, the axis of the applied voltage may be divided into three regions by two critical values. U_0 is the applied voltage at which $\Delta G_{\text{el}}=0$, as explained above. U^* is the applied voltage at which $\Delta G_{\text{ch}}=\Delta G_{\text{el}}$. In this regard:

- (1) In region I, where $U < U_0$, the metal oxide cannot be formed by anodization, because $\Delta G_{\text{el}} > 0$; Pre-existing oxide will be dissolved, because $\Delta G_{\text{ch}} < 0$; and the metal dissolves in the electrolyte directly upon anodization.
- (2) In region II, where $U_0 \leq U < U^*$, the metal oxide is formed but the oxide is unstable due to the prevalence of reaction (2), i.e., the oxide will be dissolved concurrently.
- (3) In region III, where $U \geq U^*$, the anodized metal oxide formed is stable to exist in the electrolyte, i.e., the oxide is protected by the anodic voltage against reaction (2).

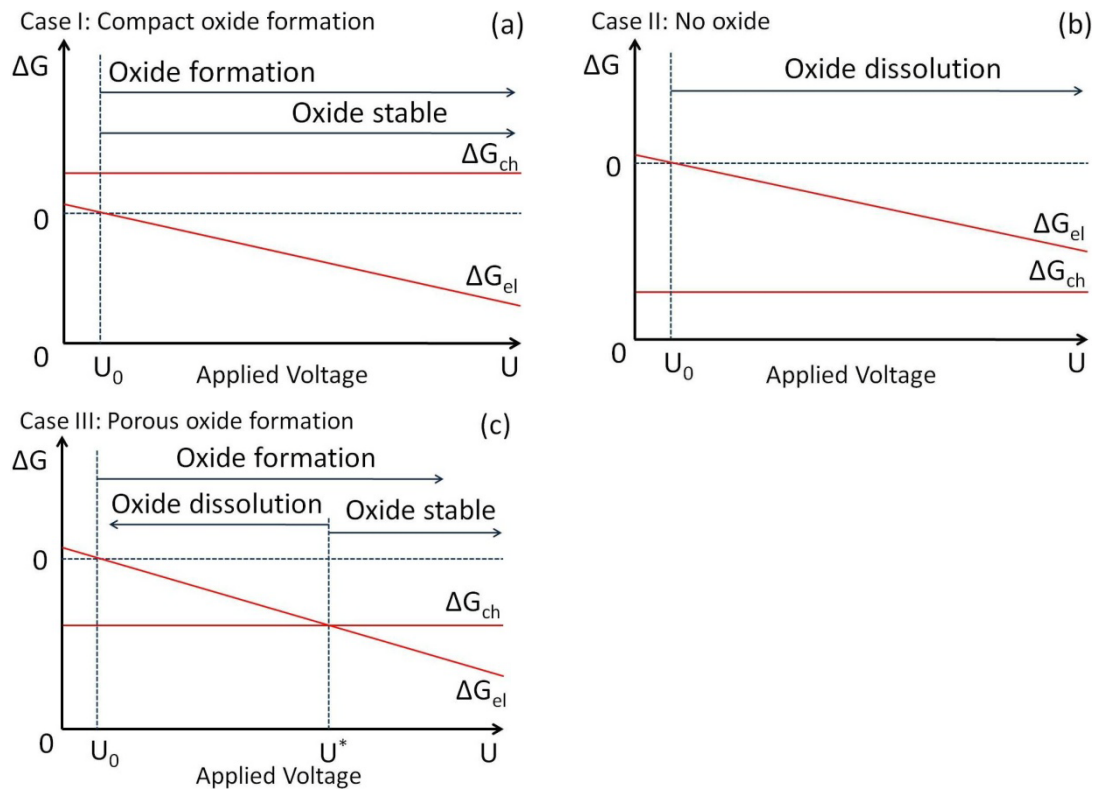


Figure 2. Schematic illustrations of thermodynamic analysis of the Gibbs free energy changes of the anodic formation of oxide (ΔG_{el}) and chemical dissolution of the oxide (ΔG_{ch}) in relation to the applied voltage. (a) Expresses the condition when only the electrochemical oxide formation reaction is active and compact oxide is formed; (b) expresses the condition when chemical dissolution of oxide is dominant and porous metal may be formed; (c) expresses the condition when both the electrochemical formation and the chemical dissolution of the oxide are active, resulting in the formation of porous oxide.

Table 1 shows a survey of electrochemical and chemical reactions for the formation of anodized metal oxides. In case I, in which compact oxides are formed, only electrochemical anodization reactions for metal oxide formation occur in the systems. The chemical dissolution reactions of the metal oxides have positive Gibbs free energy changes ($\Delta G_{ch}^0 > 0$) and are thermodynamically prohibited.

In case III, in which porous oxides are formed, the Gibbs free energy change of the oxide dissolution reaction is negative ($\Delta G_{ch}^0 < 0$), therefore both reactions may operate concurrently (satisfying the $U > U_0$ condition).

Table 1. Survey of electrochemical and chemical reactions for the formation of anodized metal oxides.

Metal oxide formation: Electrochemical reaction	Metal oxide dissolution: Chemical reaction	Electrolyte	ΔG_{ch}^0 (kJ/mol)
Case I: Compact oxide formation			
$2Al + 3H_2O \rightarrow Al_2O_3 + 6H^+ + 6e^-$	$Al_2O_3 + 6H_3BO_3 + 3H_2O \rightarrow 2Al^{3+} + 6B(OH)_4^-$	H_3BO_3	197.63
$2Al + 3H_2O \rightarrow Al_2O_3 + 6H^+ + 6e^-$	$Al_2O_3 + 2H_2B_4O_7 \rightarrow 2Al^{3+} + 3B_4O_7^{2-} + 2H_2O$	$H_2B_4O_7$	227.04
$2Al + 3H_2O \rightarrow Al_2O_3 + 6H^+ + 6e^-$	$Al_2O_3 + 3C_4H_6O_6 \rightarrow 2Al^{3+} + 3C_4H_4O_6^{2-} + 3H_2O$	$C_4H_6O_6$	
$Ti + 2H_2O \rightarrow TiO_2 + 4H^+ + 4e^-$	$TiO_2 + 2H_2SO_4 \rightarrow Ti(SO_4)_2 + 2H_2O$	H_2SO_4	
Case II: Porous metals			
$Si + H_2O \rightarrow SiO_2 + 4H^+ + 4e^-$	$SiO_2 + 6HF \rightarrow [SiF_6]^{2-} + 2H^+ + 2H_2O$	HF	-169.1
$Ge + H_2O \rightarrow GeO + 4H^+ + 4e^-$	$GeO_2 + 4H^+ + nF^- \rightarrow [GeF_n]^{n-4} + 2H_2O$	HF	
$Ge + H_2O \rightarrow GeO + 4H^+ + 4e^-$	$GeO_2 + 4H^+ + nCl^- \rightarrow [GeCl_n]^{n-4} + 2H_2O$	HCl	
Case III: Porous oxide formation			
$2Al + 3H_2O \rightarrow Al_2O_3 + 6H^+ + 6e^-$	$Al_2O_3 + 3H_2SO_4 \rightarrow 2Al^{3+} + 3SO_4^{2-} + 3H_2O$	H_2SO_4	-118.13
$2Al + 3H_2O \rightarrow Al_2O_3 + 6H^+ + 6e^-$	$Al_2O_3 + 3H_2C_2O_4 \rightarrow 2Al^{3+} + 3C_2O_4^{2-} + 3H_2O$	$H_2C_2O_4$	-118.14
$Ti + 2H_2O \rightarrow TiO_2 + 4H^+ + 4e^-$	$TiO_2 + 6HF \rightarrow H_2TiF_6 + 2H_2O$	HF	-45.76
$Sn + 4OH^- \rightarrow SnO_2 + 2H_2O + 4e^-$	$SnO_2 + 2NaOH \rightarrow Na_2SnO_3 + H_2O$	NaOH	-117.02
$2Fe + 3H_2O \rightarrow Fe_2O_3 + 6H^+ + 6e^-$	$Fe_2O_3 + 6H^+ + 12F^- \rightarrow 2[FeF_6]^{3-} + 3H_2O$ [12]	HF	
$W + 3H_2O \rightarrow WO_3 + 6H^+ + 6e^-$	$WO_3 + 6H^+ + nF^- \rightarrow [WF_n]^{n-6} + 3H_2O$ [65]	HF	
$Ni + H_2O \rightarrow NiO + 2H^+ + 2e^-$	$NiO + 2H^+ + nF^- \rightarrow [NiF_n]^{n-2} + H_2O$	HF	
$Hf + 2H_2O \rightarrow HfO_2 + 4H^+ + 4e^-$	$HfO_2 + 4H^+ + nF^- \rightarrow [HfF_n]^{n-4} + 2H_2O$	HF	
$2Nb + 5H_2O \rightarrow Nb_2O_5 + 10H^+ + 10e^-$	$Nb_2O_5 + 10H^+ + nF^- \rightarrow 2[NbF_n]^{n-5} + 5H_2O$	HF	
$2Ta + 5H_2O \rightarrow Ta_2O_5 + 10H^+ + 10e^-$	$Ta_2O_5 + 10H^+ + nF^- \rightarrow 2[TaF_n]^{n-5} + 5H_2O$	HF	
$Zr + 2H_2O \rightarrow ZrO_2 + 4H^+ + 4e^-$	$ZrO_2 + 4H^+ + nF^- \rightarrow [ZrF_n]^{n-4} + 2H_2O$	HF	

It is known that fluoride ion is a potent species to break down metal oxides, i.e., to cause metal oxide dissolution reactions with negative ΔG_{ch}^0 . A large number of comparative studies of anodization in electrolytes with and without F^- ions have been reported in the literature for various metals, including Ti [53], Hf [61], Nb [62], Ta [63], W [64] and Zr [11]. These studies demonstrate that porous oxide films are

formed in fluoride-containing electrolytes, whereas compact oxide films form in electrolytes containing no fluoride ions. These observations support the suggestion that the criterion for the formation of porous metal oxide is the concurrent operation of the electrochemical anodic formation of the oxide and the chemical dissolution of the oxide in the same electrolyte.

These criteria described above, based on electrochemical and thermodynamic principles, allow us to explain the conditions for the formation of three types of anodization products, including (i) porous oxide structures for both “valve metals” (e.g., Al, Ti, Hf, Nb, Ta, W and Zr) and non-valve metals (e.g., Ni), (ii) porous metals (e.g., Si and Ge), and (iii) compact oxide films.

5.4. Formation of compact oxides

A typical compact type oxide is Al_2O_3 film formed by anodization of Al in H_3BO_3 (pH=5) aqueous electrolyte [2]. In this case, the anodic oxidation of Al into Al_2O_3 is:



and the chemical dissolution of Al_2O_3 occurs as:



The formation Gibbs free energies of the compounds involved in the above equation are $\Delta G_{\text{Y-Al}_2\text{O}_3}^0 = -1563.85 \text{ kJ/mol}$, $\Delta G_{\text{H}_3\text{BO}_3}^0 = -968.85 \text{ kJ/mol}$, $\Delta G_{\text{H}_2\text{O}}^0 = -237.1 \text{ kJ/mol}$, $\Delta G_{\text{Al}^{3+}}^0 = -485.34 \text{ kJ/mol}$ and $\Delta G_{\text{B}(\text{OH})_4^-}^0 = -1153.52 \text{ kJ/mol}$ [66].

The free energy relationship between reaction (4) and reaction (5) conforms to Case I expressed in Figure 2(a). In this case, reaction (2) will not proceed and compact Al_2O_3 is formed.

Figure 3 shows a schematic illustration of the growth mechanism of an anodized compact oxide (as in the example of Al_2O_3 formed in 0.15 M H_3BO_3 (pH=5) aqueous electrolyte). Figure 3(a) illustrates the initial condition, when a voltage is applied on the bare Al anode and a cathode. The applied voltage is linearly distributed within the electrolyte between the two electrodes, and the current obeys Ohm's law based on the conductivity of the electrolyte and the geometry of the cell.

Figure 3(b) expresses the situation when a thin layer of the compact oxide is formed. The applied voltage U is then shared by two conducting media in serial connection between the two electrodes (ignoring the IR drop within the electrode and the polarizations of the electrodes), i.e.:

$$U = \Delta U_{\text{ox}} + \Delta U_{\text{el}} \quad (6)$$

where ΔU_{ox} is the IR voltage drop across the oxide and ΔU_{el} is the IR voltage drop across the electrolyte. Given that (as per Ohms' Law):

$$\Delta U_{\text{ox}} = R_{\text{Al}_2\text{O}_3} i = \rho_{\text{Al}_2\text{O}_3} t_{\text{ox}} i \quad (7a)$$

$$\Delta U_{\text{el}} = R_{\text{el}}(\text{H}_3\text{BO}_3) i = \rho_{(0.15\text{M-H}_3\text{BO}_3)} D i \quad (7b)$$

Solving equations (6) and (7) simultaneously gives:

$$\Delta U_{\text{ox}} = U \left(1 - \frac{\rho_{(0.15\text{M-H}_3\text{BO}_3)} D}{\rho_{(0.15\text{M-H}_3\text{BO}_3)} D + \rho_{\text{Al}_2\text{O}_3} t_{\text{ox}}} \right) \quad (8a)$$

$$U_{\text{b}} = U - \Delta U_{\text{ox}} = U \frac{\rho_{(0.15\text{M-H}_3\text{BO}_3)} D}{\rho_{(0.15\text{M-H}_3\text{BO}_3)} D + \rho_{\text{Al}_2\text{O}_3} t_{\text{ox}}} \quad (8b)$$

where i is the current density, t_{ox} is the thickness of the compact oxide, U_{b} is the voltage at the oxide/electrolyte interface, $\rho_{\text{Al}_2\text{O}_3}$ is the electrical resistivity of Al_2O_3 ,

taken as $1 \times 10^{13} \text{ } \Omega \cdot \text{m}$ [66], $\rho_{(0.15\text{M}-\text{H}_3\text{BO}_3)}$ is the electrical resistivity of the electrolyte used, at $6.04 \times 10^{-4} \text{ } \Omega \cdot \text{m}$ as experimentally determined in this work, and D is the working distance between the anode and cathode, 0.1 m normally.

For the particular experiment described above, $\Delta U_{\text{ox}}/U$ and U_{b}/U may be computed as functions of t_{ox} , as shown in Figure 3(c). It is seen that $\Delta U_{\text{ox}}/U$ increases rapidly with increasing t_{ox} . At $t_{\text{ox}} > 40 \text{ nm}$, 87% of the voltage drop occurs within the oxide layer. For a typical oxide barrier layer of $t_{\text{ox}} = 200 \text{ nm}$, $\Delta U_{\text{ox}}/U = 97\%$ and $U_{\text{b}}/U = 3\%$.

Figure 3(d) shows the process of growth of the oxide layer. As the oxide layer grows into the metal substrate (ignoring the volume change of the oxide relative to the metal), the voltage at the interface decreases continuously with the increase of the oxide layer thickness. The growth of the oxide layer stops when the voltage at the oxide-electrolyte interface is decreased to $U_{\text{b}} = U_0$ where $\Delta G_{\text{el}} = 0$. This criterion practically dictates that the anodized compact oxide thickness is independent of anodization time after the initial period of growth and is controlled by the applied voltage.

This prediction is consistent with the many experimental observations. Diggle et al. [2] reported that the anodized compact Al_2O_3 layer thickness is not affected by anodization time once completely formed, but only linearly dependent on the applied voltage, with a coefficient of $\sim 1.4 \text{ nm/V}$, in boric acid, citric acid or ammonium tartrate electrolytes.

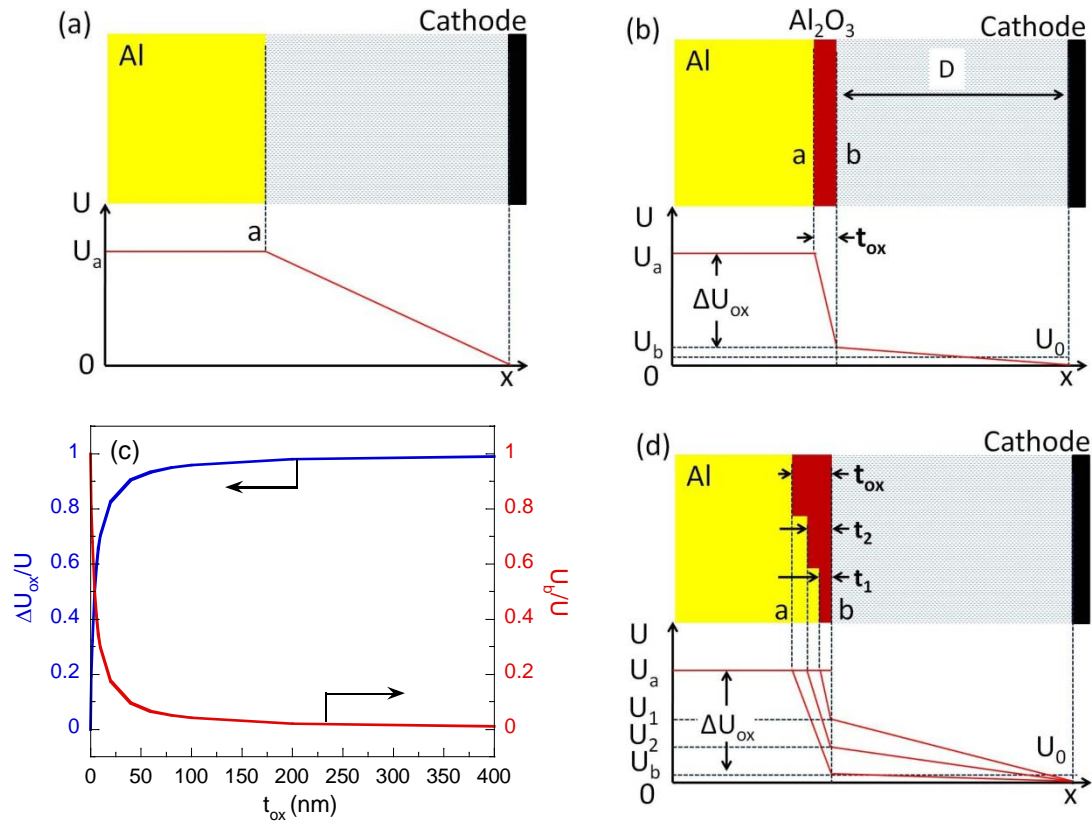


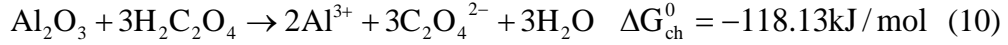
Figure 3. Schematic illustration of the mechanism of formation of compact type aluminium oxide: (a) beginning state when the applied voltage is linearly distributed within the electrolyte; (b) distribution of the applied voltage when a layer of the oxide is formed, (c) effect of oxide layer thickness on the sharing of the voltage drop in the oxide (ΔU_{ox}) and in the electrolyte (U_b), as computed using equation (8); and (d) analysis of the growth of the compact oxide to an equilibrium thickness.

5.5. Porous oxide formation

As discussed above, a porous oxide forms when the metal is anodized under condition III (Figure 2(c)). A typical example is the porous Al_2O_3 formed in (0.3 M) $H_2C_2O_4$ aqueous electrolyte. In this case, the anodic oxidation of Al into Al_2O_3 occurs as per reaction (9):



and the chemical dissolution of Al_2O_3 occurs via reaction:



where $\Delta G_{\text{Y-Al}_2\text{O}_3}^0 = -1563.85 \text{ kJ/mol}$, $\Delta G_{\text{H}_2\text{C}_2\text{O}_4}^0 = -674.04 \text{ kJ/mol}$, $\Delta G_{\text{Al}^{3+}}^0 = -485.34 \text{ kJ/mol}$, $\Delta G_{(\text{C}_2\text{O}_4)^{2-}}^0 = -674.04 \text{ kJ/mol}$, and $\Delta G_{\text{H}_2\text{O}}^0 = -237.1 \text{ kJ/mol}$ [66].

Reaction (9) is an electrochemical reaction. Its free energy change obeys Nernst equation and is a function of the applied voltage, i.e., $\Delta G_{\text{el}} = -zFE$. At $\Delta G_{\text{el}} = \Delta G_{\text{ch}}^0$, U^* is defined.

Figure 4 shows a schematic illustration of the formation process of anodized porous oxide. Figures 4(a) expresses the anodic formation of a continuous and compact oxide layer, also known as the barrier layer. This process is similar to the case of compact oxide discussed above. The growth of the compact oxide layer stops at certain thickness (t_{barrier}) when $U_b = U^*$. However, given that in this case both reactions (9) and (10) are active, and that at the $\text{Al}_2\text{O}_3/\text{electrolyte}$ interface, where $U_b = U^*$, the oxide has the minimum protection from the applied anodic voltage, the oxide will be attacked by reaction (10), causing random pitting and perturbation on the oxide surface, as indicated by the arrow in Figure 4(a).

Figure 4(b) shows an enlarged view of the local situation at the bottom of a shallow pit. Under this condition, the anodic current redistributes (relative to a flat oxide layer) and converge towards point 1 at the bottom of the concaved surface, where the oxide thickness is the smallest and the electrical path to the underlying metal is the shortest. The current density distribution is schematically shown below the pit. The anodic current density is effectively the growth rate of the oxide into the underlying metal. This means that the originally flat oxide/metal interface is bulging out under the bottom of the pit, as indicated by the dashed locus. Continuation of this process creates a wavy oxide/metal interface matching the profile of the oxide/electrolyte interface, as shown in Figure 4(c).

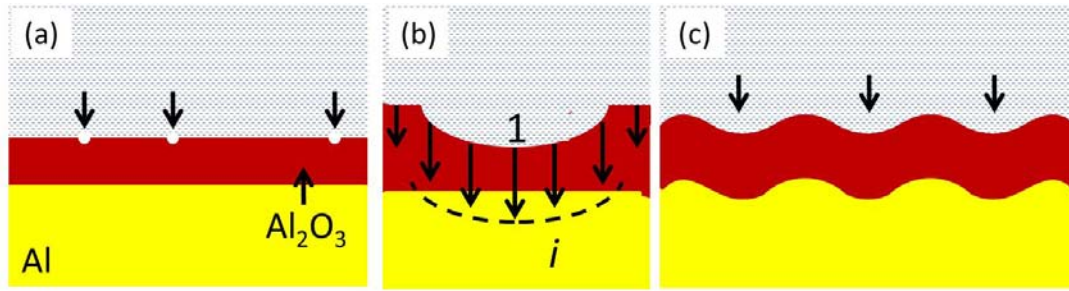


Figure 4. Schematic illustration of the pore initiation and formation mechanism for anodized porous oxide; (a) initiation of pores; (b) concentration of anodic current density at the bottom of a pit and protrusion of the metal-oxide interface under the pit; (c) starting of porous structure formation.

Figure 5 illustrates the condition for pore growth. As discussed above, in an electrochemical cell, the oxide layer and the electrolyte body effectively form an electrical circuit in serial connection. For the situation depicted in Figure 5, the electrical potential distributions along line A and line B are different, as schematically expressed in the lower part of the figure. U_{a1} and U_{b1} are the applied voltage (neglecting the voltage drop within the metal electrode). U_{a2} and U_{b2} are the voltages at the oxide-electrolyte interface on lines A and B, respectively. They can be determined using equation (8b). It is easy to recognize that $U_{a2} \approx U_{b2}$ and it is apparent that the voltage along line B is greater than that along line A in the entire region inside the body of the oxide. As discussed above, the oxide is stable at locations where $U > U^*$. This implies that only the oxide at the surface (e.g., at a2 and b2) will chemically dissolve and the rest (the body of the oxide) is protected by the applied voltage.

It is also obvious that the total electrical resistance along line A is much lower than that along line B. This means that the net current passing along line A is much greater than that along line B. This leads to the preferential oxide formation/dissolution along line B. This means that the preferential formation and growth of the porous structure is self-promoted and maintained, resulting in the continued stable stage growth of the porous structure.

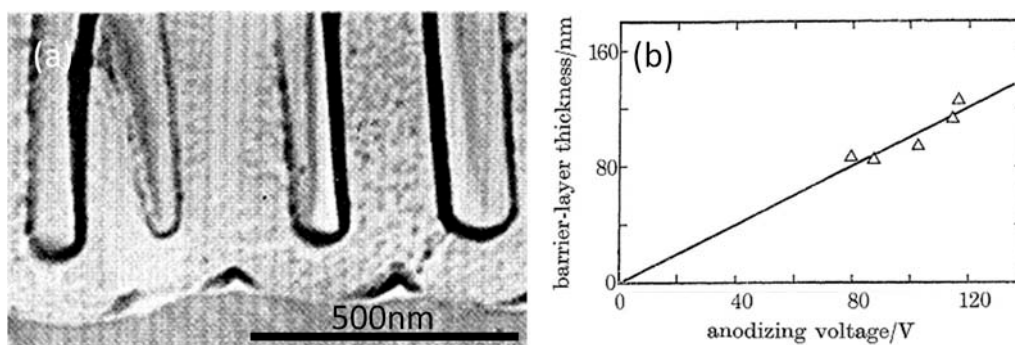


Figure 6. (a) Side view of porous aluminium oxide formed by anodization of Al in 0.4 M H_3PO_4 solution at 115 V and (b) effect of applied cell voltage on the porous oxide barrier layer thickness (t_{barrier}) [54].

This discussion also demonstrates that the voltage at the oxide-electrolyte interface everywhere is (practically) the same, as has been recognized by Houser et al. [67] and Li et al. [68]. This implies that the equilibrium between reactions (9) and (10) is maintained on the entire oxide-electrolyte interface of the porous structure.

5.6. Perforation of the barrier layer

For certain purposes, the barrier layer of a porous oxide needs to be removed, e.g., to allow electrochemical deposition of metallic nanowires through the pores [56]. Two methods have been used to remove the barrier layer. One method involves controlled chemical dissolution using acids, after removing the remaining metal substrate, e.g., using dilute H_3PO_4 solution as the etchant for Al_2O_3 [69, 70]. The chemical etching effect also enlarges the pore diameter in this process. The second method is in-situ perforation by step-wise reduction of the anodizing voltage [55-57], without the removal of the remaining metal substrate. This method has the advantages of maintaining the small nanopore size and using the substrate metal as the cathode for direct electrochemical deposition of metal nanostructures.

Figure 7 shows a schematic illustration of the in-situ electrochemical perforation

technique. Figure 7(a) shows a scheme of step-wise reduction of the anodization voltage. Figure 7(b) shows the progressive thinning of the barrier layer. At the initial anodization voltage U_1 , the barrier layer thickness is t_1 and the layer is stable. When U_1 is reduced to U_2 , the voltage at point “a” is below U^* , thus unstable. This means that the oxide is chemically encouraged to dissolve in the electrolyte. This will thin the barrier layer to thickness t_2 to establish a new equilibrium. Continued stepwise reduction of the applied voltage thus progressively thins the oxide layer down till perforation [56].

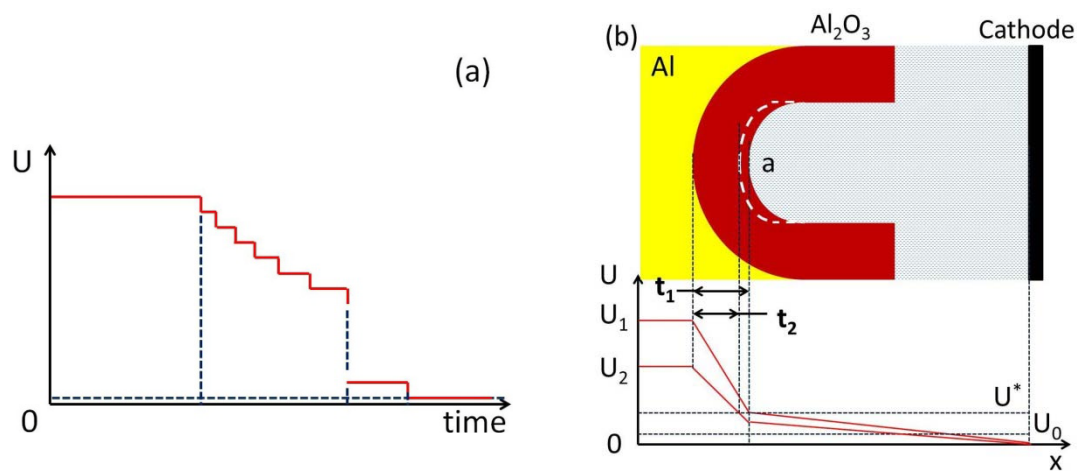


Figure 7. Schematic illustration of the mechanism of in-situ perforation of barrier layer: (a) stepwise reduction of applied voltage (U); (b) schematic illustration of barrier layer thinning and penetration of porous anodized aluminium oxide.

5.7. Formation of porous metals

A porous metal forms when the metal is anodized under condition II (Figure 2(b)). A typical example is the porous Si formed in 10 wt% HF aqueous electrolyte. In this case, anodic oxidation of Si into SiO_2 occurs as per reaction (11):



and the chemical dissolution of SiO_2 occurs via reaction:



$$\Delta G_{ch}^0 = -169.1 \text{ kJ/mol} \quad (12)$$

where $\Delta G_{SiO_2}^0 = -856.67 \text{ kJ/mol}$, $\Delta G_{HF}^0 = -274.66 \text{ kJ/mol}$, $\Delta G_{H^+}^0 = 0 \text{ kJ/mol}$, $\Delta G_{[SiF_6]^{2-}}^0 = -2199.53 \text{ kJ/mol}$, and $\Delta G_{H_2O}^0 = -237.1 \text{ kJ/mol}$ [66].

In this case, the Gibbs free energy change of reaction (12) is expected below that of reaction (11). The chemical dissolution of the anodic oxide dominates the process.

Generally two different growth mechanisms for porous metals have been proposed in the literatures [71]. Unagami et al. [72] suggested that direct local dissolution of the metal leads to the formation of porous metals. Parkhutik et al. [73] proposed that anodized porous metals are created in two steps by the formation of their oxides and the simultaneously dissolution of the oxides. According to the principle expressed in Figure 2(b), Parkhutik's hypothesis appears to be more credible.

5.8. Conclusions

This study proposes a unified theory for the formation of surface structures of metals induced by anodization. The theory is based on thermodynamic and electrochemical principles. The theory is able to explain the main experimental observations of all three types of anodic structures, including solid compact oxide films, porous oxides and porous metal surface layers. The criteria for the formation of each type of anodic structures may be summarized as following:

- (1) In an electrochemical anodization system two possible reactions may exist, i.e., the electrochemical anodic reaction for the formation of the metal oxide and the chemical dissolution of the metal oxide in the electrolyte (ΔG_{ch}). The Gibbs free

energy change of the electrochemical reaction (ΔG_{el} is a function of the over-potential of the electrode, which is influenced by the applied anodic voltage, as per Nernst equation, whereas that of the chemical dissolution reaction (ΔG_{ch}) is a constant in a given system. The relative prevalence of the two reactions determines the anodic structures that may form.

- (2) Compact oxide is formed when $\Delta G_{el} < 0$ and $\Delta G_{ch} > 0$. Under this condition the metal oxide formed does not dissolve.
- (3) When $\Delta G_{ch} < \Delta G_{el} < 0$, the metal oxide formed is unstable in the environment and will be dissolved instantaneously, resulting in the formation anodized porous metal.
- (4) When $\Delta G_{ch} < \Delta G_{el} < 0$, the metal oxide formed is protected by the electrical potential against chemical dissolution. Within the vicinity of the cross-point between ΔG_{el} and ΔG_{ch} , some part of the anodized metal oxide is dissolved and some part is protected, leading to the formation of porous oxide.

Acknowledgements

M. Wang wishes to acknowledge the scholarship support from the Chinese Scholarship Council and the University of Western Australia. We also acknowledge the experimental support of the Centre for Microscopy, Characterization and Microanalysis of the University of Western Australia for electron microscopy and microstructure analysis.

References

- [1] H. Masuda, K. Fukuda, Science 268 (1995) 1466-1468.

- [2] J. W. Diggle, T. C. Downie, C. W. Goulding, *Chemical Review* 69 (1969) 365-405.
- [3] D. Gong, C. A. Grimes, O. K. Varghese, W. Hu, R. S. Singh, Z. Chen, E. C. Dickey, *J. Mater. Res.* 16 (2001) 3331-3334.
- [4] R. Beranek, H. Hildebrand, P. Schmuki, *Electrochem. Solid-State Lett.* 6 (2003) B12-B14.
- [5] H. Hirakata, K. Ito, A. Yonezu, H. Tsuchiya, S. Fujimoto, K. Minoshima, *Acta Mater.* 58 (2010) 4956-4967.
- [6] F. Schmidt-Stein, S. Thiemann, S. Berger, R. Hahn, P. Schmuki, *Acta Mater.* 58 (2010) 6317-6323.
- [7] J. Choi, J. H. Li, S. C. Lee, J. H. Chang, K. J. Kim, M. A. Cho, *Electrochim. Acta* 51 (2006) 5502-5507.
- [8] I. Sieber, B. Kannan, P. Schmuki, *Electrochem. Solid-State Lett.* 8 (2005) J10-J12.
- [9] X. Feng, T. J. LaTempa, J. I. Basham, G. K. Mor, O. K. Varghese, C. A. Grimes, *Nano Lett.* 10 (2010) 948-952.
- [10] H. Zheng, A. Z. Sadek, K. Latham, K. Kalantar-Zadeh, *Electrochem. Commun.* 11 (2009) 768-771.
- [11] H. Tsuchiya, P. Schmuki, *Electrochem. Commun.* 6 (2004) 1131-1134.
- [12] T. J. LaTempa, X. Feng, M. Paulose, C. A. Grimes, *J. Phys. Chem. C* 113 (2009) 16293-16298.
- [13] H. E. Prakasam, O. K. Varghese, M. Paulose, G. K. Morand, C. A. Grimes, *Nanotechnology* 17 (2006) 4285-4291.
- [14] H.-C. Shin, J. Dong, M. Liu, *Adv. Mater.* 16 (2004) 237-240.
- [15] N. K. Shrestha, M. Yang, P. Schmuki, *Electrochem. Solid-State Lett.* 13 (2010) 21-24.
- [16] F. Keller, M. S. Hunter, D. L. Robinson, *J. Electrochem. Soc.* 100 (1953) 411-419
- [17] H. S. Shin, J. Yu, J. Y. Song, *Appl. Phys. Lett.* 91 (2007) 173106.

- [18] I. Paramasivam, J. M. Macak, P. Schmuki, *Electrochem. Commun.* 10 (2008) 71-75.
- [19] F. Schmidt-Stein, R. Hahn, J.-F. Gnichwitz, Y. Song, N. K. Shrestha, A. Hirsch, P. Schmuki, *Electrochem. Commun.* 11 (2009) 2077-2080.
- [20] E. Balaur, J. M. Macak, L. Taveira, P. Schmuki, *Electrochem. Commun.* 7 (2005) 1066-1070.
- [21] E. Balaur, J. M. Macak, H. Tsuchiya, P. Schmuki, *J. Mater. Chem.* 15 (2005) 4488-4491.
- [22] K. Shankar, James I. Basham, N. K. Allam, O. K. Varghese, G. K. Mor, X. Feng, M. Paulose, J. A. Seabold, K.-S. Choi, C. A. Grimes, *J. Phys. Chem. C* 113 (2009) 6327-6359.
- [23] G. K. Mor, K. Shankar, M. Paulose, O. K. Varghese, C. A. Grimes, *Appl. Phys. Lett.* 91 (2007) 152111.
- [24] J. R. Jennings, A. Ghicov, L. M. Peter, P. Schmuki, A. B. Walker, *J. Am. Chem. Soc.* 130 (2008) 13364-13372.
- [25] J. M. Macak, H. Tsuchiya, A. Ghicov, K. Yasuda, R. Hahn, S. Bauer, P. Schmuki, *Curr. Opin. Solid State Mater. Sci.* 11 (2007) 3-18.
- [26] A. Ghicov, P. Schmuki, *Chem. Commun.* (2009) 2791-2808.
- [27] J. F. Rider, *Inside the vacuum tube*, John F. Rider Publisher, INC., New York, 1945.
- [28] M. Ishii, S. Watanabe, A. Miyai, H. Hiraoka, Thermionic cathode, in: vol 4, 137,476, *Denki Kagaku Kogyo Kabushiki Kaisha*, United States Patent, 1979, p. 5.
- [29] A. Güntherschulze, H. Betz, *Elektrolytkondensatoren*, M. Krayn Verlag, Berlin (1937).
- [30] L. Young, *Anodic Oxide Films*, Academic Press, London, 1961.
- [31] R. L. Smith, S. D. Collins, *J. Appl. Phys.* 71 (1992) R1-R22.
- [32] J. C. Vial, A. Bsiesy, F. Gaspard, R. Hérino, M. Ligeon, F. Muller, R. Romestain, R. M. Macfarlane, *Physical Review B* 45 (1992) 14171-14176.
- [33] V. P. Parkhutik, *Corros. Sci.* 26 (1986) 295-310

- [34] V. P. Parkhutik, V. I. Shershulsky, *J. Phys. D: Appl. Phys.* 25 (1992) 1258-1263.
- [35] T. P. Hoar, N. F. Mott, *J. Phys. Chem. Solids* 9 (1959) 97-99
- [36] S. J. Garcia-Vergara, P. Skeldon, G. E. Thompson, H. Habazaki, *Electrochim. Acta* 52 (2006) 681-687.
- [37] S. J. Garcia-Vergara, P. Skeldon, G. E. Thompson, H. Habazaki, *Surf. Coat. Technol.* 201 (2007) 9506-9511.
- [38] S. J. Garcia-Vergara, P. Skeldon, G. E. Thompson, H. Habakaki, *Appl. Surf. Sci.* 254 (2007) 1534-1542.
- [39] S. J. Garcia-Vergara, P. Skeldon, G. E. Thompson, H. Habazaki, *Corros. Sci.* 50 (2008) 3179-3184.
- [40] J. Oh, C. V. Thompson, *Electrochim. Acta* 56 (2011) 4044-4051.
- [41] A. P. Li, F. Müller, A. Birner, K. Nielsch, U. Gösele, *J. Appl. Phys.* 84 (1998) 6023-6026.
- [42] K. Nielsch, J. Choi, K. Schwirn, R. B. Wehrspohn, U. Gösele, *Nano Lett.* 2 (2002) 677-680.
- [43] G. Dearnaley, *Thin Solid Films* 3 (1969) 161-174
- [44] R. C. Furneaux, G. E. Thompson, G. C. Wood, *Corros. Sci.* 18 (1978) 853-881.
- [45] G. E. Thompson, R. C. Furneaux, G. C. Wood, J. A. Richardson, J. S. Goode, *Nature* 272 (1978) 433-435.
- [46] P. Roy, S. Berger, P. Schmuki, *Angew. Chem. Int. Ed.* 50 (2011) 2904-2939.
- [47] M. Wang, Y. Liu, D. Xue, D. Zhang, H. Yang, *Electrochim. Acta* 10.1016/j.electacta.2011.07.085 (2011).
- [48] S. Shingubara, *J. Nanopart. Res.* 5 (2003) 17-30.
- [49] W. Lee, R. Ji, U. Gösele, K. Nielsch, *Nat. Mater.* 5 (2006) 741-747.
- [50] C. Fang, H. Föll, J. Carstensen, *J. Electroanal. Chem.* 589 (2006) 259-288.
- [51] C. Fang, H. Föll, J. Carstensen, S. Langa, *Physica Status Solidi (a)* 204 (2007) 1292-1296.

- [52] K. Uosaki, K. Okazaki, H. Kita, H. Takahashi, *Anal. Chem.* 62 (1990) 652-656.
- [53] A. Ghicov, H. Tsuchiya, J. M. Macak, P. Schmuki, *Electrochem. Commun.* 7 (2005) 505-509.
- [54] S. Berger, H. Tsuchiya, P. Schmuki, *Chem. Mater.* 20 (2008) 3245-3247.
- [55] K. Nielsch, F. Müller, A.-P. Li, U. Gösele, *Adv. Mater.* 8 (2000) 582-586.
- [56] R. C. Furneaux, W. R. Rigby, A. P. Davidson, *Nature* 337 (1989) 147-149.
- [57] Z. F. Zhou, Y. C. Zhou, Y. Pan, X. G. Wang, *Mater. Lett.* 62 (2008) 3419-3421.
- [58] E. G. Rojas, J. Hensen, J. Carstensen, H. Föll, R. Brendel, *J. Electrochem. Soc.* 158 (2011) D408-D411.
- [59] M. Christophersen, J. Carstensen, A. Feuerhake, H. Föll, *Mater. Sci. Eng., B* 69-70 (2000) 194-198.
- [60] H. Föll, M. Leisner, A. Cojocar, J. Carstensen, *Materials* 3 (2010) 3006-3076.
- [61] H. Tsuchiya, P. Schmuki, *Electrochem. Commun.* 7 (2005) 49-52.
- [62] I. Sieber, H. Hildebrand, A. Friedrich, P. Schmuki, *Electrochem. Commun.* 7 (2005) 97-100.
- [63] I. V. Sieber, P. Schmuki, *J. Electrochem. Soc.* 152 (2005) C639-C644
- [64] Y.-C. Nah, A. Ghicov, D. Kim, P. Schmuki, *Electrochem. Commun.* 10 (2008) 1777-1780.
- [65] W. Li, J. Li, X. Wang, S. Luo, J. Xiao, Q. Chen, *Electrochim. Acta* 56 (2010) 620-625.
- [66] R. C. Weast, M. J. Astle, W. H. Beyer, *CRC Handbook of Chemistry and Physics* (68th Edition), CRC Press, Inc., Boca Raton, Florida, 1987-1988.
- [67] J. E. Houser, K. R. Hebert, *Nat. Mater.* 8 (2009) 415-420.
- [68] D. Li, L. Zhao, C. Jiang, J. G. Lu, *Nano Lett.* 10 (2010) 2766-2771.
- [69] C. Y. Han, G. A. Willing, Z. Xiao, H. H. Wang, *Langmuir* 23 (2007) 1564-1568.
- [70] W. L. Xu, H. Chen, M. J. Zheng, G. Q. Ding, W. Z. Shen, *Opt. Mater.* 28 (2006) 1160-1165.

- [71] L. Santinacci, T. Djenizian, *C.R. Chim.* 11 (2008) 964-983.
- [72] T. Unagami, *J. Electrochem. Soc.* 127 (1980) 476-483.
- [73] V. P. Parkhutik, J. M. Albella, J. M. Martinez-Duart, J. M. Gomez-Rodriguez, A. M. Baro, V. I. Shershulsky, *Appl. Phys. Lett.* 62 (1993) 366-368.

CHAPTER 6. Growth Orientation Control of Co Nanowires Fabricated by Electrochemical Deposition Using Porous Alumina Templates

Mingliang Wang, Hong Yang and Yinong Liu,
submitted to *Crystal Growth & Design*, October 2011.

Abstract

In this paper we propose an analysis as generic criteria for preferential orientation growth of metallic nanowires during electrochemical deposition using nano-channeled templates. In this work pure Co nanowire arrays were synthesized by electrochemical deposition using porous anodized aluminium oxide templates. The nanowire arrays are found to exhibit near complete preferential single orientation long the wire axis. The preferential orientation changed with increasing the deposition voltage from $[0002]_{\text{hcp}}$, $[10\bar{1}0]_{\text{hcp}}$, $[1\bar{2}10]_{\text{hcp}}$ to $[110]_{\text{fcc}}$. The observation is explained in terms of nucleation thermodynamics and crystal growth kinetics. The analysis demonstrates that at low deposition potentials, the wire orientation is determined by the criterion of minimum total surface energy, with the close-packed surfaces forming the exterior of the crystals. At high deposition potentials, the crystal axial orientation is determined by the growth kinetics, i.e., directions of the fastest growth velocity. These criteria also appear to apply well to preferential growth of fcc metal nanowires, e.g., Ag, Au, Cu and Ni.

Keywords: anodization, anodized aluminium oxide template, electrochemical synthesis, nanowires

6.1. Introduction

Metallic nanowire arrays created by electrochemical deposition using regular nanochannel templates have stimulated keen research interests in the recent years [1-3]. These materials are characteristic of high length-to-diameter ratios (typically greater than 1000) [1], small lateral dimensions and high population density (typically 10^8 wires/mm²) or large numbers (typically in the order of 2.5×10^9 over an area of 5×5 mm) can be fabricated in rare or complex substructures, like single crystals [4, 5], bamboo structures [6], or core/shell structures [7]. In addition to the above, there is also the possibility to create large quantity of metallic nanowires of near perfect, defect-free crystal structures, which have the potential to approach the theoretical limit of metallic bonds for materials strength and elasticity. Owing to these unique characteristics and promises, metallic nanowire arrays hold the promises to offer a wide range of rare properties for innovative applications. Examples of the interests have included magnetic storage media [8-10], nano-sensors [11] and as model materials for the understanding of fundamental magnetism theories at the nanoscale [12-14].

Much of the performance of the attempted and anticipated applications of metallic nanowire arrays depends on, or can be optimized by, the crystallographic orientation of the wires. For example, magnetic properties of a nanowire array (e.g., Fe, Co and Ni) are strongly dependent on crystal orientation due to magnetic anisotropy of the crystal [15-17]. The ultimate strength and elasticity of nanowires are also dependent on nanowire orientation, due to elastic constant anisotropy of the crystal structure [18]. Owing to these reasons, it is of intrinsic interest to establish the knowledge and to develop techniques to manipulate and control the orientations of nanowire arrays.

Electrochemical deposition using porous anodized aluminium oxide (AAO) templates is a popular technique used for nanowire synthesis. It has been reported in the

literature that the deposited nanowires grow with certain preferential axial crystallographic orientations, which appear to be influenced by electrochemical deposition potentials [5, 8, 19, 20]. The observed axial orientations include both the normal directions of close-packed planes (e.g., $[0001]_{\text{hcp}}$ and $[111]_{\text{fcc}}$) and non-close-packed planes (e.g., $[10\bar{1}0]_{\text{hcp}}$ and $[110]_{\text{fcc}}$) [15]. The close-packed planes normally have the lowest surface energies and are thus expected to form the front exposed surface of a growing nanowire. For nanowires grown along the non-close-packed planes, Pan et al. [5, 19] suggested that H^+ ions in the electrolyte stabilize the crystal planes of high surface energies (e.g., $(110)_{\text{fcc}}$) by surface adsorption, promoting their growth [5, 21, 22].

In this work, we studied the growth behavior of oriented pure Co nanowires synthesized by electrochemical deposition using AAO templates, in particular the deposition potential dependence of the axial orientations of the nanowires. An analysis based on thermodynamics and crystallography is presented to determine the criteria for the preferential orientation selection of metallic nanowires during electrochemical deposition using nano-channeled templates.

6.2. Experimental procedures

Porous anodized aluminium oxide (AAO) templates were prepared following a two-step anodization procedure [23]. A high purity (99.99 at%) Al thin plate of 400 μm thick was used. Sample coupons were ultrasonically cleaned in acetone, ethanol and deionized water and then electrochemically polished in an aqueous solution of sulfuric acid (25 wt%), phosphoric acid (25 wt%) and deionized water (50 wt%). The first anodization was performed at 40 V in a 3 wt% oxalic acid aqueous solution at room temperature for 6 hours. The porous alumina formed was removed using an

etchant solution containing 18 g/l chromic acid and 60 g/l phosphoric acid at 80°C for 1 hour. The second anodization was performed under the same conditions. The remaining Al was removed in 10 wt% CuCl₂ solution. The barrier layer was removed by etching in 5 wt% H₃PO₄ at 30°C for 60 minutes. The etching also widened the pore diameter to ~60 nm.

To facilitate electrodeposition, a 200 nm gold layer was coated by means of thermal evaporation onto the back of the AAO templates as the working electrode. Electrochemical deposition of nanowires was performed in a two-electrode cell. The electrolyte used for Co nanowires deposition was an aqueous solution containing 0.2 M CoSO₄ and 0.1 M H₃BO₃. A series of deposition potentials (U) from 2.2 to 5.4 V were applied using a DC regulated power supply.

The structure and morphology of the deposited nanowires were characterized by means of X-ray powder diffraction (XRD), scanning electron microscopy (SEM) and transmission electron microscopy (TEM). XRD was conducted using a Siemens D5000 Diffractometer with Cu K_α radiation ($\lambda = 0.1542$ nm). XRD was conducted on the surface perpendicular to the lengths of the nanowires. SEM examination was conducted using a Zeiss 1555 field emission scanning electron microscope. TEM was conducted using a JEOL 2100 analytical microscope. TEM samples were prepared as following. A small piece of AAO/Co nanowires sample was immersed in 1 M NaOH solution at 30°C for 1 hour to dissolve the alumina template. The remaining Co nanowires, some were still attached to the gold film and some had detached from the gold substrate and become loose wires, were washed using distilled water and ethanol for several times. The loose Co nanowires were dispersed into ethanol ultrasonically, and a drop of this solution was loaded on a Cu grid for TEM characterization.

6.3. Results and Discussions

Figure 1 shows SEM micrographs of (a) an anodized porous alumina template (top view) and (b) Co nanowire arrays deposited using the template. It is seen that the pores are in hexagonally ordered arrangement with diameters of ~ 60 nm. In figure 1(b), the alumina template has been dissolved in 1 M NaOH solution, exposing the wires. The Co nanowires are ~ 40 μm in length.

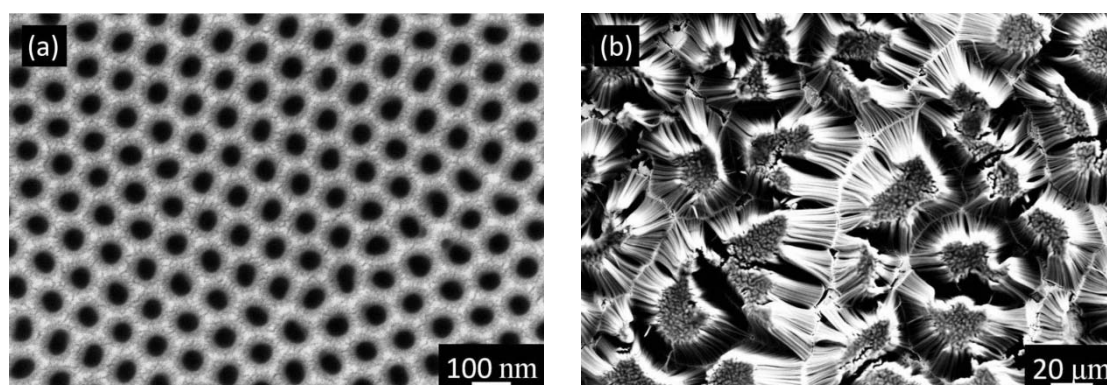


Figure 1. SEM micrographs (a) a porous alumina template and (b) Co nanowires deposited using the template (the alumina template has been removed by chemical etching in 1 M NaOH solution).

Figure 2(a) shows XRD spectra of Co nanowires deposited at different deposition potentials (U). The XRD spectra were taken of the plane perpendicular to the wire axial directions, as schematically shown in Figure 2(b). At the bottom of the spectra standard diffraction peak positions and intensities of hcp-Co and fcc-Co are shown for reference. The XRD spectra of the samples deposited at $U = 2.2$ V and 2.4 V are fully indexed to hcp-Co with clear preferential orientation of $(0002)_{\text{hcp}}$ perpendicular to the wire axes. A small diffraction peak for $(10\bar{1}0)_{\text{hcp}}$ is also visible. When deposited at $U = 2.7$ V, the Co nanowires displayed complete orientation selection of $(10\bar{1}0)_{\text{hcp}}$. At $U = 3$ V, the Co nanowires showed a clear peak at $2\theta = 75.9^\circ$ and the peak at $2\theta = 41.7^\circ$ for $(10\bar{1}0)_{\text{hcp}}$ has become much weaker, as shown in the inset. At $U \geq 3.6$ V, the peak

at $2\theta = 75.9^\circ$ became the sole peak, indicating complete orientation selection. This peak can be indexed to either $(11\bar{2}0)_{\text{hcp}}$ or $(110)_{\text{fcc}}$, which have practically the same 2θ position for Co.

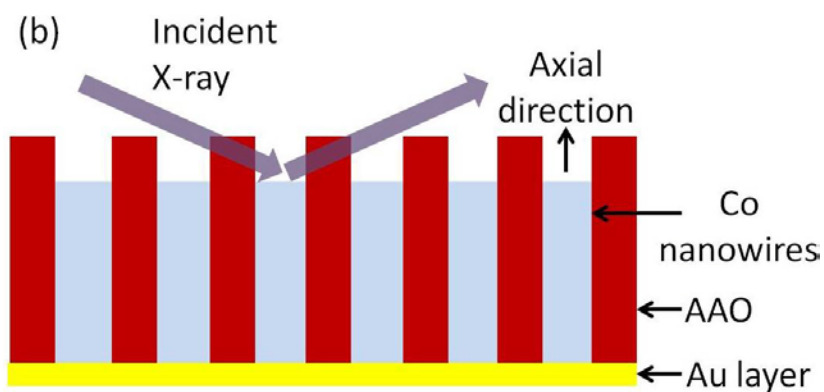
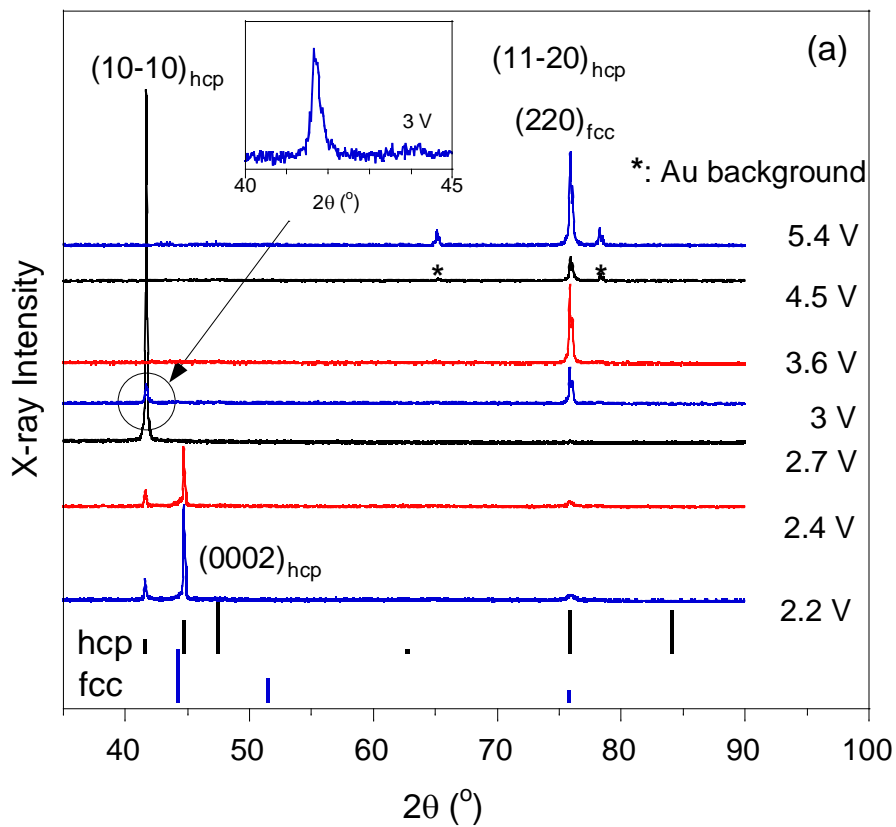


Figure 2. XRD spectra of electrochemically deposited Co nanowires.

Figure 3 shows TEM micrographs with corresponding selected area electron diffraction (SAED) patterns of Co nanowires.

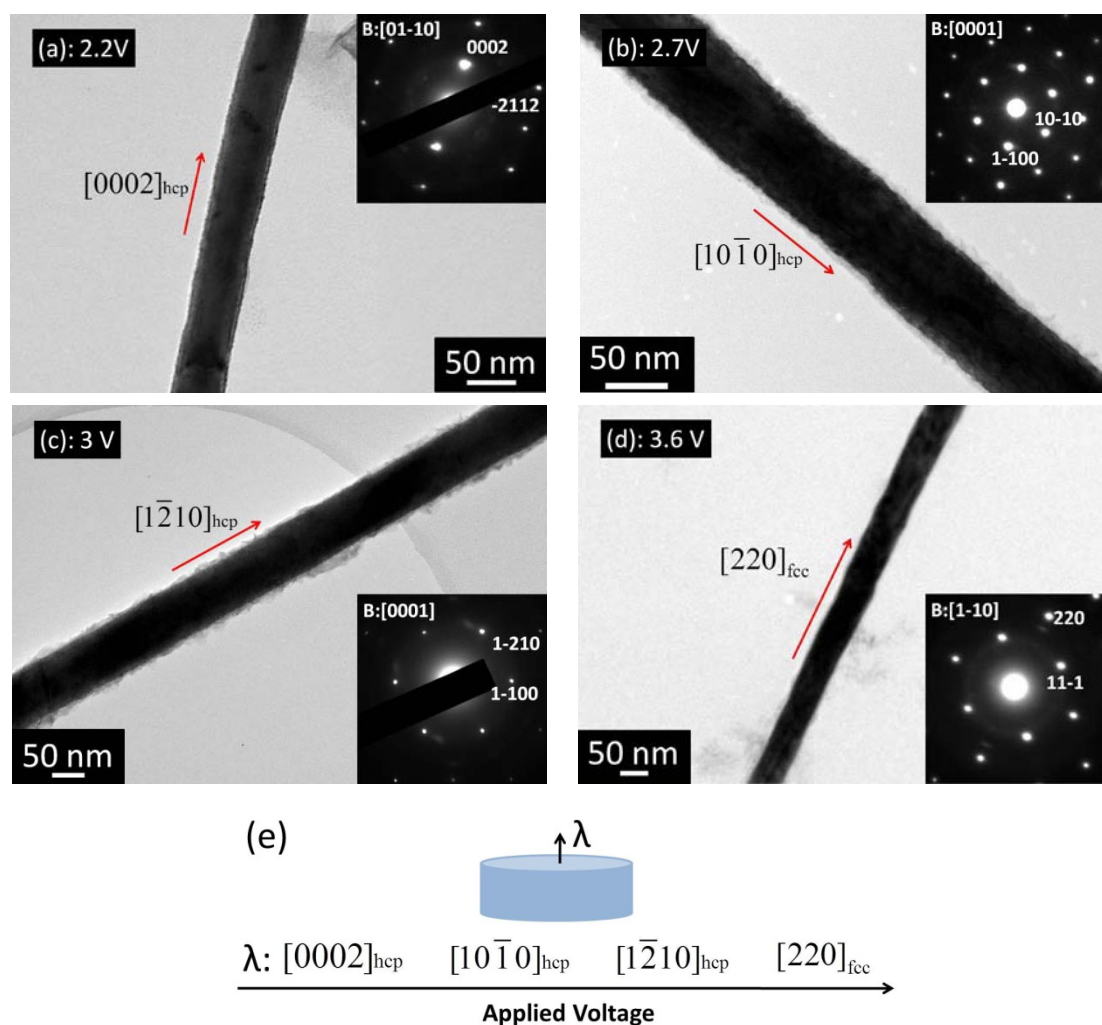


Figure 3. TEM micrographs and SAED patterns of Co nanowires deposited at different deposition potentials: (a) $U = 2.2\text{ V}$, (b) $U = 2.7\text{ V}$, (c) $U = 3\text{ V}$ and (d) $U = 3.6\text{ V}$; (e) shows a schematic of the dependence of the preferential axial orientation of the wires on deposition potential.

Micrograph (a) shows a wire deposited at $U = 2.2\text{ V}$. The single strand Co wire is $\sim 60\text{ nm}$ in diameter, same as the size of the pores of the alumina template. The wire is single crystalline and the growth direction is $[0002]_{hcp}$, as derived from its SAED pattern. SAED patterns taken at different locations along the length of the wire

confirm the single crystallinity and the common axial orientation. Similarly, the wires deposited at $U = 2.7$ V (figure 3(b)), 3 V (figure 3(c)) and 3.6 V (figure 3(d)) are mostly found to be single crystals. The axial orientations of the nanowires are determined to be $[10\bar{1}0]_{\text{hcp}}$ for $U = 2.7$ V, $[1\bar{2}10]_{\text{hcp}}$ for $U = 3$ V and $[110]_{\text{fcc}}$ for $U = 3.6$ V. In addition, the SAED allowed the differentiation between $(1\bar{2}10)_{\text{hcp}}$ and $(110)_{\text{fcc}}$.

Figure 3(e) presents a schematic of the dependence of the preferential orientation on deposition potential, as observed experimentally. The Co nanowire orientation evolves from $[0002]_{\text{hcp}}$, $[10\bar{1}0]_{\text{hcp}}$, $[1\bar{2}10]_{\text{hcp}}$ to $[110]_{\text{fcc}}$ with increasing deposition potential. This is in total agreement with the XRD observations shown in figure 2. It is seen that there is a polymorphism transition induced by higher deposition potentials, from hcp-Co to fcc-Co at $U \geq 3.6$ V.

The nucleation of metal nanowires by electrochemical deposition has been discussed by many researchers [4, 5, 19, 22] based on the classic thermodynamics nucleation theory. It is considered that in electrochemical deposition, the free energy of formation of a nucleus of N atoms ($\Delta G(N)$) has two components [21]:

$$\Delta G(N) = -\Delta G_v(N) + \varphi(N) \quad (1)$$

where $\Delta G_v(N)$ is the volume free energy change related to the transfer of N ions from solution to the crystal phase nucleus, and $\varphi(N)$ is the surface energy of the nucleus created. $\Delta G_v(N)$ is a function of the applied voltage (more precisely reduction potential of the ions on the crystal electrode) and provides the driving force for the nucleation, whereas $\varphi(N)$ is a resistive force. Therefore, $\Delta G(N_c) = 0$, or $\Delta G_v(N_c) = \varphi(N_c)$, defines the critical size of the nucleus.

Based on this theory, Plieth et al. [24] proposed the relation between the critical

dimension N_c and the surface energy of the formed crystal plane (hkl). Considering a metallic nanowire nucleus as a hemisphere-shaped crystal with radius of r , the critical dimension N_c can be determined as:

$$N_c = \frac{16\pi\sigma_{hkl}^3}{3z^3F^3|\eta|^3} \quad (2)$$

where z is the ionic valence, η is overpotential of the reduction reaction of the ions, and λ_{hkl} is the surface energy of the crystal face (hkl) that forms the exterior of the nucleus. It is obvious that crystal planes of low surface energies are favorable in nucleation. Surface energies of hcp-Co structure increase in the order of {0001}, $\{10\bar{1}0\}$ and $\{1\bar{2}10\}$ [25], i.e.:

$$N_c(0001) < N_c(10\bar{1}0) < N_c(1\bar{2}10) \quad (3)$$

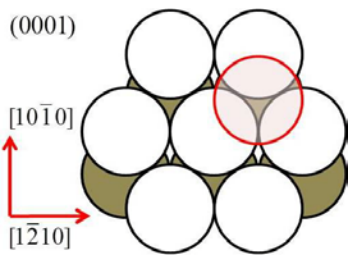
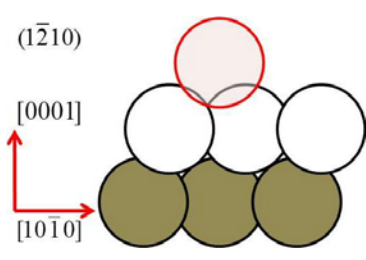
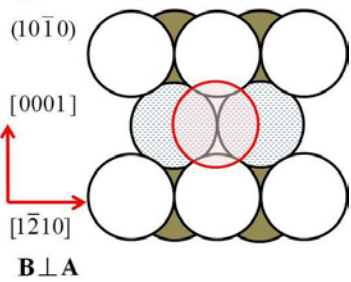
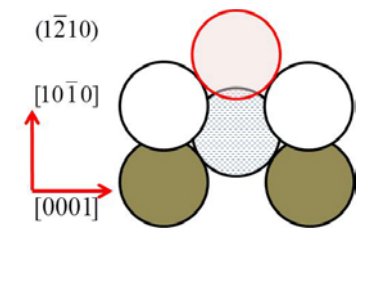
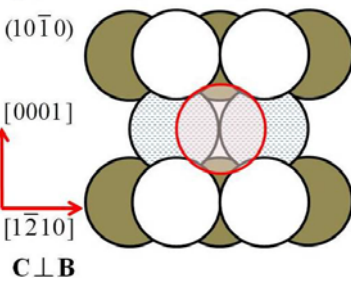
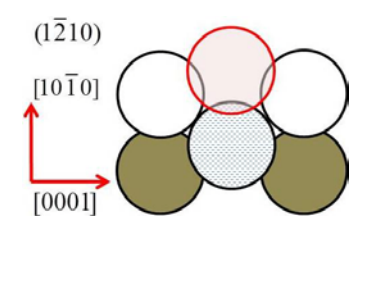
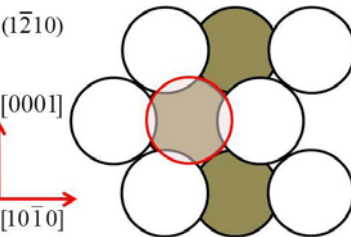
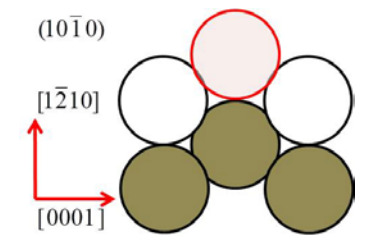
According to this criterion, (0001) plane will be the face plane of the disk shaped nucleus. This is consistent with the preferred orientation of the Co nanowires deposited at low voltages ($U \leq 2.4$ V).

However, at higher deposition potentials, Co nanowires in $[10\bar{1}0]$ and $[1\bar{2}10]$ preferential axial orientations are formed. This obviously deviates from the minimum surface energy criterion expressed above. This growth habit is attributed to the influence of growth kinetics, or growth rate of the growing crystal planes.

The growth kinetics of a crystal growing plane is much determined by the probability of an arriving atom to stick to a site on the plane. The attaching probability is determined by the strength of the interatomic bonds within the solid and the number of bonds of the site, or the (surface) coordination number. Table 1 presents a structure analysis of the main low-index crystal planes of hcp structure. The first column shows the top view of the growing plane (growing in the normal direction to the plane). The

atom in red is an arriving atom (ion) from the solution. The second column shows the side view parallel to the growing plane. The third column shows the stacking order of the growing plane. The fourth column shows the coordination number for the arriving atom on the growing plane.

Table 1. Structure analysis of hcp crystal planes

Adhesion sites in on low index planes		Stacking order	Surface coordination number (n)
Top view	Side view		
<p>(0001)</p>  <p>[10$\bar{1}$0] [1$\bar{2}$10]</p>	<p>(1$\bar{2}$10)</p>  <p>[0001] [10$\bar{1}$0]</p>	AB	3
<p>(1): A or C plane exposed</p> <p>(10$\bar{1}$0)</p>  <p>[0001] [1$\bar{2}$10]</p> <p>B \perp A</p>	<p>(1$\bar{2}$10)</p>  <p>[10$\bar{1}$0] [0001]</p>	[AB-CD-]	4
<p>(2): B or D plane exposed</p> <p>(10$\bar{1}$0)</p>  <p>[0001] [1$\bar{2}$10]</p> <p>C \perp B</p>	<p>(1$\bar{2}$10)</p>  <p>[10$\bar{1}$0] [0001]</p>	[AB-CD-]	6
<p>(1$\bar{2}$10)</p>  <p>[0001] [10$\bar{1}$0]</p>	<p>(10$\bar{1}$0)</p>  <p>[1$\bar{2}$10] [0001]</p>	[AB]	5

The first row shows the case of (0001) plane. This is the closed-packed plane of hcp structure and has a stacking order of [AB] along the [0001] direction. The arriving atom has 3 nearest neighbours, i.e., a coordination number of 3. For (10 $\bar{1}$ 0) plane, the stacking order is [AB-CD-] along its normal direction (as shown in Table S1 in the supporting material). There exist two different situations for the exposed plane profile. A and C planes have identical structure, as shown in the second row in Table 1. B and D planes are also identical but have a different structure from A and C, as shown in the third row in the table. When (10 $\bar{1}$ 0)_A or (10 $\bar{1}$ 0)_C plane is exposed, the arriving atom has 4 nearest coordinators. When (10 $\bar{1}$ 0)_B or (10 $\bar{1}$ 0)_D plane is exposed, the arriving atom has 6 nearest coordinators. This means that when B and D planes are exposed, the atomic sites in the new plane above (A and C) will be filled up more quickly compared to when A and C planes are exposed. In this case, the growth rate is dictated by the slower growing planes (i.e., A and C). The situation of (1 $\bar{2}$ 10) plane is shown in the last row. This plane has a stacking order of [AB] and a coordination number of 5. Therefore, the planar coordination number of the low index planes has the relationship of:

$$n_{(0001)} < n_{(10\bar{1}0)} < n_{(1\bar{2}10)} \quad (4)$$

A second parameter influencing crystal formation is the surface energy of the crystallographic planes. Table 2 shows structural parameters of Co (hcp) crystal planes, including the planar atomic packing density, inter-plane spacing (d_{space}) and surface energy of the three low index planes. Two entries are given for (10 $\bar{1}$ 0), corresponding to the A and C planes and B and D planes. Crystal planes of higher atomic packing densities generally have smaller surface energies. It is seen that the surface energies of the planes follow the increasing order of:

$$\sigma_{(0001)} < \sigma_{(10\bar{1}0)_{A,C}} < \sigma_{(1\bar{2}10)} \quad (5)$$

where $(10\bar{1}0)_{A,C}$ plane is used as the limiting condition for the growth in $[10\bar{1}0]$ direction.

Table 2. Structural parameters of Co (hcp) crystal planes.

Low index plane	Planar atomic packing density	d_{space} (R: atomic radius)	Surface energy (for Co [25]) (J/m ²)
(0001)	0.903	1.64R	2.994
$(10\bar{1}0)_{A,C}$	0.802	1.16R	3.421
$(10\bar{1}0)_{B,D}$	0.441	0.58R	5.219
$(1\bar{2}10)$	0.555	R	4.841

Figure 4 shows schematic drawings of (a) nanowire electrochemical deposition along AAO channels and (b) free energy analysis of electrochemical deposition process at a given deposition potential.

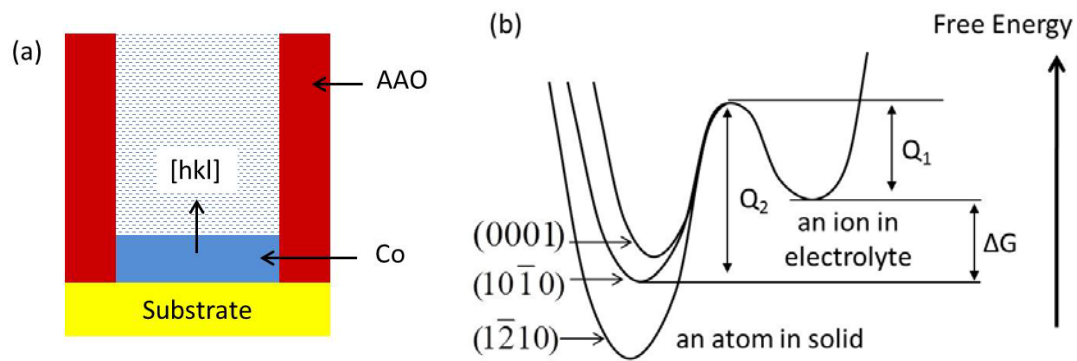


Figure 4. Schematic drawings of (a) nanowire electrochemical deposition along AAO channels, and (b) free energy analysis of electrochemical deposition process at a given deposition potential.

At a given deposition potential, the probability ($P_{S(hkl)}$) of one ion from the electrolyte to adhere to an atomic site on the solid (hkl) plane may be expressed as:

$$P_{S(hkl)} = \frac{k_B T}{h} \exp\left(-\frac{Q_1}{RT}\right) \quad (6)$$

where k_B is Boltzmann Constant, T is the absolute temperature, h is Plank constant, R is ideal gas constant, Q_1 is the barrier energy for the conversion of one ion in the electrolyte to one atom in the solid (Figure 4(b)).

At the meantime, atoms in the solid may ionize back into the electrolyte. The probability ($P_{L[hkl]}$) of one atom adhered on (hkl) plane migrating into the electrolyte is expressed as:

$$P_{L[hkl]} = \frac{k_B T}{h} \exp\left(-\frac{Q_2(hkl)}{RT}\right) \quad (7)$$

where $Q_2(hkl)$ is the barrier energy for the conversion of an atom in the solid (hkl) plane to an ion in the electrolyte (Figure 4(b)). Therefore, the probability of net deposition along the normal direction of the (hkl) plane at a given deposition potential is given as:

$$P_{[hkl]} = P_{S(hkl)} - P_{L[hkl]} = \frac{k_B T}{h} \left[\exp\left(-\frac{Q_1}{RT}\right) - \exp\left(-\frac{Q_2(hkl)}{RT}\right) \right] \quad (8)$$

As expressed in relationship (4), the coordination number increases for the planes in the order of $n_{(0001)} < n_{(10\bar{1}0)} < n_{(1\bar{2}10)}$. A higher coordination number means stronger bonding for the arriving atom, which in turn implies higher activation energy ($Q_2(hkl)$) for the atom to dissolve into the electrolyte, i.e.:

$$Q_{2(0001)} < Q_{2(10\bar{1}0)} < Q_{2(1\bar{2}10)} \quad (9)$$

Considering equations (8) and relationship (9), the net atomic adhesion probabilities in the normal directions of the three planes can be expressed as,

$$P_{[0001]} < P_{[10\bar{1}0]} < P_{[1\bar{2}10]} \quad (10)$$

Relationship (10) actually describes the relationship among the growth rates along the normal directions of a (hkl) planes during electrochemical deposition.

Considering relationships (5) and (10), it can be stated that the (0001) plane has the lowest surface energy and (1 $\bar{2}$ 10) plane has the highest normal growth rate. Referring to the experimental observations summarized in Figure 3(e), it can be concluded that at low deposition potentials, when the growth rate is low, the formation orientation of the nanowire crystals is dictated by minimum surface energy criterion and at high deposition potentials, when the growth rate is high, the nanowire axial orientation is dictated by the growth kinetics criterion.

The above analysis can also be applied to fcc metals (e.g., Ag, Au, Cu and Ni). Table 3 shows a summary of electrodeposited elemental nanowires of typical hcp and fcc metals. It is seen that the axial orientations of fcc metal nanowires evolve with increasing deposition voltage in the order of:

$$[111] \rightarrow [100] \rightarrow [110] \quad (11)$$

Table 3. Summary of electrodeposited element nanowires of typical hcp and fcc metals.

Metal	Structure	Growth direction	Deposition condition	Reference
Co	hcp fcc	[10 $\bar{1}$ 0] [110]	1.45 V 3 V	[26]
Co	hcp	[0001] [10 $\bar{1}$ 0]	5 mA/cm ² 50 mA/cm ²	[15, 27]
Ag	fcc	[111] [110]	-0.05 V vs Ag/AgCl -0.25 V vs Ag/AgCl	[28]
Au	fcc	[111] [111]&[100]&[110]	-0.75 V (SCE*) -1.2 V (SCE)	[4]
Cu	fcc	[111] [110]	-0.15V (SCE) -0.45V (SCE)	[29] [30]
Cu	fcc	[111]&[100]&[110] [110]	0.5 V 2 V	[31]
Ni	fcc	[111]&[100]&[110] [110]	0.5 mA/cm ² 2.5 mA/cm ²	[32]
Ni	fcc	[111]&[100]&[110] [110]	0.4 V 4 V	[5]

- SCE is saturated calomel electrode.

Table 4 shows crystal plane parameters for the three low-index crystal planes of fcc structure, as in the case of Ni, including the crystal planar atomic packing density, inter-plane spacing (d_{space}) and surface energy. It is seen that the surface energy (e.g., Ni [33]) is in the order of $\sigma_{(111)} < \sigma_{(100)} < \sigma_{(110)}$, implying that the critical dimension for nanowire nucleation is in the order of:

$$N_c(111) < N_c(100) < N_c(110) \quad (12)$$

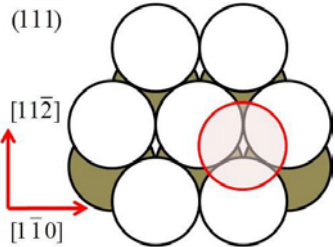
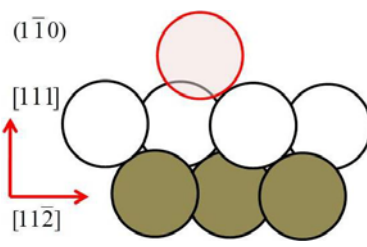
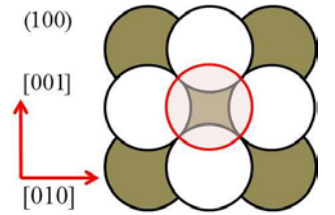
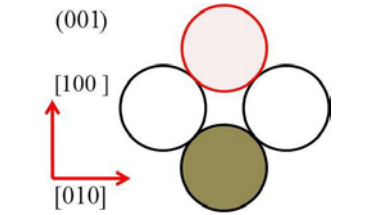
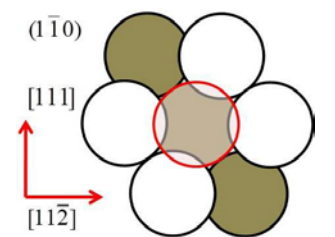
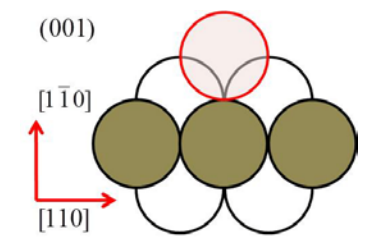
Table 4. Structure parameters of Ni (fcc) crystal planes.

Low index plane	Planar atomic packing density	d_{space} (R: atomic radius)	Surface energy (for Ni [33]) (J/m ²)
(111)	0.903	1.64R	1.171
(100)	0.802	1.414R	1.305
(110)	0.555	R	1.417

Table 5 shows the structure analysis of the three low-index crystal planes of fcc structure. It is seen that the planar coordination number of the planes, hence the growth rate of the nanowires in the normal directions, is in the order of:

$$n_{(111)} < n_{(100)} < n_{(110)} \quad (13)$$

Table 5. Structure analysis of fcc crystal planes.

Adhesion sites on low index planes		Stacking order	Surface coordination number (n)
Top view	Side view		
(111) 	(1-10) 	AB	3
(100) 	(001) 	AB	4
(1-10) 	(001) 	AB	5

Relationships (12) and (13) imply that for electrochemical deposition of fcc metal nanowires, [111] is the preferential axial orientation at low deposition potentials, due to low surface energy of the (111) plane, and [110] is the preferential axial orientation at high deposition potentials, due to its high growth kinetics. This conclusion is obviously consistent with the experimental observations summarized in Table 3.

It is admitted that the analysis did not attempt to explain the polymorphic change of Co from hcp to fcc with increasing the deposition potential to above 3.6 V in the given system. For Co, $(1\bar{2}10)_{\text{hcp}}$ and $(110)_{\text{fcc}}$ planes have the same structure parameters, including planar atomic packing density, planar coordination number and inter-plane spacing. The theory presented above does not provide means to explain this transition.

6.4. Conclusions

1. In this work, pure Co nanowires are synthesized by electrochemical deposition into nano-channels of porous anodized aluminium oxide templates. The nanowires formed are predominantly single crystals with uniform preferential axial orientation. The preferential orientation is found to change with increasing deposition potential, in the order of $[0002]_{\text{hcp}}$, $[10\bar{1}0]_{\text{hcp}}$, $[1\bar{2}10]_{\text{hcp}}$ and $[110]_{\text{fcc}}$.
2. The variation of the preferential axial orientation of the nanowires is explained in terms of two governing criteria. At low deposition potentials the axial orientation is dictated by nucleation thermodynamics, which obeys the criterion of minimum surface energy. This criterion dictates that the round face of thin disk shaped nucleus is (0001) for hcp metals and (111) for fcc metals. At high deposition potentials, the axial orientation is dictated by the criterion of maximum crystal growth kinetics. Crystal planes of high planar coordination numbers have high

growth rates and are thus preferred to be the exposed plane of the growth front. This criterion dictates that the axial orientation is the normal direction of $(1\bar{2}10)$ for hcp metals and (110) for fcc metals.

3. The criteria for nanowire axial preferential orientation in electrochemical deposition proposed above appears to be applicable to both hcp and fcc metals.

Acknowledgements

M. Wang wishes to acknowledge the scholarship support from the Chinese Scholarship Council and the University of Western Australia. We also acknowledge the experimental support of the Centre for Microscopy, Characterization and Microanalysis of the University of Western Australia for electron microscopy and microstructure analysis.

References

- (1) S. V. N. T. Kuchibhatla, A. S. Karakoti, D. Bera, S. Seal, *Prog. Mater Sci.* 52 (2007) 699-913.
- (2) S. Shingubara, *J. Nanopart. Res.* 5 (2003) 17-30.
- (3) W. LI, J. ZHANG, T. SHEN, J. G. A, G. P. J, *SCIENCE CHINA Physics, Mechanics & Astronomy* 54 (2011) 1181-1189
- (4) M. Tian, J. Wang, J. Kurtz, T. E. Mallouk, M. H. W. Chan, *Nano Lett.* 3 (2003) 919-923.
- (5) H. Pan, B. Liu, J. Yi, C. Poh, S. Lim, J. Ding, Y. Feng, C. H. A. Huan, J. Lin, *J. Phys. Chem. B* 109 (2005) 3094-3098.
- (6) Y.-K. Su, D.-H. Qin, H.-L. Zhang, H. Li, H.-L. Li, *Chem. Phys. Lett.* 388 (2004) 406-410.

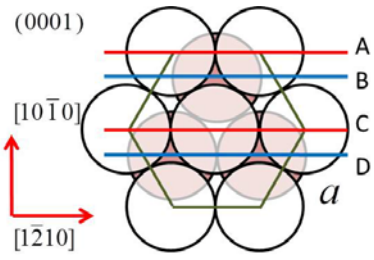
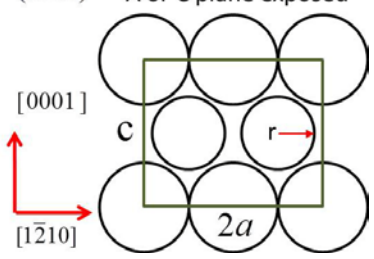
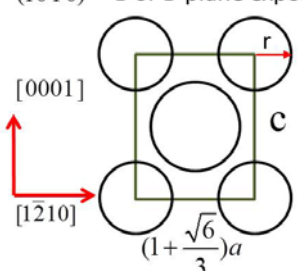
- (7) D. Zhang, Z. Liu, S. Han, C. Li, B. Lei, M. P. Stewart, J. M. Tour, C. Zhou, *Nano Lett.* 4(11) (2004) 2151-2155.
- (8) S.-F. Chen, H. Wei, C.-P. Liu, C. Y. Hsu, J. C. A. Huang, *Nanotechnology* 21 (2010) 425602.
- (9) K. Nielsch, F. Müller, A.-P. Li, U. Gösele, *Adv. Mater.* 8 (2000) 582-586.
- (10) H. Zeng, M. Zheng, R. Skomski, D. J. Sellmyer, Y. Liu, L. Menon, S. Bandyopadhyay, *J. Appl. Phys.* 87 (2000).
- (11) T. M. Whitney, J.S.Jiang, P.C.Searson, C.L.Chien, *Science* 261 (1993) 1316-1319.
- (12) S. I. Kim, J. H. Lee, Y. W. Chang, S. S. Hwang, K.-H. Yoo, *Appl. Phys. Lett.* 93 (2008) 033503.
- (13) L. Piraux, J. M. George, J. F. Despres, C. Leroy, E. Ferain, R. Legras, K. Ounadjela, A. Fert, *Appl. Phys. Lett.* 65 (1994) 2484-2486
- (14) K. Liu, K. Nagodawithana, P. C. Searson, C. L. Chien, *Physical Review B* 51 (1995) 7381-7384.
- (15) M. Darques, A. Encinas, L. Vila, L. Piraux, *J. Phys. D: Appl. Phys* 37 (2004) 1411-1416.
- (16) B. D. Cullity, C. D. Graham, *Introduction to Magnetic Materials*, JohnWiley & Sons, Inc., Hoboken, New Jersey, 2008.
- (17) Z. Jun, J. YaXin, W. HanBin, Y. Cong, T. WeiMing, W. Hao, *SCIENCE CHINA Physics, Mechanics & Astronomy* 54 (2011) 1244-1248.
- (18) S. Dubois, J. Colin, J. L. Duvail, L. Piraux, *Physical Review B* 61 (2000) 14315-14318.
- (19) H. Pan, H. Sun, C. Poh, Y. Feng, J. Lin, *Nanotechnology* 16 (2005) 1559-1564.
- (20) Y. Zhu, X. Dou, X. Huang, L. Li, G. Li, *Journal of Physical and Chemistry B* 110 (2006) 26189-26193.
- (21) M. Paunovic, M. Schlesinger, *Fundamentals of Electrochemical Deposition*, Wiley, New York, 1998.
- (22) H. Sun, X. Li, Y. Chen, W. Li, F. Li, B. Liu, X. Zhang, *Nanotechnology* 19 (2008) 225601.

- (23) H. Masuda, K. Fukuda, *Science* 268 (1995) 1466-1468.
- (24) W. Plieth, *Electrochemistry for Materials Science*, Elsevier, Oxford, 2008.
- (25) J.-M. Zhang, D.-D. Wang, K.-W. Xu, *Appl. Surf. Sci.* 253 (2006) 2018-2024.
- (26) X. W. Wang, G. T. Fei, P. Tong, X. J. Xu, L. D. Zhang, *J. Cryst. Growth* 300 (2007) 421-425.
- (27) M. Darques, L. Piraux, A. Encinas, P. Bayle-Guillemaud, A. Popa, U. Ebels, *Appl. Phys. Lett.* 86 (2005) 072508.
- (28) G. Riveros, S. Green, A. Cortes, H. Gomez, R. E. Marotti, E. A. Dalchiele, *Nanotechnology* 17 (2006) 561-570.
- (29) T. Gao, G. W. Meng, J. Zhang, Y. W. Wang, C. H. Liang, J. C. Fan, L. D. Zhang, *Applied Physics A Materials Science & Processing* 73 (2001) 251-254.
- (30) T. Gao, G. Meng, Y. Wang, S. Sun, L. Zhang, *J. Phys.: Condens. Matter* 14 (2002) 355-363.
- (31) S. Thongmee, H. L. Pang, J. Ding, J. Y. Lin, *J. Magn. Magn. Mater.* 321 (2009) 2712-2716.
- (32) H. Sun, Y. Yu, X. Li, W. Li, F. Li, B. Liu, X. Zhang, *J. Cryst. Growth* 307 (2007) 472-476.
- (33) Y.-N. Wen, J.-M. Zhang, *Solid State Commun.* 144 (2007) 163-167.

Supporting information

- For Co (hcp) structure, the crystal planar atomic packing density of three low index planes, including (0001), and $(1\bar{2}10)$, are calculated in Table S1. In the calculation, a and c are the lattice parameters ($c = \sqrt{\frac{8}{3}} a$) and R is the atomic radius ($a=2R$). The structures shown on the left hand column are the cross-sections of geometrical planes, thus half-cut atoms appear as smaller circles, as for the case of $(10\bar{1}0)$. The illustration of (0001) plane also shows the positions of four $(10\bar{1}0)$ planes, identifying the difference between A, C planes and B, D planes.

Table. S1 Crystal planar atomic packing density of three low index planes in hcp structure

Crystal plane structure	Plana atomic packing density
<p>(0001)</p> 	$\frac{(6 \times \frac{1}{3} + 1)\pi R^2}{\frac{1}{2} \times \frac{\sqrt{3}}{2} \times 6 \times a \times a} = 0.903$
<p>$(10\bar{1}0)$ A or C plane exposed</p> 	$\frac{(4 \times \frac{1}{4} + 2 \times \frac{2}{3} + 2 \times \frac{1}{2})\pi R^2}{c \times 2a} = 0.802$ $r = \frac{\sqrt{6}}{3} R$
<p>$(10\bar{1}0)$ B or D plane exposed</p> 	$\frac{(4 \times \frac{1}{4} \times \frac{2}{3} + 1)\pi R^2}{c \times (1 + \frac{\sqrt{6}}{3})a} = 0.441$ $r = \frac{\sqrt{6}}{3} R$

	$\frac{(4 \times \frac{1}{4} + 1)\pi R^2}{c \times \sqrt{3}a} = 0.555$
--	--

2. For fcc structure, the crystal planar atomic packing density of three low index planes, including (100), (110) and (111), are calculated in Table S2. In the calculation, a is the lattice parameter and R is the atomic radius ($a = 2\sqrt{2}R$).

Table. S2 Crystal planar atomic packing density of three low index planes in fcc structure

Crystal plane structure	Plana atomic packing density
	$\frac{(1 + 4 \times \frac{1}{4})\pi R^2}{a \times a} = 0.785$
	$\frac{(4 \times \frac{1}{4} + 2 \times \frac{1}{2})\pi R^2}{a \times \sqrt{2}a} = 0.555$
	$\frac{(3 \times \frac{1}{6} + 3 \times \frac{1}{2})\pi R^2}{\frac{1}{2} \times \frac{\sqrt{3}}{2} \sqrt{2}a \times \sqrt{2}a} = 0.903$

CHAPTER 7. Closing Remarks

This work studies the formation mechanisms of anodized materials and their related electrochemical anodic behaviors. The thesis presents the study in the form of 5 papers. The specific conclusions of these topics have been presented in each paper. Overall, the thesis may be summarized in three aspects of original contribution to the field, as following:

- (1) The thesis developed a unified theory based on thermodynamic and electrochemical principles to successfully explain the mechanisms, the criteria and the requirement of processing conditions for the formation of three different anodized structures of metals, including compact surface oxides, porous oxides and porous metals.
- (2) The completed experimental work presented in the thesis established quantification of the related electrochemical behaviors of some metals during anodization. This includes the voltage dependence of the products and their morphologies of anodization of Sn, the time evolution of the product morphology of SnC_2O_4 when anodizing Sn in oxalic acid, the voltage dependence of the orientation selection of Co nanowires, and the phenomenon of spontaneous periodical current oscillation during electrochemical anodization of tin in alkaline electrolytes. These information help future research in developing novel functional materials using electrochemical techniques.
- (3) In this work a variety of nanostructures are created by means of electrochemical

synthesis, including Co nanowire arrays, Co-Ni alloy nanowire arrays, porous SnO₂, and dendrite Sn materials. These materials have potentials to serve as novel functional materials in innovative applications, such as magnetic actuators in nano and micro scales, gas sensors and oxidation catalysts.

This study has also conducted investigations on three other topics which have not been published or included in the thesis. These works will be published later. These works include:

- (1) Anodization of Al in H₂SO₄, H₂C₂O₄ and H₃PO₄ electrolytes to form porous alumina of different channel diameters. The success of the fabrication of nano-channels of 200 nm in diameter in porous Al₂O₃ allows creation of metallic nano-pillars.
- (2) Crystallographic selective anodic etching of Sn in NaF electrolytes, which creates crystallographically defined etching wells into the surface of Sn.
- (3) Cathodic deposition of Co-Ni alloy system. The study not only enables electrochemical synthesis of Co-Ni alloys of desired compositions for different magnetic and martensitic transformation characteristics but also provides a model immiscible alloying system to investigate the alloy formation behavior of elements in solid state.

I hope these contributions would be of interests and value to the many fellow scientists, technologists and future research students in their effort to further advance the knowledge, develop the technology and search for new and better functional materials in the field of electrochemical materials science, beyond phenomenological studies.

The electrochemical anodization technique is proven to be a versatile and

cost-effective method in nanomaterials synthesis. The fundamental investigation provides vital knowledge to control the structure and morphology, thus property of these anodized nanomaterials. These nanomaterials are expected to utilize in the fields like energy storage and conservation, which will make exciting technological advancements for the benefit of our society.

With this note, I wish to thank you for reading my thesis and sharing with me the passion in the quest for knowledge for the betterment of the mankind.